Prospects for Charged Higgs Boson Searches at the Large Hadron Collider with Early ATLAS Data

A thesis submitted to the University of Manchester for the degree of

Doctor of Philosophy

in the Faculty of Engineering and Physical Sciences

2010

Jenna Louise Lane

School of Physics and Astronomy

Contents

Total word count: 29553

List of Tables

List of Figures

Abstract

In some theories beyond the Standard Model, such as Supersymmetry, the two complex scalar doublets required for electro-weak symmetry breaking result in, amongst other new particles, two charged Higgs bosons, $H^{\pm}$. This thesis presents the expected sensitivity to the $H^{\pm}$, assuming proton-proton collisions at a centre of mass energy $\sqrt{s} = 10$ TeV provided by the Large Hadron Collider and recorded by the ATLAS experiment. At this centre of mass energy, top-quark pairs are produced with a predicted cross section of 401.6 pb, and the $H^{\pm}$ are potentially produced in the top quark decay $t \rightarrow bH^{+}$, which replaces the Standard Model decay $t \rightarrow bW^{+}$. The $H^{\pm}$ were assumed to decay to the quark pairs $c\overline{s}$ or $s\overline{c}$, and the presence of the $H^{\pm}$ was inferred from a secondary peak in the W-boson mass distribution. A kinematic fitting method was used to gain better separation between the W-boson and $H^{\pm}$ mass peaks, and a maximum likelihood method was used to set the expected upper limits on the branching ratio $B(t \rightarrow bH^{+})$.

Assuming 200 pb^{-1} of data collected at $\sqrt{s} = 10$ TeV, the expected limits range between 4.3% and 17.8%, depending on the $H^{\pm}$ mass. This shows that ATLAS should be able to use early data to compete with the Tevatron experiments. Since ATLAS is now taking data at $\sqrt{s} = 7$ TeV, the expected limits assuming 1 fb^{-1} of data with $\sqrt{s} = 7$ TeV are also presented. These limits range between 3.5% and 15% depending on the $H^{\pm}$ mass.

Declaration

No portion of the work referred to in this thesis has been submitted in support of an application for another degree or qualification of this or any other university or other institution of learning.

Jenna Louise Lane
School of Physics and Astronomy
University of Manchester
Oxford Road
Manchester
M13 9PL
September 2010

Copyright

and/or Reproductions described in it may take place is available in the University IP Policy (see http://documents.manchester.ac.uk/DocuInfo.aspx?DocID=487), in any relevant thesis restriction declarations deposited in the University Library, the University Library's regulations (see http://www.manchester.ac.uk/library/-aboutus/regulations) and in the University's policy on presentation of theses.

The Author

The author was educated at William Farr C.E. Comprehensive school between 1995 and 2002. In 2002 she moved to Manchester to study physics, and graduated in 2006 with a first class honours degree. She then continued her studies at Manchester University, joining the High Energy Physics group to work with Unki Yang and Fred Loebinger.

Acknowledgements

Firstly I would like to thank my parents, for making it possible for me to go to university in the first place. Without their encouragement and financial support I would never have made it to this point. Also thanks to Dave and Dee, for respectively looking after my Mum and Dad, and to Libby for being the most supportive and brilliant sister in the world.

Thanks to Un-ki Yang and Fred Loebinger for their excellent supervision. I would particularly like to thank Fred, for his pep-talks and his unwavering belief in me, even when I wasn't so sure myself! I am also very grateful to all of the people that I have worked with throughout my PhD - without you this thesis probably wouldn't exist. For my charged Higgs analysis, thanks to Arnaud Ferrari, Chris Potter and Miika Klemetti, for being such a great group of people to work with. Paul Miyagawa deserves a special mention for his work on the charged Higgs analysis at 7 TeV. For my work on the Event Filter, thanks to Stefan Ask and Jiri Masik, and extra special thanks for being such lovely office mates whilst I was based at CERN.

Thanks to all of the people I've shared an office with over the last few years; not only has it been fun, but your help with programming, and our discussions of my work have been invaluable to me. People who deserve a special mention are Simon Head, Paul Bell, Alex Martyniuk, Andy Pilkington, Chris Tevlin and Mark

Owen. Also, thanks to all of my friends for being so fantastic. You know who you are, but I would especially like to thank Jen Sutton, Lisa Alexander-Nunneley, Jack Hill and Chris Headington, for being such supportive friends.

Finally, I would like to thank Rob for his love, encouragement and support (and all of the cups of tea).

Dedication

This thesis is dedicated to William Lane.

Chapter 1

Introduction

The Standard Model of particle physics [1] has had remarkable success in describing the observed particles that make up our universe and the strong, electromagnetic and weak processes via which they interact. The theory, however, does not explain the different mass scales of these particles and the origin of mass is arguably the biggest unanswered question in modern-day particle physics. The minimal Higgs mechanism [2] offers a potential way to generate particle masses and predicts the existence of one new particle known as the Standard Model Higgs boson. To date it has not been observed in experiment, but the search for the Higgs boson is one of the main remits of particle collider facilities, such as the Large Hadron Collider (LHC) [3] at CERN and the Tevatron [4] at Fermilab.

The minimal Higgs mechanism is the simplest model to explain mass generation in the Standard Model, but is widely believed to be flawed. Assuming that, other than gravity, there are no additional physics processes to add to the Standard Model, theoretical calculations predict a Higgs boson with a mass of the order of 10^{16} GeV [5]. However, precision measurements of the top quark and W-boson masses can be used to infer the mass of the Higgs boson and indicate

that it is of the order of 100 GeV [6]. This striking disagreement is suggestive of additional physics processes beyond the Standard Model.

The Minimal Supersymmetric Extension to the Standard Model (MSSM) [7] describes mass generation, whilst allowing theoretical predictions of the Higgs mass to be consistent with precision electro-weak measurements. The MSSM is, necessarily, more complex than the Standard Model and introduces a symmetry between bosons and fermions. The model predicts that each fermion in the Standard Model will have a boson super-partner and vice-versa, thereby introducing a wealth of additional particles. The mechanism of mass generation in the MSSM also predicts the existence of three neutral Higgs bosons: h, H and A, along with two charged Higgs bosons, $H^{\pm}$. An experimental observation of the charged Higgs bosons would, therefore, rule out the minimal Higgs mechanism as the mechanism of mass generation.

The charged Higgs mass, m_{H^+}, is not predicted by the MSSM, although it is closely connected to the W-boson mass according to $m^2_{H^+} = m^2_A + m^2_W$. Experimentally, analyses from the Large Electron-Positron (LEP) collider [8] have set a limit of $m_{H^+} > 78.6$ GeV using a direct mass scan [9]. At hadron-hadron colliders, such as the LHC or the Tevatron, where a mass scan is not possible, the direct production of charged Higgs bosons is difficult to separate from high cross-section processes such as QCD di-jet production. The MSSM predicts that a 'light' charged Higgs can be produced in association with a bottom quark, via the decay of a top quark in $t \rightarrow bH^+$ or the charge conjugate decay. The charged Higgs boson thus replaces the W-boson in the Standard Model decay $t \rightarrow bW^+$. A light charged Higgs fulfills the requirement $m_{H^+} < m_t - m_b$, where m_t and m_b are, respectively, the top and bottom quark masses. The D0 [10] and CDF [11] experiments at the Tevatron have measured the top quark mass, m_t, to be 173.3 $\pm$ 1.1 GeV [12].

Using proton-proton collisions with a centre of mass energy $\sqrt{s} = 1.96$ TeV provided by the Tevatron accelerator, the CDF and D0 experiments have set limits on the branching ratio $B(t \rightarrow bH^+)$ for various potential decay modes of the charged Higgs boson [13] [14]. The scenario considered in this thesis is a leptophobic charged Higgs, which decays exclusively to a doublet of charm and strange quarks (($c\overline{s}$) or the charge conjugate pair). Under this assumption, Figure 1.1 shows the limits published by the CDF experiment using 2.2 fb^{-1} of data. The CDF analysis is based on the shape of the mass distribution of the $c\overline{s}$ quark pair which, in the case of the Standard Model decay $t \rightarrow bW^+$ produces the W-boson mass distribution. The limits on $B(t \rightarrow bH^+)$ are inferred by searching for an additional peak in the W mass distribution, which could be attributed to a potential charged Higgs signal. As m_{H^+} approaches the W-boson mass, m_W, however, the signal cannot be separated from the Standard Model $t\overline{t}$ decay, and limits are not quoted in this region. The black solid line in Figure 1.1 shows the expected upper limit on $B(t \rightarrow bH^+)$ at 95% confidence level, based on Monte Carlo studies, while the solid bands show the regions in which 68% and 95% of experimental results would be expected to fall. The red circles show the upper limit at 95% confidence level, based on the analysis of real data.

The limits on $B(t \rightarrow bH^+)$ have also been evaluated by the D0 experiment, based on an analysis of 1 fb^{-1} of data and the assumption of a leptophobic charged Higgs. The results are shown in Figure 1.2 and show relatively little variation over the full range of m_{H^+}. The D0 analysis is a counting experiment and does not depend on the shape of the $c\overline{s}$ mass distribution. The best limits on $B(t \rightarrow bH^+)$ range between 8% and 22% depending on m_{H^+} and, with the exception of the mass range 80 - 90 GeV, come from the CDF analysis. Due to the small cross section to produce top quarks at the Tevatron, however, these measurements are still limited by low statistics.

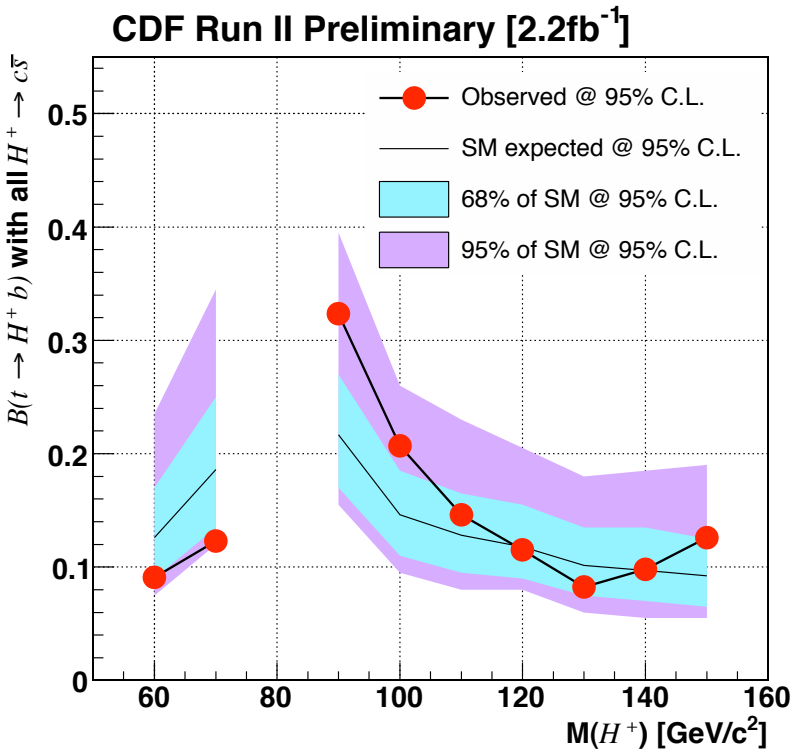

Figure 1.1: Upper limits on $B(t \to H^+ b)$ assuming 2.2 fb^{-1} of CDF data recorded at $\sqrt{s} = 1.96$ TeV [13].

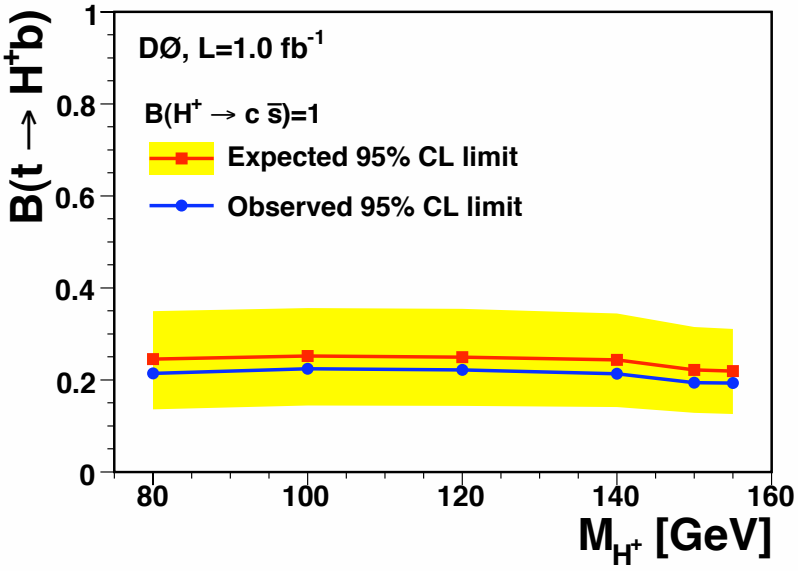

Figure 1.2: Upper limits on $B(t \to H^+ b)$ assuming 1 fb^{-1} of D0 data recorded at $\sqrt{s} = 1.96$ TeV [14].

In April 2009, the Large Hadron Collider [3] began to provide proton-proton collisions at centre of mass energy $\sqrt{s} = 7$ TeV. After the failure of a magnet interconnect in September 2008 the machine was initially expected to run with $\sqrt{s} = 10$ TeV, and many Monte Carlo studies were performed under this assumption. However, in August 2009, the decision was made to have an extended run with $\sqrt{s} = 7$ TeV before attempting to reach higher energies. The ATLAS detector [15] is one of the four main experiments at the LHC, and is designed to search for new physics signals, in addition to making precision measurements of the properties of known particles. The main purpose of this thesis is to develop the search tools for a charged Higgs analysis in the $H^+ \to c\overline{s}$ channel, and to study the expected sensitivity to the branching ratio $B(t \to bH^+)$, with the first 200 pb^{-1} of data recorded by ATLAS at $\sqrt{s} = 10$ TeV. Given the current LHC schedule, however, equivalent results are also presented assuming 1 fb^{-1} of data at $\sqrt{s} = 7$ TeV.

This thesis is structured as follows. Chapter 2 gives an overview of the theoretical motivation for a charged Higgs search with early ATLAS data. Chapter 3 describes the LHC machine and the ATLAS detector. In Chapter 4, results are presented from tracking studies using ATLAS data from cosmic rays, and from proton-proton collisions at $\sqrt{s} = 900$ GeV and 7 TeV. This work is an essential component of the electron and muon triggers used for the charged Higgs analysis, and formed an important contribution to the commissioning of the ATLAS detector. Chapter 5 gives an overview of the Monte Carlo simulated data used for the charged Higgs analysis, while Chapter 6 describes the methods used to select the events of interest to study. The main analysis method is described in Chapter 7, whilst Chapter 8 deals with the systematic uncertainties that affect the expected limit on $B(t \to bH^+)$. Conclusions are made in Chapter 9, along with a discussion of future extensions to the analysis.

Chapter 2

Theoretical Motivation

2.1 The Standard Model

The Standard Model of Particle Physics [1, 16] is an effective theory that seeks to describe the fundamental particles that have been observed in nature, and their interactions with one another. The experimentally observed particles fall into two categories: a group of spin-half fermions which constitute matter, and a group of integer-spin bosons, via which the fermions interact. The group of fermions is known to consist of six quarks and six leptons, organised into three generations, and is shown in Table 2.1. Each fermion is also observed to have an antiparticle with the same mass and spin, but opposite electric charge. The 'handedness' of a particle is defined by the projection of the particle spin along its momentum axis. Only left-handed neutrinos have been observed in experiments, and this must also be accounted for in the theory.

Four types of particle interaction have been observed in nature. The Standard Model is able to describe three of these interactions which are listed, along with

	Electric Charge	1^{st} Generation	2^{nd} Generation	3^{rd} Generation
Quarks	+2/3 -1/3	Up (u) Down (d)	Charm (c) Strange (s)	Top (t) Bottom (b)
Leptons	1 0	Electron (e) e neutrino (ν_e)	Muon (μ) μ neutrino (ν_μ)	Tau (τ) τ neutrino (ν_τ)

Table 2.1: The matter content of the Standard Model, which can be ordered in three generations of particles. The features of each generation are very similar, with the exception of the particle masses which are smallest for the first generation and largest for the third generation. For example, the lepton masses range from 0.511 MeV for the electron to 1.777 GeV for the tau.

Interaction	Associated bosons	Boson mass (GeV)
Strong	Gluon	0
Electromagnetic	Photon	0
Weak	$W^{\pm}$, Z^0	80.4, 91.2

Table 2.2: The interactions described by the Standard Model, and their associated bosons.

their associated force carrying boson, in Table 2.2. The strong force is responsible for interactions between quarks and gluons. The electromagnetic and weak forces are found to be linked, and are unified in the electro-weak interaction, which accounts for all other observed collider phenomena. Gravity is not described by the Standard Model, although it is postulated that gravitational interactions occur by a similar mechanism, where the force carrying boson is known as a graviton. The gravitational force is weak in strength, compared to the three forces described by the Standard Model.

2.2 Interactions in the Standard Model

Interactions in the Standard Model are based on the requirement that a Lagrangian must be invariant under a local phase transformation of the particle

fields. A simple example of this idea is U(1) local phase invariance. A massless fermion, ψ, can be described by the Lagrangian:

$$\mathcal{L} = i\overline{\psi}\gamma^{\mu}\partial_{\mu}\psi \tag{2.1}$$

where ψ is a four-component Dirac spinor, and the γ^{μ} are the Dirac gamma matrices [16]. We study the properties of $\mathcal{L}$ under the transformation:

$$\psi(x) \rightarrow e^{i\alpha(x)}\psi(x) \tag{2.2}$$

where $\alpha(x)$ is an arbitrary function of space-time and this U(1) set of transformations forms an Abelian group. The phase invariance of Equation 2.1 is destroyed by the presence of the derivative ∂_{μ}. Enforcing invariance of $\mathcal{L}$ dictates that we replace ∂_{μ} with a 'covariant derivative', D_{μ}, which has the same transformation properties as ψ. This is achieved by constructing:

$$D_{\mu} \equiv \partial\mu - ieA_{\mu} \tag{2.3}$$

where we must also introduce a vector field, A_{μ}, which transforms as:

$$A_{\mu} \rightarrow A_{\mu} + \frac{1}{e}\partial_{\mu}\alpha. \tag{2.4}$$

Replacing ∂_{μ} with the covariant derivative of Equation 2.3 in the original Lagrangian, Equation 2.1, then gives:

$$\mathcal{L} = i\overline{\psi}\gamma^{\mu}\partial_{\mu}\psi + e\overline{\psi}\gamma^{\mu}\psi A_{\mu} - \frac{1}{4}F_{\mu\nu}F^{\mu\nu}. \tag{2.5}$$

The requirement of local phase invariance of $\mathcal{L}$ introduces a gauge field A_{μ}, which couples to the fermion field with coupling strength e. The first additional term, $e\overline{\psi}\gamma^{\mu}\psi A_{\mu}$, in the Lagrangian describes an interaction between the fermion field and the gauge field, and is identical to the electron-photon interaction in QED. The final term, $-\frac{1}{4}F_{\mu\nu}F^{\mu\nu}$, has been added by hand, and is a gauge invariant kinetic term for A_{μ}, where:

$$F_{\mu\nu} = \partial_{\mu}A_{\nu} - \partial_{\nu}A_{\mu}. \tag{2.6}$$

The kinetic term is required to describe the propagation of the gauge field. This completes the description of the particle, with the exception of its mass. It is not possible to add to the Lagrangian an explicit mass term of the form $\frac{1}{2}m^2 A_\mu A^\mu$ for the gauge field, without violating gauge invariance.

2.3 The Gauge Groups of the Standard Model

Invariance of the Lagrangian under a U(1) local phase transformation is seen to describe the photon and reproduce the well-measured results of QED. The full Standard Model is described by invariance under the product of the groups $U(1)_Y$, $SU(2)_L$ and $SU(3)_C$, where the groups are associated with hypercharge (Y), weak (L) and colour (C) symmetries respectively. The subscript L denotes a transformation only affecting left-handed particles, and is responsible for the fact that right-handed neutrinos have not been observed in nature. The full gauge group is most easily pictured as a $SU(3)_C$ transformation describing the strong interaction, and a $U(1)_Y \otimes SU(2)_L$ transformation describing the electro-weak interaction. The interactions are derived following the method in Section 2.2, but the more complicated group structure leads to the expected four electro-weak gauge bosons, and the eight gluons associated with the strong interaction.

2.4 The Higgs Mechanism

The Standard Model is, as yet, a massless theory. The model accurately describes the observed particles and their interactions, but it does not describe the particle masses. We have already ascertained that we cannot add mass terms to the Lagrangian if we insist on gauge invariance. This problem can be solved using

the Higgs mechanism [17], which is elegantly demonstrated by the breaking of the U(1) gauge symmetry described in Section 2.2.

A complex scalar field, $\phi = (\phi_1 + i\phi_2)/\sqrt{2}$, can be described by the Lagrangian:

$$\mathcal{L} = (\partial_\mu \phi)^*(\partial^\mu \phi) - \mu^2 \phi^* \phi - \lambda(\phi^* \phi)^2 \tag{2.7}$$

where $\lambda > 0$. Using the substitutions 2.3 and 2.4 ensures that this Lagrangian is invariant under a U(1) transformation and introduces a vector field, A_μ, as described in section 2.1. In the case that $\mu^2 > 0$, the potential describes a complex scalar field with mass μ. However, in the case that $\mu^2 < 0$ the potential no longer has a single minimum at (0,0) in the ϕ_1,ϕ_2 plane. Instead, there is a circle of minima, with radius:

$$v^2 = -\frac{\mu^2}{\lambda}. \tag{2.8}$$

In order to do a perturbative expansion of ϕ we must pick a minimum to expand about. Since all solutions are equivalent, we can pick ϕ_1=v and ϕ_2=0 with no loss of generality. On substituting the expansion:

$$\phi(x) = \sqrt{\frac{1}{2}}[v + \eta(x) + i\xi(x)] \tag{2.9}$$

into the U(1) gauge invariant Lagrangian:

$$\mathcal{L}' = \frac{1}{2}(\partial_\mu \xi)^2 + \frac{1}{2}(\partial_\mu \eta)^2 - v^2 \lambda \eta^2 + \frac{1}{2} e^2 v^2 A_\mu A^\mu - e v A_\mu \partial^\mu \xi + X \tag{2.10}$$

where X denotes additional interaction terms [16], we find that the substitution has revealed a mass term for the vector field, A^μ, in addition to terms describing a massless scalar field, ξ, and a massive scalar field, η. The act of choosing one potential solution is known as spontaneous symmetry breaking of the system. However, not all of the resulting fields correspond to physical particles. By giving mass to A^μ, we increase the polarisation degrees of freedom of the particle from two to three. A simple translation of Lagrangian co-ordinates cannot generate

this extra degree of freedom. The field ξ, known as a Goldstone boson, does not correspond to an observable particle, but the additional degree of freedom required to give mass to the A^{μ}. A striking prediction of the theory, however, is the massive field η - a real particle known as the Higgs boson that, if this model were correct, could be observed by experiment. This is a simplified model limited to a U(1) gauge invariant Lagrangian, but it shows how a translation of co-ordinates can reveal boson mass terms that were ostensibly forbidden by gauge invariance.

Experimental observations in the electro-weak sector require our model to describe a massless photon and the three massive gauge bosons, $W^{\pm}$ and Z^0. In the simplest model, this requires four real scalar fields, ϕ_i which are arranged in an isospin doublet with hypercharge Y = 1. The procedure is very similar to the U(1) model above, except that now the Lagrangian must be $SU(2)_L \otimes U(1)_Y$ gauge invariant. Three of the ϕ_i provide the longitudinal polarisations required to give mass to the $W^{\pm}$ and Z^0, while the remaining degree of freedom becomes a massive scalar field, known as the Higgs boson. The mass of the Higgs boson is not predicted by the theory, although the vacuum expectation value, v, is related to known quantities such as the gauge boson masses and is predicted to be 246 GeV. Note that mass terms through the breaking of $SU(3)_C$ symmetry are not required as the gluons are known experimentally to have zero mass.

2.5 Why go Beyond the Standard Model?

The Standard Model is an extremely successful theory whose predictions have been rigorously tested by different experiments over many decades. It is widely acknowledged, however, that, together with mass generation by the minimal Higgs

mechanism, the Standard Model leaves several unanswered questions that have implications in both particle physics and astrophysics. The theory is already known to be incomplete, since it does not include gravitational interactions. It is sensible, therefore, to also consider the possibility of new physics processes that occur only at energy scales beyond the reach of previous accelerator experiments. The following arguments highlight areas where the Standard Model is open to criticism, and suggest that the current form of the theory, even with the addition of quantum gravity, would not be complete.

The most compelling argument for new physics is the hierarchy problem, which is related to the vast difference between the relative strengths of the gravitational and weak interactions. This is equivalent to asking why the W-boson mass is so much smaller than the Planck mass, $M_P = 10^{18}$ GeV, and it has an important effect on the Higgs mass in a model that does not predict any new physics other than gravitational interactions. The Higgs mass is affected by quantum loop corrections, such as the lowest order loop diagram shown in Figure 2.1. The momentum in the loop is unknown; the size of the correction is evaluated by integrating over all possible momenta up to a cut-off, Λ, where new physics processes are expected to contribute additional diagrams. Since this integral is quadratically divergent, the correction to the Higgs mass becomes large in the absence of any new physics process, and the Higgs mass is driven to the highest scale in the problem. Assuming no new physics until the Planck scale, $\Lambda = M_P$, the correction to the Higgs mass squared is then $\delta m^2 = O(10^{36})$ GeV^2.

Experimental results interpreted in the context of the minimal Higgs mechanism favour a 'light' Higgs boson. The combined limit on the Higgs mass, m_h, from the LEP experiments is $m_h > 114$ GeV, whilst precision electroweak measurements from both the LEP and Tevatron experiments imply $m_h < 186$ GeV [18].

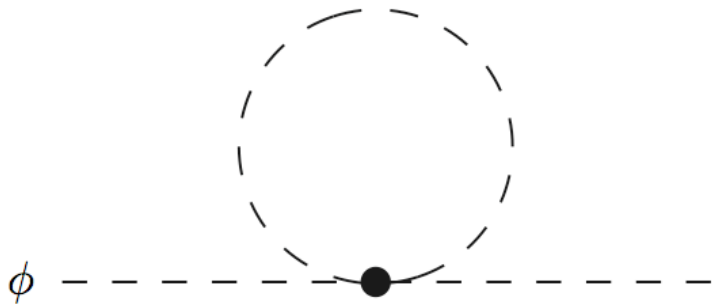

Figure 2.1: The Higgs propagator can be modified by loop corrections, which correspond to the emission and re-absorption of a particle. The momentum flow around the loop is not known. Shown is an example of a one-loop correction to the Higgs mass according to the Standard Model.

Unless new physics processes occur at a relatively low scale, tuning of parameters over many orders of magnitude is required in order to reconcile experimental observations with theoretical predictions. Although this is still potentially the solution, it is widely regarded as an unnatural explanation, especially when juxtaposed with the Standard Model whose predictions arise from internal symmetries with no tuning requirements.

The structure of the Standard Model is the result of the invariance of a Lagrangian under three different groups of transformations: $U(1)_Y$, $SU(2)_L$ and $SU(3)_C$. This results in the electromagnetic, weak and strong interatcions, each of which has its own coupling to describe the strength of the interaction. The couplings vary with the scale of the interaction, and their evolutions to high energies are shown in Figure 2.2, assuming that there is no new physics until the Planck scale. The couplings show a convergent behaviour, although they do not meet exactly. Historically, the Standard Model has explained complex phenomena through the principle of underlying symmetries, and Grand Unified

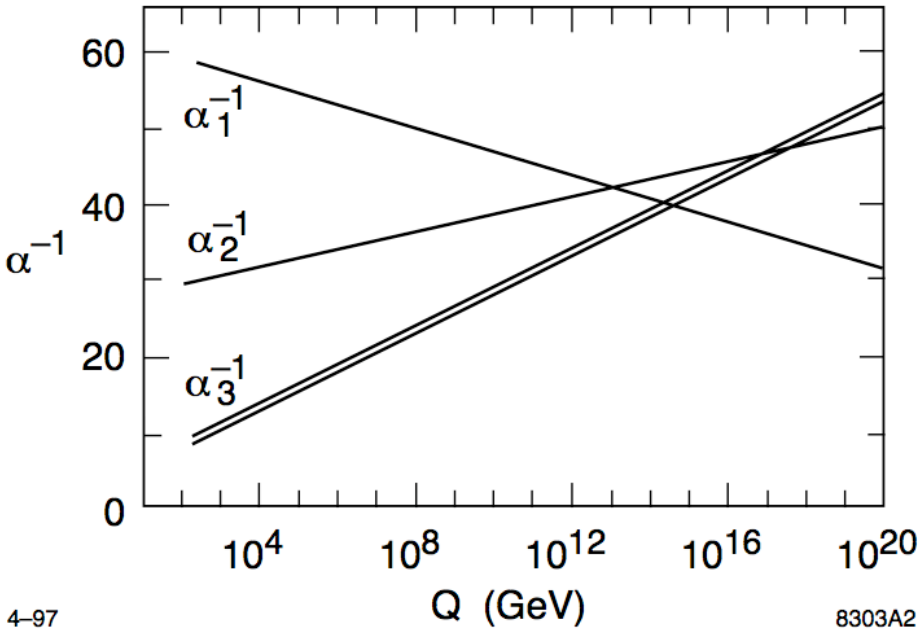

Figure 2.2: The running couplings as a function of the interaction scale, Q, according to the Standard Model [7]. The couplings α_1, α_2 and α_3 correspond to $U(1)_Y$, $SU(2)_L$ and $SU(3)_C$ respectively. The double line represents the size of the experimental uncertainty on the measurement of α_3.

Theories [7] suggest that at a very high scale the three interactions can be unified in a single interaction described by one gauge group and one coupling constant. This requires that at the relevant scale the coupling constants fully converge, which is suggestive of new physics before the Planck scale.

Astronomers have used observations of galactic rotation to infer the amount of matter present in particular galaxies. The results show discrepancies with studies of electromagnetic radiation from the same galaxies, and this has led to the conclusion that much of the universe is composed of non-baryonic 'cold dark matter'. The Standard Model, however, does not predict any particle that fulfills these requirements.

2.6 Supersymmetry

Supersymmetry is a possible extension to the Standard Model, where the Lagrangian is required to be invariant under the transformation:

$$Q|\text{Boson}> = |\text{Fermion}> \quad \text{and} \quad Q|\text{Fermion}> = |\text{Boson}> . \tag{2.11}$$

The supersymmetry operator, Q, transforms a fermion into a boson, or a boson into a fermion. In order to satisfy this requirement each fermion must have a boson super-partner and vice-versa, with generally the same quantum numbers, but whose spin differs by half a unit. Supersymmetry therefore introduces a wealth of new particles to the Standard Model, a detailed description of which can be found in [5]. The Minimal Supersymmetric Standard Model (MSSM) is the version of supersymmetry that requires the fewest additional particles.

To date there have been no experimental observations of supersymmetric particles. If they exist, these new particles are likely to be more massive than their Standard Model counterparts and, therefore, result from a broken symmetry. The mechanism of supersymmetry breaking is, however, not known. In an unconstrained model, supersymmetry breaking leads to around 120 additional unknown parameters, such as particle masses and mixing angles [19]. This is clearly impractical in terms of making theoretical predictions or interpreting experimental results. The number of free parameters in the theory can be dramatically reduced by assuming a particular mechanism for supersymmetry breaking. One example is minimal supergravity (mSUGRA), where supersymmetry breaking is mediated by gravitational interactions.

Electroweak symmetry breaking in the MSSM follows the logic of the Higgs mechanism described in Section 2.4, but requires two complex doublets of scalar fields. The additional degrees of freedom result in five Higgs bosons, three of

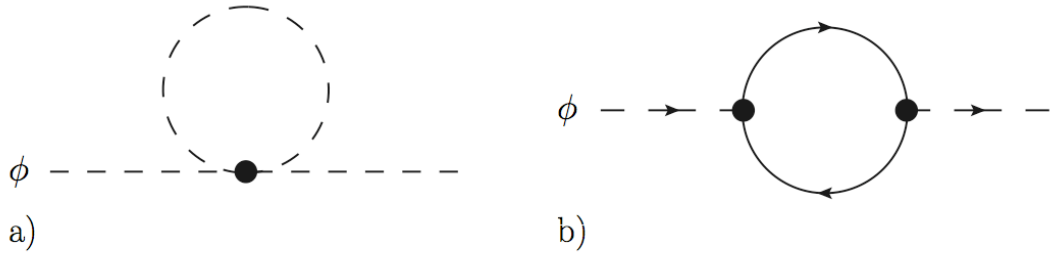

Figure 2.3: a) The correction to the Higgs mass due to a boson loop which, according to supersymmetry, will be cancelled by b) the equivalent fermion loop.

which are neutral (h, H, A) and two of which charged ($H^{\pm}$). An important parameter is $\tan\beta$, the ratio of the vacuum expectation values from the two scalar doublets. At leading order, the MSSM Higgs sector is fully determined by $\tan\beta$ and the charged Higgs mass, m_{H^+}, although dependence on additional MSSM parameters is introduced at higher orders.

Supersymmetry offers a solution to each of the problems described in Section 2.5. The loop correction to the Higgs propagator due to any Standard Model particle will be accompanied by the equivalent diagram involving its superpartner, as shown in Figure 2.3. Since one loop contains a boson and the other a fermion, the diagrams have opposite signs when evaluated and can cancel one another. The cancellation cannot be exact, since the pairs of particles do not have degenerate masses. If supersymmetry exists at the TeV scale, however, this effect can remove much of the fine tuning required to make the Higgs mass agree with the predictions from precision electro-weak measurements.

Assuming R-parity conservation, meaning that the number of supersymmetric and Standard Model particles is conserved in any given interaction, the lightest supersymmetric particle (LSP) is not able to decay. The LSP is thus a candidate

particle for non-baryonic cold dark matter.

Finally, with the inclusion of supersymmetry, the couplings α_1, α_2 and α_3 are predicted to unify at a mass scale of 10^{16} GeV. The argument that Grand Unification is not possible with the Standard Model alone is an aesthetic one, and does not prove that the Standard Model is incomplete. However, the convergent behaviour of the couplings is suggestive of some possible underlying symmetry, and is widely considered as a reason to investigate supersymmetry.

2.7 Top Quark Physics

The top quark is, to date, the heaviest known particle in the Standard Model and was discovered by the CDF and D0 experiments in 1995 [20], [21]. Top quarks are predominantly produced in $t\bar{t}$ pairs via the diagrams shown in Figure 2.4. At the LHC, around 90% of $t\bar{t}$ pairs are produced by gluon-gluon fusion, with the remaining 10% from $q\bar{q}$ annihilation. This is a result of the Parton Distribution Functions (PDFs) for quarks and gluons inside the proton. The PDFs describe the probability of a parton carrying a particular momentum fraction, x, of the total proton momentum. In order to produce a $t\bar{t}$ pair, the hard-scatter must have a minimum energy of $2m_t$. For $\sqrt{s} = 10$ TeV, this corresponds to $x = 0.035$, whilst at the Tevatron ($\sqrt{s} = 1.96$ TeV) $t\bar{t}$ production requires $x = 0.18$. The gluon and up quark distributions from the CTEQ6M PDF set [22] are shown as an example in Figure 2.5. The LHC probes the low-x region, where the gluon PDF is dominant, thus top-pair production is predominantly via diagrams involving gluon-gluon fusion. The Tevatron probes a higher-x region where the quark PDFs dominate, and the majority of $t\bar{t}$ events result from $q\bar{q}$ annihilation.

The cross section for $t\bar{t}$ production, $\sigma_{t\bar{t}}$, varies as a function of both the centre

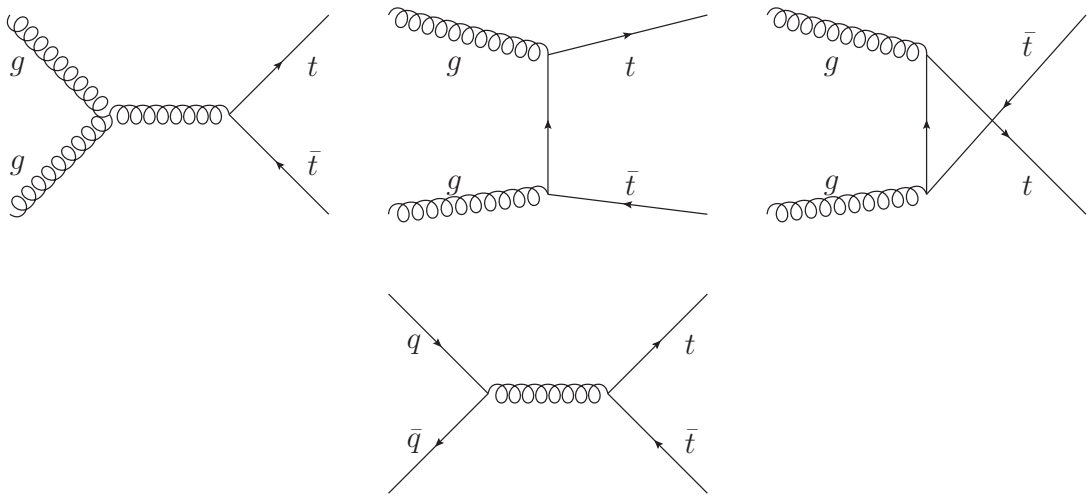

Figure 2.4: The leading order diagrams for top quark pair production, which can occur by gluon-gluon fusion or by $q\overline{q}$ annihilation. (Taken with permission from [23]).

of mass energy of the colliding protons and the top quark mass. For a top mass of 172.5 GeV and centre of mass energy $\sqrt{s} = 10$ TeV the predicted cross section is 401.6 pb based on an approximate next to next to leading order calculation [24]. This is considerably larger than the $t\bar{t}$ cross section at the Tevatron, which has been measured by the CDF experiment as 7.50 ± 0.48 pb [25], assuming a top mass of 172.5 GeV. Top-related measurements at the Tevatron are still limited by statistical uncertainties. The comparatively large cross section to produce top-pairs at the LHC will quickly provide copious numbers of top events to study.

In the Standard Model, the top quark has a lifetime of around 5 x 10^{-25} s. This is shorter than the characteristic timescale in which strong interaction processes occur, and the top quark decays weakly before bound hadronic states are able to form. It offers, therefore, the opportunity to study a 'bare' quark, whose properties are not disguised by parton showering and hadronisation effects. The top quark decay is flavour-changing and, in the Standard Model, proceeds at leading order via the charged electroweak bosons $W^{\pm}$.

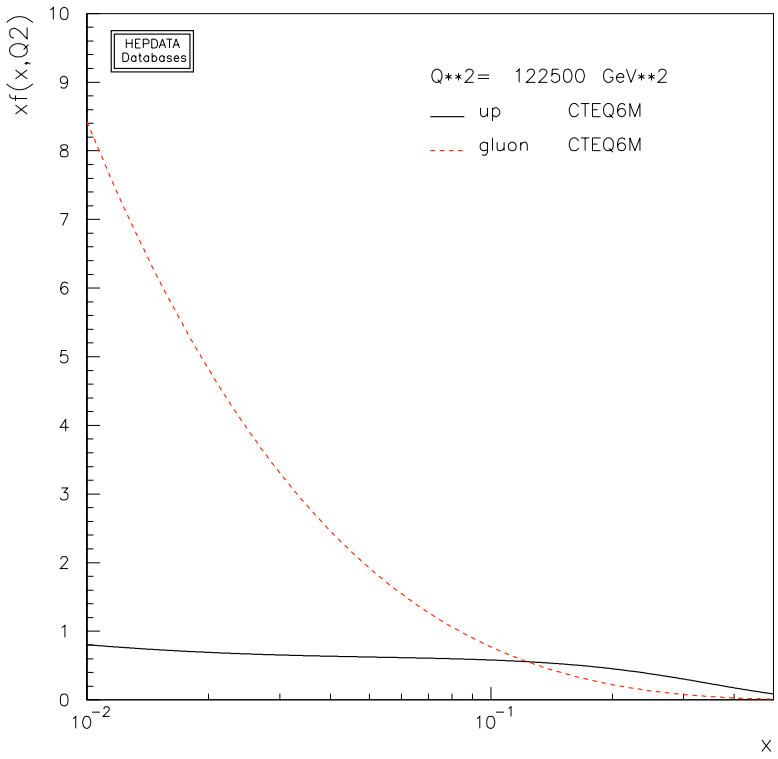

Figure 2.5: The parton distribution functions for a gluon and up quark, assuming a scale $Q^2 = 4m_t^2$, as given by the CTEQ6M PDF set. At the LHC, assuming $\sqrt{s}$ =10 TeV, top-quark pairs can be produced at momentum fraction $x = 0.035$, whereas at the Tevatron top-quark pair production requires a minimum of $x = 0.18$.

The charged current interaction couples left-handed up and down-type quark states:

$$\begin{pmatrix} u \\ \tilde{d} \end{pmatrix}_L , \begin{pmatrix} c \\ \tilde{s} \end{pmatrix}_L , \begin{pmatrix} t \\ \tilde{b} \end{pmatrix}_L \tag{2.12}$$

where the states $\tilde{d}$, $\tilde{s}$ and $\tilde{b}$ are orthogonal combinations of the physical quark states d, s and b. This can be understood as a 'mixing' of physical quark states, which allows decays between different quark generations. The amount of mixing is described by the Cabibbo-Kobayashi-Maskawa (CKM) matrix, V_{CKM}, whose elements $|V_{ij}|$ parameterise the amplitude for the weak decay of a physical quark state i to another physical quark state j via a flavour-changing weak interaction.

$$\begin{pmatrix} \tilde{d} \\ \tilde{s} \\ \tilde{b} \end{pmatrix}_L = \begin{pmatrix} V_{ud} & V_{us} & V_{ub} \\ V_{cd} & V_{cs} & V_{cb} \\ V_{td} & V_{ts} & V_{tb} \end{pmatrix} \begin{pmatrix} d \\ s \\ b \end{pmatrix}_L . \tag{2.13}$$

The elements of the CKM matrix have been measured experimentally, and the diagonal elements V_{ud}, V_{cs} and V_{tb} are dominant. [16] In particular, the element $|V_{tb}| \cong 1$ and the top quark decays almost exclusively as $t \rightarrow W + b$. As a result, the decay of a top-quark pair can be characterised by the decay of the two W-bosons in the event Note that here, and throughout this document, W is used to represent a generic $W^{\pm}$ boson unless otherwise stated. In around one third of cases, a W-boson will decay 'leptonically' to either $e\nu$, $\mu\nu$ or $\tau\nu$, in roughly equal proportions. In the remaining two thirds of cases, the W-boson will decay 'hadronically' to $q\overline{q}'$, where q and $\overline{q}'$ are the quark doublets $(u\overline{d})$, $(c\overline{s})$ or their charge conjugate pairs. The quarks are observed in the detector as jets of particles, which are discussed in more detail in Chapter 6.1.4.

There are three possible decay modes for a $t\overline{t}$ pair.

- In the dilepton channel, both W-bosons decay leptonically, and the full decay chain can be summarised as $t\overline{t} \rightarrow W^+W^-b\overline{b} \rightarrow l^+l^-\nu\overline{\nu}b\overline{b}$. Dilepton

top events can typically be triggered with a high efficiency, due to the clean signal of the two leptons. However, since the presence of a neutrino is inferred from missing transverse energy, E_T^{miss}, in a detector, the two neutrinos cannot be distinguished from one-another. This complicates the reconstruction of high-level objects in the event, such as the top quarks or W-bosons. The dilepton channel has the smallest branching ratio of the possible top decay modes.

- In the semi-leptonic channel, one W-boson decays leptonically while the other decays hadronically, leading to a decay of the form $t\bar{t} \rightarrow W^+W^-b\bar{b} \rightarrow l\nu q_1\overline{q_2}b\bar{b}$. The presence of the high p_T lepton means that this channel is still efficient to trigger. In addition, information about the single neutrino can be inferred from the measurement of the E_T^{miss}.

- In the all-hadronic channel, both W-bosons decay hadronically, and the decay can be summarised as $t\bar{t} \rightarrow W^+W^-b\bar{b} \rightarrow q_1\overline{q_2}q_3\overline{q_4}b\bar{b}$. It is difficult to trigger signal events in this channel with a high purity, since there is no lepton in the event. Instead, the trigger strategy must be based on the jet multiplicity and, as a result, it is challenging to separate the top-pair events from the QCD multi-jet background.

This analysis considers $t\bar{t}$ events in the semi-leptonic channel, which is characterised by a high p_T lepton, a large E_T^{miss} due to the non-interacting neutrino, and four jets. The semi-leptonic channel can be further separated into a 'tau + jets' channel, where the W-boson decays to a tau, and the 'lepton + jets' channel, where the W-boson decays to an electron or a muon. This distinction is relevant in the definition of the signal events in Chapter 5. The potential decay modes of a $t\bar{t}$ pair are shown pictorially in Figure 2.6.

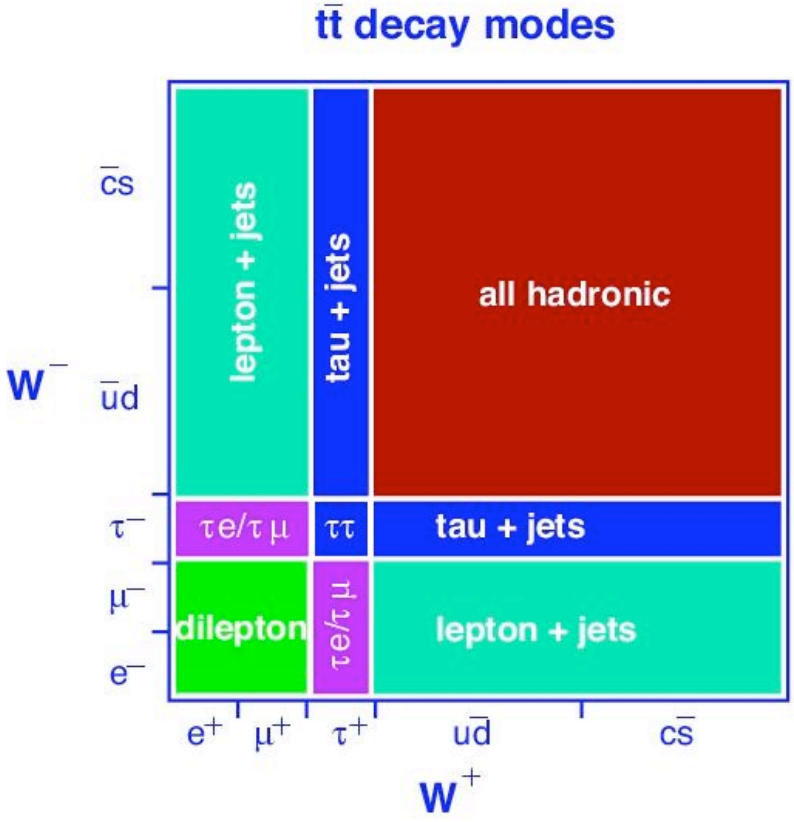

Figure 2.6: The potential decay modes of a SM $t\bar{t}$ event (taken with permission from [26]). The comparative areas of each section reflect the relative branching ratios of the decay modes, where the leptonic W-boson decay is separated in to a decay to $\tau\nu$ and a decay to $e, \mu + \nu$. The fully-hadronic and semi-leptonic decays each encompass 44.4% of the total $t\bar{t}$ decays. The di-lepton channel accounts for 11.1% of $t\bar{t}$ decays.

2.8 Charged Higgs from Top Quark Decays

The production mechanisms for an MSSM charged Higgs boson, H^+, can be loosely separated into two categories, depending on the mass of the H^+. The definition of a 'light' charged Higgs is when four-momentum conservation allows the H^+ to be produced in the decay of a top quark. This limits the charged Higgs mass, m_{H^+}, to $m_{H^+} < (m_t - m_b)$, where m_t and m_b are respectively the top and bottom quark masses. The remaining charged Higgs mass range is attributed to a 'heavy' charged Higgs which, according to theoretical predicions, can be produced in association with a top quark, via the fusion of a gluon and bottom quark. Such heavy charged Higgs processes have small cross sections of the order 1 pb [27], excluding these channels from realistic early data studies at the LHC.

This analysis is concerned with a light H^+, which can be produced as shown in Figure 2.7. The signal channel mimics the Standard Model $t\bar{t}$ decay, with the exception that one W-boson is replaced by a charged Higgs boson. Owing to the large $t\bar{t}$ production cross section at the LHC this channel also potentially has a large cross section, depending on the branching ratio B($t \rightarrow H^+b$). Theoretically, this branching ratio depends on the choice of MSSM scenario, as does the decay mode of the charged Higgs. Figure 2.8 shows the predicted branching ratio $B(t \rightarrow bH^+)$ along with the decay modes for a 100 GeV H^+ as a function of $\tan\beta$, assuming the MSSM benchmark scenario number 1 [19]. At low tanβ the dominant decay of the charged Higgs is to the quark doublet $c\bar{s}$, whilst at high tanβ the decay to $\tau\nu$ is dominant. This analysis is a study of the charged higgs decays to $c\bar{s}$ which is a good candidate decay in the very low tanβ region of the MSSM.

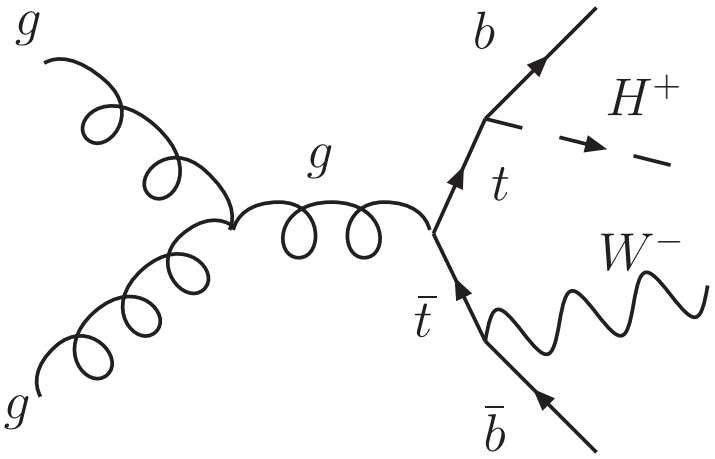

Figure 2.7: The production mechanism for a light charged Higgs boson in a top-quark decay at the LHC.

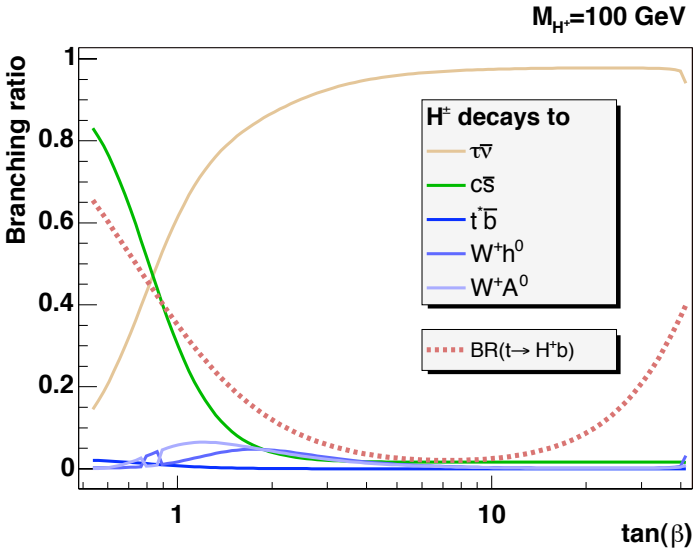

Figure 2.8: The predicted branching ratio $B(t \rightarrow bH^+)$ and the decay modes of the resulting charged Higgs as a function of tanβ [28], assuming the MSSM benchmark scenario number 1, which corresponds to an mSUGRA scenario.

The MSSM benchmark scenario number 1 corresponds to an mSUGRA scenario, but the choice is simply for illustration purposes and this analysis is designed to be independent of the choice of MSSM scenario. Throughout this analysis the branching ratio $B(H^+ \to c\overline{s})$ is assumed to be unity, with the aim of setting limits on the branching ratio B($t \to bH^+$). The results can then be interpreted in any MSSM scenario or, equally, in a non-MSSM context, since the analysis is effectively a search for any charged boson produced in association with a b-quark in the decay of a top quark. A similar analysis has been performed at CDF [13] and the upper limits on B($t \to bH^+$) with 2.2 fb^{-1} of data at 1.96 TeV are shown in Figure 1.1. Due to the comparatively large number of top-pair events expected at the LHC, this is an ideal opportunity for a new physics search with early ATLAS data.

Chapter 3

Experimental Apparatus

3.1 The Large Hadron Collider

The Large Hadron Collider (LHC) [3] is an accelerator and collider facility on the Franco-Swiss border, close to Geneva. Built in the existing 27 km tunnel of the Large Electron-Positron (LEP) collider, the LHC collides beams of protons, but will later be operated with heavy ion beams. Protons are accelerated in bunches and collide at four points around the ring, where the experiments ATLAS, CMS, LHCb and ALICE are situated. The first collisions with stable proton beams at a centre of mass energy, $\sqrt{s}$, of 900 GeV were recorded in ATLAS on 6th December 2009.

The LHC is designed to accelerate each proton beam to 7 TeV, providing collisions with $\sqrt{s} = 14$ TeV. This will be achieved using a series of pre-accelerators. Protons are accelerated to 50 MeV by a linear accelerator, after which the Proton Synchrotron Booster increases the energy to 1.4 GeV. Injection into the Proton Synchrotron and Super Proton Synchrotron accelerators allows the energy to

reach 25 GeV and 450 GeV, respectively. The beam is then injected into the main LHC ring for the final phase of acceleration. The protons are accelerated in bunches by Radio Frequency (RF) cavities. Dipole magnets steer the beams through the curved sections of the beampipe, while the straight sections are equipped with quadrupole focussing magnets.

Since the goal of the experiments is to search for new physics processes, the LHC is designed to provide a large number of events to study. The event rate, R, for a particular process is given by:

$$R = \sigma L \tag{3.1}$$

where σ is the cross section for the process and L is the machine luminosity given by:

$$L = \frac{N_b^2 n_b f_{rev} \gamma}{4\pi \epsilon_n \beta^*} F. \tag{3.2}$$

N_b is the number of particles per bunch, n_b is the number of bunches per beam, f_{rev} the beam revolution frequency, γ is the relativistic gamma factor, ϵ_n is the transverse beam emittance and β^* is the value of the beta function at the particle crossing point. The factor F describes the reduction in luminosity due to the non-zero crossing angle of the colliding particles. The LHC has a design luminosity of 10^{34} cm^{-2}s^{-1}. Such high luminosity precludes the use of proton-antiproton collisions, as preferred by previous collider experiments such as the Tevatron, since it is difficult to produce large numbers of anti-protons. Instead, two separate beampipes allow counter-rotating beams of like-charge particles, which are steered by separate magnet systems.

3.2 The ATLAS Detector

ATLAS is a general purpose detector designed both to study known physics processes with high precision and to search for new phenomena. The detector is described using a right handed co-ordinate system. The x-axis points towards the centre of the LHC ring, the y-axis upwards and the z-axis in the direction of the beamline. Two angular variables complete the description. The azimuthal angle ϕ is measured about the z-axis where zero corresponds to the positive x-axis. The polar angle θ is the angle of elevation from the z-axis, with zero defined by the positive z-axis. The positions of detector components are typically described using the z-co-ordinate and the distance $r_\phi = r\phi$ in azimuthal space, where r is the radial distance from the beamline. In practice, the pseudorapidity, η, is used in place of the polar angle and is given by:

$$\eta = -ln\left(tan\frac{\theta}{2}\right). \tag{3.3}$$

The separation of objects in the detector is commonly described by the distance ΔR in η-ϕ space:

$$\Delta R = \sqrt{(\Delta\eta)^2 + (\Delta\phi)^2} \tag{3.4}$$

and the transverse momentum, p_T, is the scalar momentum perpendicular to the z axis, given by:

$$p_T = p\sin\theta \tag{3.5}$$

where p is the particle momentum.

The layout of the ATLAS detector is shown in Figure 3.1, and the various sub-detectors are optimised to measure different particle properties. Closest to the beam pipe is the Inner Detector. This is surrounded by the calorimeters which are, in turn, surrounded by the muon chambers. The design requirements can be summarised by the following [15].

- A detector that is fast, radiation-hard and highly granular in order to precisely record large rates of events with high particle multiplicity.
- Good coverage up to high η and, as much as possible, full coverage in ϕ.
- A tracking detector with high efficiency and good momentum resolution over a wide range of particle momenta. Very precise position measurements are required close to the interaction point for use in vertex reconstruction. These requirements must be achieved with the minimum possible material in order to reduce the energy loss of particles before the calorimeters.
- Good electromagnetic calorimetry for electron and photon reconstruction, and good coverage in the hadronic calorimeter to accurately measure the jet activity and missing energy in the detector.
- Good muon momentum resolution over a wide range of muon momenta, and excellent charge sign identification even at large muon momenta.
- A fast, efficient trigger with good background rejection.

The sub-detectors and trigger system are described in detail in the following sections.

3.2.1 The Inner Detector

The Inner Detector [29], shown schematically in Figure 3.2, is designed to efficiently reconstruct charged particle tracks above a nominal threshold of 0.5 GeV and to provide some basic particle identification. Covering the range $|\eta| < 2.5$, the Inner Detector is contained within a cylindrically shaped envelope of length 7024 mm, radius 1150 mm and comprises three subdetectors. The pixel detector

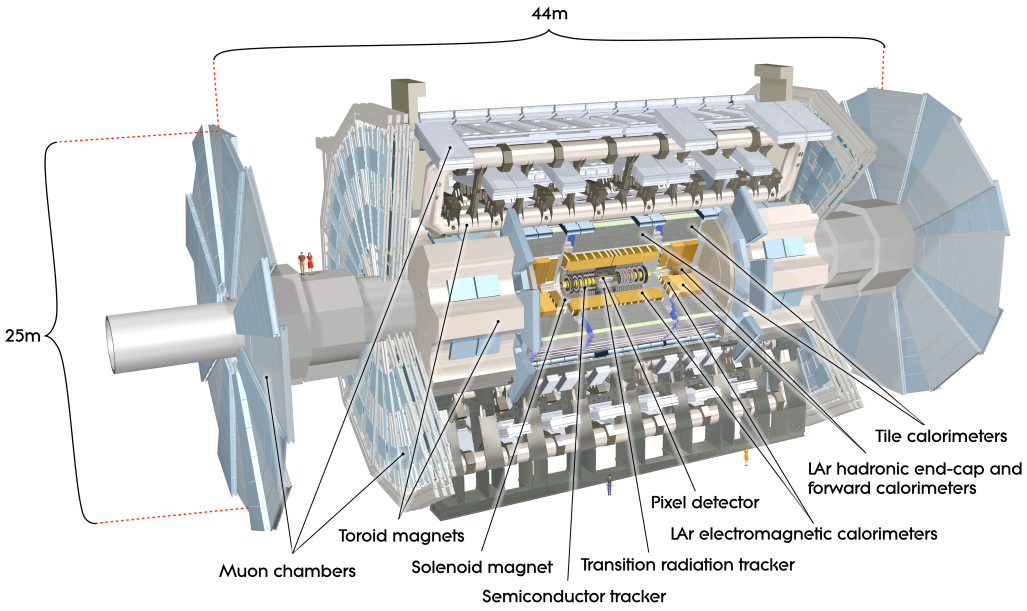

Figure 3.1: Cut away view of the ATLAS detector [15].

is closest to the beamline. This is surrounded by the Silicon Tracker (SCT), while the outermost detector is the Transition Radiation Tracker (TRT). Each subdetector is split into three components - a central barrel region and two endcaps. The entire Inner Detector is enclosed within a 2 T superconducting solenoid magnet, which provides an homogeneous magnetic field. The trajectory of a charged particle is bent in the presence of the field and the momentum and charge of the particle can be deduced from the radius of curvature of the measured track.

Both the pixel and SCT detectors are based on silicon technology. Charged particles entering the silicon create electron-hole pairs due to the excitation of a valence band electron to the conduction band. An applied electric field allows the charges to be collected on the surface of the silicon. The pixel detector has a high granularity and is designed to record precise information about particle trajectories very close to the beampipe, allowing accurate reconstruction of the decay vertices. It consists of 1744 identical sensors, each containing 47232 pixels of size 50×400 μm^2 spread over the three barrel layers and three layers in each

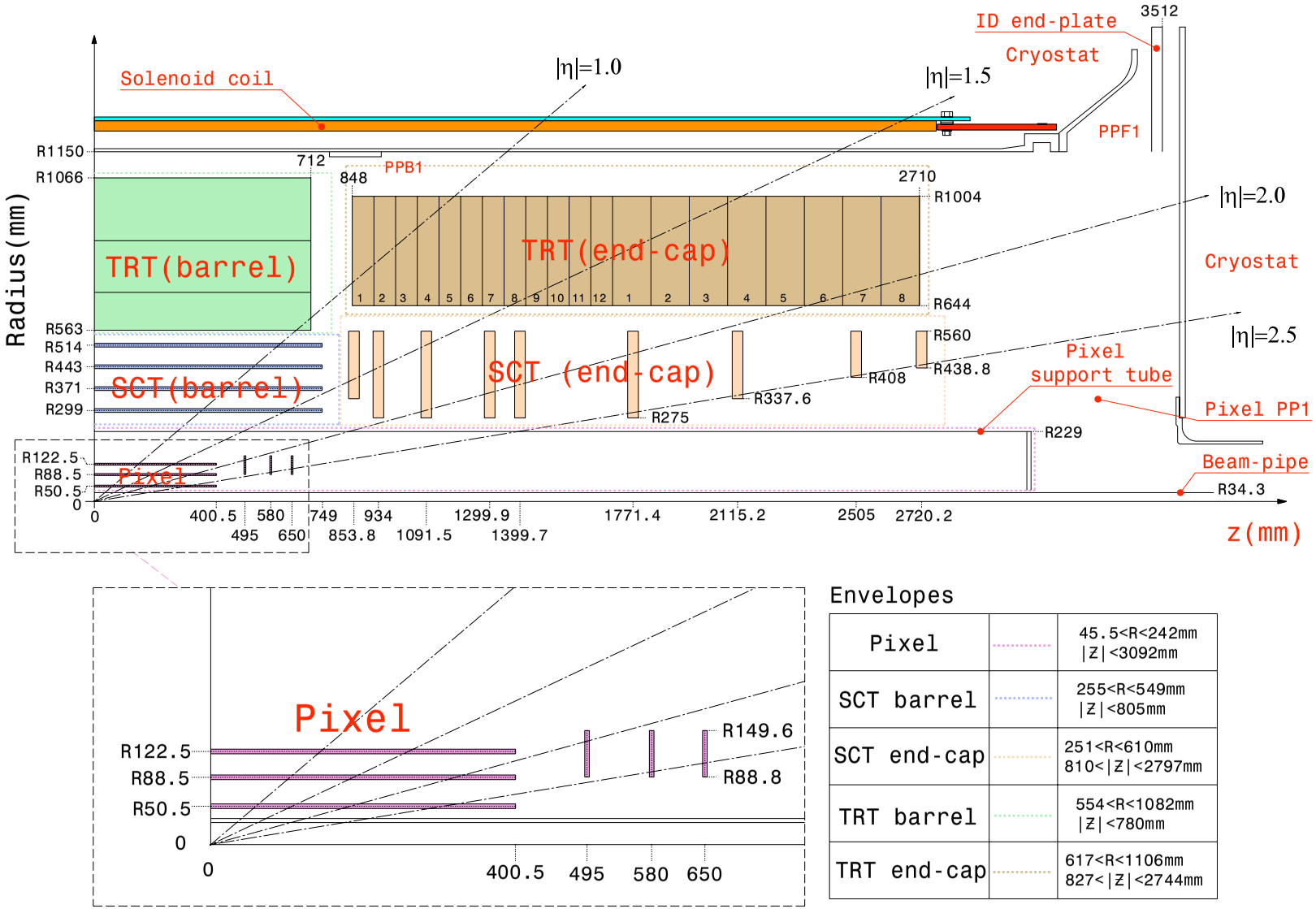

Figure 3.2: Schematic diagram of the ATLAS Inner Detector.

endcap. The intrinsic accuracy of the barrel pixels is 10 μm in r_ϕ and 115 μm in z and for the endcap pixels, 10 μm in r_ϕ and 115 μm in R. Due to the extreme proximity to the beamline, the pixel detector is expected to be very susceptible to radiation damage, particularly in the first layer which is known as the b-layer. The silicon is cooled to between -5 and -10 degrees C in order to optimise the signal to noise ratio, and the bias voltage is expected to increase from 150 V to 600 V as the charge collection efficiency degrades.

For cost purposes, the pixel detector is limited to three layers. The SCT is, instead, constructed from 15912 sensor modules, each containing 768 silicon strips with a length of 12 cm, and a strip pitch of 80 μm. Since a silicon strip can only provide a precise measurement in one direction, pairs of strip layers are bonded back to back, with a stereo angle of 40 mrad. This information, together with the global position of the module, provides a three-dimensional hit position. The intrinsic accuracy of each pair of strips in the barrel is 17 μm in r_ϕ and 580 μm in z. In the endcap it is 17 μm in r_ϕ and 580 μm in R.

The TRT detector is based on drift tube technology, and consists of tubes of 4 mm diameter arranged in the z-direction for the barrel, and radially for each endcap. The straws have walls of thickness 70 μm, and are filled with a $Xe/CO_2/O_2$ gaseous mixture. The straw anode is a 31 μm diameter tungsten wire, plated with gold. Owing to the alignment of the straws, the TRT detector only provides an R-ϕ measurement in the barrel, and a z measurement in the end-caps. The intrinsic resolution of each straw is 130 μm. The TRT measurements serve two purposes. The large number of additional track hits are invaluable for a precise momentum measurement, but the TRT information is also used for particle identification. Transition radiation photons can be emitted when a particle crosses the boundary between two media with different dielectric constants. The

radiated energy is proportional to the Lorentz factor, γ, of the incident particle [30], with a lower cut off around $\gamma = 1000$. The TRT detector records two types of hit information. A high-threshold hit results from a large energy deposit in a given straw, and typically occurs when transition radiation has been emitted. Low-threshold hits are due to smaller energy deposits, and are used to gain additional track hits. Together with the measured momentum, the high-threshold information can be used to infer the particle mass, and this method is particularly well suited to distinguish between highly relativistic electrons and charged pions.

A charged particle typically leaves three pixel hits, eight SCT layer hits, and around 36 TRT hits. Pattern recognition software is used to reconstruct the tracks, and is described in detail in Chapter 4.1. From Monte Carlo studies [31], the resolution on the inverse momentum, $1/p_T$, of a track is expected to be

$$\sigma_{1/p_T} = 0.34\ TeV^{-1}(1 \oplus \frac{44\ GeV}{p_T}) \tag{3.6}$$

where p_T is expressed in units of GeV. The first term represents the intrinsic resolution at infinite momentum, and the second term the multiple scattering component, which is small for high p_T tracks.

3.2.2 The Calorimeters

The ATLAS calorimeter system [32] is made up of an electromagnetic calorimeter and a hadronic calorimeter, both of which use sampling methods to measure the energy of an incident particle. Thin absorbing layers induce showers of particles inside the detector. These are alternated with sampling layers that measure the energy deposits due to the shower, from which the energy of the original particle can be inferred. Calorimeter measurements are necessary to reconstruct electrons, photons, jets of particles from the hadronisation of partons, and to measure

the missing transverse energy, E_T^{miss}, in an event. Energy deposits associated with muons can also be used to correct the muon energy measured by the muon spectrometer.

Electromagnetic Calorimeters

The electromagnetic calorimeter (ECAL) is designed to measure the energy of electrons and photons. Lead absorbing planes are interleaved with liquid argon (LAr) sampling layers, which contain copper readout electrodes. On entering the ECAL, electrons and photons undergo electromagnetic interactions, causing electrons to emit bremsstrahlung radiation and photons to produce electron-positron pairs. This process is known as electromagnetic showering. Inside the sampling layers, the electrons cause ionisation of the LAr, and the resulting charge is collected by a set of electrodes. The planes of lead and LAr have an accordion geometry, which optimises the detector coverage in ϕ.

A barrel region covers the range $|\eta| < 1.475$ and is constructed from two half-barrels, separated by a 4 mm gap in z. The total thickness ranges between 22 and 33 radiation lengths, X_0, depending on η. Two endcaps cover the range $1.375 < |\eta| < 3.2$. Each endcap consists of two wheels; an outer wheel covers the range $1.475 < |\eta| < 2.5$ and an inner wheel covers $2.5 < |\eta| < 3.2$. The total active thickness ranges between 24 and 38 X_0 depending on η. The ECAL is segmented into cells whose size govern the granularity of the detector. In the barrel region, the cell size in η-ϕ-space is 0.025×0.1 in the first layer, 0.025×0.025 in the second layer and 0.05×0.025 in the third layer. In both the barrel and endcaps, the finest granularity is in the second layer, where the majority of the energy is deposited. On reaching the ECAL, a particle has traversed the beampipe, the Inner Detector and additional material related to detector services. Interactions

with this material may have already caused the particle to lose energy. A layer of LAr just inside the ECAL is used as a pre-sampler to estimate this energy loss, and covers the range $|\eta| < 1.8$ with a granularity of 0.025×0.1 in η-ϕ space.

An electromagnetic shower will deposit energy in several neighbouring calorimeter cells, and the energy of a particle is calculated by clustering together these cells. The resolution on the energy, E, of a particle reconstructed by the ECAL can be parameterised as:

$$\frac{\sigma_E}{E} = \frac{a}{\sqrt{E(GeV)}} \oplus b \tag{3.7}$$

where a is a sampling term, quoted with units of % $GeV^{-1/2}$ and b is a constant term, (%) describing non-linearities in the calorimeter response. Test-beam studies of barrel modules using electrons and positrons at $\eta = 0.687$ found the sampling term to be 10% and the constant term to be 0.17% [32], corresponding to an uncertainty of 3.2% for 10 GeV electrons and 1% for 100 GeV electrons. The resolution varies as a function of pseudorapidity.

Hadronic Calorimeters

The hadronic calorimeter (HCAL) is a sampling calorimeter designed to measure the energies of hadrons, and is situated directly outside of the ECAL. The barrel region covers $|\eta| < 1.0$ and two extended barrel regions span $0.8 < |\eta| < 1.7$ using steel as the absorbing material and 3 mm polystyrene scintillator tiles to sample the shower development. Shower particles passing through the tiles produce ultraviolet light, which is collected at the edges of the tiles. Wave-length shifting fibres reduce the frequency to a known value in the visible spectrum, and the signal is read out using photomultiplier tubes. The hadron energy is then inferred from this signal. The endcaps cover $1.5 < |\eta| < 3.2$ using copper absorbing

plates separated by LAr sampling regions, and operate in a very similar way to the ECAL.

The energy resolution can be parametrised using Equation 3.7. Test-beam studies of the tile calorimeter using charged pions found the sampling term to be 56.4% and the constant term to be 5.5%, for $\eta = 0.35$ [32]. This can vary with η, largely due to the varying effective depth of the calorimeter material.

Forward Calorimeters

The forward calorimeters (FCals) [33] are designed to measure particles at very high η, and are vital for a robust measurement of the E_T^{miss}. They also provide natural shielding for the muon detectors from beam backgrounds. Two FCals cover the range $3.2 < |\eta| < 4.9$, and each is separated into three modules. The first module (FCal1) performs electromagnetic calorimetry, and the remaining two (FCal2 and FCal3) are hadronic modules. The forward calorimeters are subject to a high flux of particles and use LAr technology with rod-shaped copper electrodes. In FCal1 the LAr gaps are 0.27 mm, to avoid the build-up of charge in the material, and to decrease the signal collection time. The LAr gaps increase to 0.37 mm in FCal2 and 0.51 mm in FCal3, where the density of ionising particles is smaller.

3.2.3 The Muon Spectrometer

Muons leave a track in the Inner Detector but, as minimum ionising particles, typically deposit very little energy in the calorimeters. The muon spectrometer [34] is designed to measure the momentum and charge sign of muons, using the radius of curvature of charged tracks that are bent by an external magnetic

field. The muon spectrometer is split into a barrel section extending to $|\eta| < 1.0$, and two endcap regions covering $1.0 < |\eta| < 2.7$. Muons can be tracked over the range $|\eta| < 2.7$ and the detector modules are divided into a set of precision measurement chambers, and a set of dedicated fast trigger chambers. The bending field is provided by air core toroid magnets, with the barrel and endcap toroids producing fields of approximately 0.5 T and 1 T, respectively. The toroid field is inhomogeneous, particularly in the transition region between the barrel and endcap magnets.

The majority of precision tracking hits are provided by the Monitored Drift Tubes (MDTs). MDTs consist of aluminium tubes of diameter 30 mm, filled with a gaseous mixture of $Ar/C0_2$. Ionisation electrons are collected by a 50 μm gold-plated W/Re wire running through the centre of each tube, which provides a drift time measurement. Each tube has an intrinsic resolution of 80 μm and gives a measurement in the bending (η) plane. The muon detector is organised in stations; in the barrel region there are three stations arranged in concentric cylinders around the beampipe at radii of 5 m, 7.5 m and 10 m. A station consists of 8 chambers, each of which is a symmetrical segment in ϕ. Chambers are made up of layers of MDTs and can contain between 3 and 8 layers, depending on the chamber position. In the endcaps there are four stations, with each segment containing between 6 and 8 MDT layers. In the innermost endcap station, the coverage of the MDTs is restricted to $|\eta| < 2.0$ due to performance limitations in this region of high occupancy.

Cathode Strip Chambers (CSCs) are used for precision measurements in the forward region, and cover the region $2.0 < |\eta| < 2.7$ in the innermost station of each endcap. The CSCs are multi-wire proportional chambers. Anode wires run radially outwards, perpendicular to the beampipe, with a set of cathode strips perpendicular to the wires. The wires are surrounded by a gaseous mixture of

$Ar/C0_2$. Electrons collected on an anode wire induce a charge distribution on the cathode strips. A precision measurement is determined by interpolating the charge distributions on nearby strips. A second set of strips running parallel to the wires provides a transverse measurement. In both endcaps, the CSC station is split into eight chambers, where each chamber consists of four CSC planes. The intrinsic resolution of the CSCs is 60 μm.

The muon trigger system is designed to provide fast and robust information about particle trajectories, in order to identify events that potentially contain muons. In the barrel, Resistive Plate Chambers (RPCs) are used. These consist of two parallel electrode plates filled with a gaseous mixture of $C_2H_2F_4$/Iso-C_4H_{10}/SF_6. The plates are separated by 2 mm, and an applied potential of 4.9 kVmm^{-1} leads to electron avalanches along the particle tracks. Perpendicular metallic strips read out an η and ϕ measurement from each layer. There are three trigger stations, each consisting of two RPC layers. The endcap trigger is formed from Thin Gap Chambers (TGCs), which are based on the same principles as a multi-wire proportional chamber. The TGC wires are separated by 1.8 mm and cover the range $1.0 < |\eta| < 2.4$, meaning that the muon trigger does not cover the full η range of the muon spectrometer. The wire signals provide a measurement of η, while the ϕ co-ordinate is determined from the induced signals on the pickup strips.

The three-level trigger system is described in more detail in Section 3.2.4, but the time avaliable to make a trigger decision for each event precludes the use of tracking algorithms at the first level of the muon trigger. The initial decision is, instead, based on hit co-incidences, which are required separately in η and ϕ in order to reduce backgrounds. The decision is then refined in the other levels of the trigger system. Muon trigger measurements from both the RPCs and TGCs also provide the precision tracking co-ordinate in the non-bending (ϕ) plane to

complement the precision η measurement from the MDTs.

3.2.4 Triggers and Data Acquisition

The Standard ATLAS Trigger System

At design luminosity of 10^{34} cm^{-2}s^{-1}, ATLAS will see a bunch crossing rate of 40 MHz. However, the maximum rate at which events can be written out is around 300 MBs^{-1}, corresponding to an event rate of around 200 Hz. The vast majority of proton-proton collisions will result in soft QCD events; the cross sections for new physics processes or the production of particles such as the top quark will be many orders of magnitude smaller. The ATLAS trigger [35] is a three-level system, designed to reduce the output event rate to a managable size, whilst selecting the desirable physics events to store. The Level-1 trigger uses custom-made hardware to make an initial decision. The software-based high level trigger (HLT) comprises the Level-2 trigger and the Event Filter, and further refines the decision made at Level-1.

At Level-1 the initial interaction rate is reduced to an output rate of 75 kHz, with 2.5 μs available to accept or reject each event. The decision is based on reduced granularity information from the calorimeters and the muon spectrometer. Information from the Inner Detector cannot be accessed on this timescale. In the calorimeters, candidate high E_T objects such as electrons/photons and jets are identified using sliding window algorithms that locate clusters of energy deposits. Isolation requirements can be imposed to veto clusters that are not well separated from surrounding energy deposits. A measurement of the total transverse energy, E_T, is also performed. The electron/photon and tau triggers cover the range $|\eta| < 2.5$, while the jet triggers extend to $|\eta| = 3.2$. The muon

trigger uses hit information from the dedicated RPC and TGC trigger chambers. The presence of a muon is inferred by comparing patterns of chamber hits with pre-defined look-up tables, and the muon trajectory is required to be consistent with the interaction point. The resulting calorimeter clusters and muon candidates are compared to a set of pre-programmed energy thresholds. The Level-1 trigger decision is made by the Central Trigger Processor (CTP) which considers only the multiplicity of trigger objects passing each energy threshold. A trigger menu, in which up to 256 items can be defined, contains combinations of object requirements, designed to select events of interest such as those containing high p_T and/or isolated objects. If an event satisfies the criteria of any of the menu items, the entire detector information is read out, and the position of each trigger object is recorded as a Region of Interest (RoI) in $\eta - \phi$ space. For many triggers, and particularly at high luminosity, the rate of events selected at Level-1 can exceed the available bandwidth. Events can be randomly rejected before the event is read out in a process known as prescaling. The rejection rate for a particular trigger is pre-defined; for example, a prescale of three means that only one in three events passing at Level-1 are sent to Level-2 for further processing.

The Level-2 and Event Filter triggers consist of fast algorithms run on dedicated farms of computers, and have access to information from all ATLAS subdetectors. The Level-2 trigger is seeded by the RoI from Level-1 and only considers data within this RoI. The processing time is around 40 ms per event with an output rate of around 3.5 kHz. Algorithms search for features within the RoI, such as Inner Detector tracks, calorimeter clusters or muon spectrometer tracks, and matching between features in different sub-detectors can be used to identify physics objects such as electrons or jets. The Event Filter further refines the Level-2 result, and reduces the output rate to around 200 Hz. The Event Filter algorithms are the same as those used for the full offline event reconstruction,

although the details of the configuration at run-time allow the algorithms to run on the RoI and to limit the processing time to within a few seconds per event.

Early Data Triggers

Early data analyses, such as the performance studies described in Chapter 4 will study the same QCD events that the standard triggers are designed to reject. This will require inelastic collisions to be triggered with as little bias as possible, giving a sample of events known as minimum bias events. The Minimum Bias Trigger Scintillators (MBTS) [36] are designed for use in very low luminosity running and consist of two wheels of polystyrene-based scintillator counters. Each wheel is 2 cm thick and mounted on the inside surface of the liquid argon endcap cryostats. Each wheel contains eight segments in azimuth of $\pi/4$, and two sections in η ($2.12 < |\eta| < 2.83$ and $2.83 < |\eta| < 3.85$). The MBTS use the tile calorimeter electronics to read out a fast signal which is used by the CTP to make a decision on the event at Level-1.

The Beam Pickup Timing detectors (BPTX) [37] are electrostatic devices situated 175 m upstream and downstream of the interaction point, and are designed to detect the presence of proton bunches entering ATLAS. The primary use of the BPTX information is to monitor the beam structure and the timing signals provided by the LHC machine. However, it also provides a Level-1 trigger input in the form of the time of each bunch passing through the detector. For example, the BPTX information can be combined with a random trigger at Level-1 to record an unbiassed set of events. However, until the luminosity reaches around 10^{32} $\mathrm{cm}^{-2}\mathrm{s}^{-1}$ this trigger will have a very low efficiency, since the majority of bunch crossings will not contain an inelastic proton-proton collision.

Minimum bias events are recorded in ATLAS using Level-1 trigger items based

on the MBTS information. The trigger menu allows for various combinations of MBTS hits to be used. The least biassed trigger requires only one hit in the scintillators, while noise can be suppressed by requiring different combinations of coincident hits. However, during the first few weeks of data-taking at 900 GeV, when the detector timing was not optimised, the MBTS hits were used in conjunction with the BPTX information to ensure that the trigger was fired on a real bunch crossing.

Chapter 4

Event Filter Tracking Studies

In collider experiments it is important to design appropriate triggers with high efficiency and purity, in order to maximise the number of recorded signal events. The charged Higgs events described in Section 2.8 can be triggered using single electron or single muon triggers. These will be especially relevant in early data studies, when more complicated triggers, such as those based on missing transverse energy in the detector, are not well understood. An efficient electron or muon trigger requires good tracking of charged particles in the Inner Detector, despite the time constraints imposed by the trigger decision. At Level-1, tracking information is not used, as the latency is too short to access the data from the pixel and SCT detectors. Tracking in the ATLAS trigger begins at Level-2 and is further refined by the Event Filter. This chapter describes the structure of the Event Filter Inner Detector tracking software, and performance studies using both cosmic ray and collisions data. These studies were important to the commissioning of the electron and muon triggers used for the charged Higgs analysis, and formed an essential contribution to the infrastructure of the ATLAS experiment.

4.1 Event Filter Tracking Algorithms

The high luminosity of the LHC will present a challenging environment in which to search for tracks. The standard track finding strategy in ATLAS is known as inside-out tracking, and exploits the high granularity hit information from the pixel and SCT detectors. The reconstruction begins with these 'silicon' hits, and the track is later extended in to the TRT detector if appropriate. A complementary back-tracking method beginning in the TRT detector and extending into the silicon detectors can also be used to improve the efficiency to reconstruct tracks from photon conversions or secondary particles. Common tracking software known as New Tracking (NewT) [38] is shared between the Event Filter and the offline reconstruction. In the Event Filter, the NewT algorithms are typically run in a Region of Interest (RoI) based mode, as described in Section 3.2.4, and have access to the full granularity data inside each RoI.

The NewT algorithms take the detector hit information and provide the optimum set of tracks. The software has a modular structure. Firstly, tracks are seeded from the silicon hit information and refined using fitting algorithms. Track extension to the TRT detector and vertex finding are performed in later algorithms. This reduces processing time since, in events where high quality silicon tracks are not found, later algorithms are not executed. Each module is described briefly below, together with the main simplifications required to meet the total processing time of a few seconds per event allotted to the Event Filter.

4.1.1 Tracking Co-ordinate System

A charged particle in a uniform magnetic field follows a helical path. The resulting track can be defined in a frame where the z-axis is parallel to the direction of the

solenoid field, and is fully described by the following set of parameters:

- d_0 = transverse impact parameter, the distance of closest approach (perigee) of the helix to the nominal interaction point in the transverse direction.
- z_0 = longitudinal impact parameter, the distance of closest approach of the helix to the nominal interaction point in the z-direction.
- ϕ_0 = the azimuthal angle of the track at the distance of closest approach, in the range [-π,π].
- θ = the polar angle of the track in the range [0,π].
- $\frac{q}{p_T}$ = the charge over transverse momentum.

These parameters are illustrated in Figure 4.1. Since the solenoid field provides a uniform magnetic field in the z-direction, any track is bent solely in the azimuthal direction. For this reason, the track ϕ must be specified at the distance of closest approach to the interaction point. The track θ is not changed by the magnetic field.

4.1.2 Silicon SpacePoint Formation

Silicon hit information from the SCT and pixel detectors is used to create SpacePoints, which are used for track seeding. Each SpacePoint is a simple three-dimensional co-ordinate that can be accessed quickly. This reduces the processing time associated with track seeding which, with a high detector occupancy, can be time consuming due to the large number of combinatorial possibilities. Each pixel hit can easily be interpreted as a three-dimensional measurement. However, since no precise measurement is recorded in the direction of each SCT strip, hits

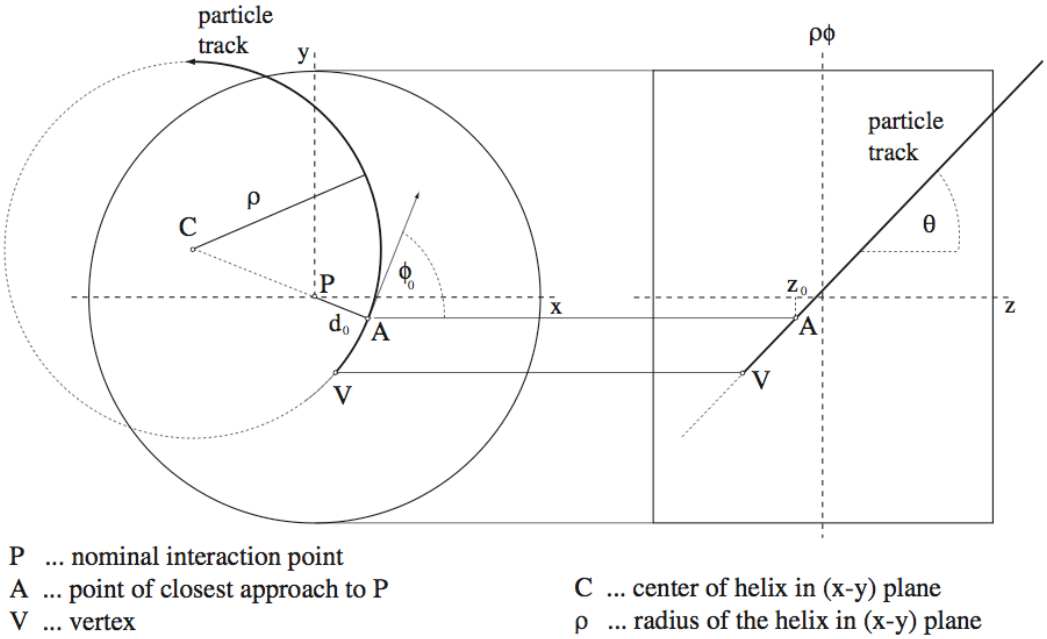

Figure 4.1: Pictorial representation of the helical track parameters, taken with permission from [39]. The transverse parameters d_0 and ϕ_0 are shown in the x-y plane, in which the track is curved. The longitudinal parameters z_0 and θ are shown in the $\rho\phi - z$ plane, in which the track is a straight line.

on two back to back strips are used to give one SpacePoint. Noise masking is used to remove hits from known noisy detector elements, and the maps of these modules are constantly evolving. Since the offline track reconstruction takes place several hours after data-taking, accurate noise maps can be used to reflect the run-time performance of the detector. However, in the online environment it is not possible to update the module masking as frequently, and the Event Filter tracks can show evidence of detector noise.

4.1.3 SpacePoint Seeded Track Finding

Track seeding is initiated by pairing together different combinations of SpacePoints; each pair gives a predicted z-coordinate for the primary vertex position. A histogram of these vertex candidates allows a fast primary vertex algorithm to select the most likely vertex. Track seeds are rejected if they are incompatible with this vertex, and additional SpacePoints are added to the track seeds. Unwanted seeds can be removed at this stage. The cuts used are highly configurable, but typically reject seeds with very low p_T. Seeding can also be performed without the z-vertex constraint, which is a more time consuming process. This is useful for events where the primary vertex cannot be well-measured, and is also designed to be used in heavy-ion collisions. After the initial track seeding, the SpacePoints are superseded by the original detector hit information and the direction of each track seed is used to build a road of detector elements within which to search for additional track hits. Any hits within the road, which is typically around 20 mm in width, are used for the following track fitting.

4.1.4 Track Candidate Selection and Track Fitting

Seeded track-finding leads to a large number of track seeds, and there are several algorithms available to fit each track. In the Event Filter, a global χ^2 algorithm [40] is used, although various options are available including a Kalman Filter [41]. A scoring technique is used to distinguish between good and bad tracks, where different track features are assigned either a positive or negative score. An example of track seeds in the SCT detector is shown in Figure 4.2. A large number of hits associated with a track candidate gives a beneficial score in order to preferentially find complete, rather than incomplete, tracks. Penalties

are incurred for hits missing along the track trajectory and, in general, the scores are weighted in favour of the high precision pixel hits. If a hit is shared between two tracks it is generally given to the track with the highest score, while the additional track is re-fitted without the hit. The details of the ambiguity solving are configurable. The process is iterated, and quality cuts remove low scoring tracks.

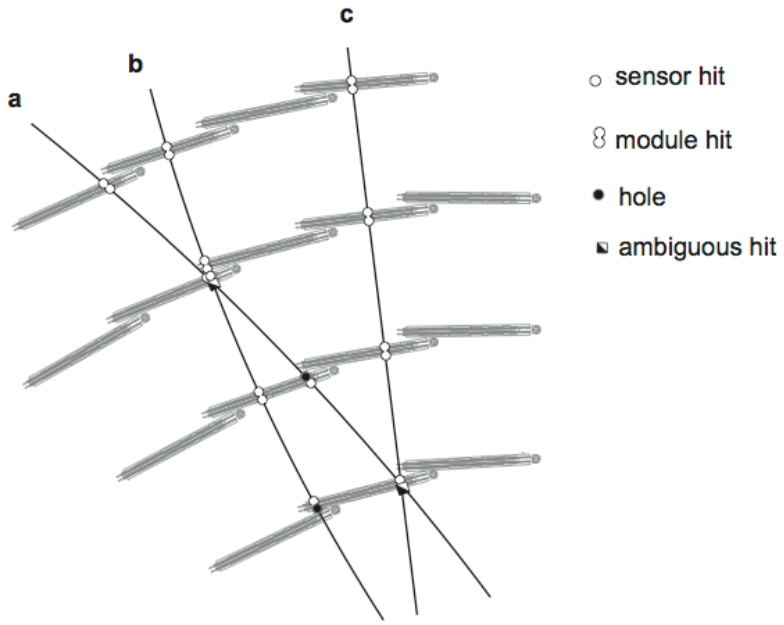

Figure 4.2: Three potential track seeds passing though the SCT detector, taken from [38]. In this case, a comparison of track χ^2 values is not sufficient to select the correct tracks. Sensor hits show a hit in one of the two SCT layers for a particular module. Module hits show points with hits in both SCT layers. A hole is a missing hit along a track trajectory, while ambiguous hits could potentially belong to multiple tracks. The scoring technique is used to rank the tracks.

4.1.5 TRT Track Extension

The reconstructed silicon tracks are extrapolated into the TRT, and a road-finding method is used to locate compatible TRT hits. If a possible TRT extension is found, the original silicon track is re-fitted to include the TRT hits, and the track scoring method described in Section 4.1.4 is used to compare the original silicon track to the refitted track. During the re-fit, silicon hits can be flagged as outlying measurements if they are no longer compatible with the refitted track. This, however, leads to scoring penalties, since additional silicon holes are introduced on the track. The track with the highest score is retained, meaning that the TRT hits are only used if they lead to an improvement in the track score.

4.1.6 Post Processing

Once the tracks have been optimised, the vertices are reconstructed and, finally, the Event Filter tracking information is stored. Several vertex reconstruction methods are available [42], falling into two categories. In the first category, the vertex finding and vertex fitting are decoupled. After applying track quality cuts, a sliding-window algorithm is used to bunch tracks together according to their measured value of z_0. Each bunch forms a potential primary vertex candidate, whose position is then fitted, typically using a χ^2 minimisation. Outlying tracks can be removed with a configurable cut on their contribution to the χ^2, and are not considered for any other vertex candidate. In the second category, a 'finding through fitting' approach is used, where a single vertex seed is created from all pre-selected tracks. The vertex position is fitted and outlying tracks are used to create a second vertex seed. The process is iterated and the number of vertex candidates grows with each iteration, with the vertices competing for the tracks.

The output of all vertex finding methods is a set of fitted vertices, from which the primary vertex must be selected. This is typically based on the number of tracks associated with each vertex, and the transverse momentum of the tracks.

To reduce the event size, detector hit information is not stored for the Event Filter tracks. Instead, a vector of the track trajectory is created and only low level information is stored, such as the number of hits on the track from each sub-detector and the perigee parameters.

4.2 Studies with Cosmic Ray Data

4.2.1 Data Set

In June and July 2009, over 90 million cosmic ray events were recorded by the ATLAS detector. Cosmic protons interact with atmospheric particles, leading to particle showers. In general, these particles are absorbed by the atmosphere and the earth before reaching the detector. However, muons, which cannot interact via the strong interaction and have a low probability to emit bremsstrahlung radiation, are less readily absorbed and are thus observed in the detector. Cosmic ray data provided a valuable opportunity to test the performance of the Event Filter tracking before collision data became available. The tracking algorithms used were very similar to the standard inside-out tracking described in Section 4.1. However, some modifications allowed tracks to be reconstructed far away from the nominal interaction point, and for a single track to be fitted across the entire Inner Detector. In addition to the inside-out tracking, a TRT-only tracking strategy was employed, using only hits from the TRT detector to reconstruct tracks. In this study we focus on the tracks from the inside-out tracking, since this is the

main tracking mode used to reconstruct collision events.

The events considered were triggered using the TRT Fast-OR Trigger [43], a Level-1 trigger based on the TRT electronics. The TRT is split into trigger segments, each consisting of around 200 straws. A high-threshold hit in any straw is recorded as a trigger hit in that segment, and the trigger is fired if there are trigger hits in four adjacent segments. The TRT high-threshold was set to 1 keV, substantially below the threshold for transition radiation but high enough to avoid noise hits. The TRT low-threshold was set to 200 eV to record the maximum number of hits for tracking purposes. In this configuration, the TRT does not distinguish between transition radiation and minimum ionising hits. Only the high-threshold hits were used for the trigger decision, to maintain a manageable rate, but both the high and low-threshold hits were used for track reconstruction in the TRT. This trigger provided approximately 8 Hz of events in the barrel, a large fraction of which contained tracks with silicon hits. Due to the low granularity of this trigger, it is only suitable for triggering in an environment with low charged particle density and is not intended to be used during collision data-taking. The HLT tracking algorithms were run online but not used for the trigger decision, allowing performance studies to compare the HLT tracking with the offline reconstruction. Due to the low track occupancy and low rate of cosmic events, the Event Filter was run in a 'Full Scan' mode, where the RoI was defined to be the size of the detector acceptance.

4.2.2 Track Parameter Studies

Event Filter tracks were required to have at least one silicon hit associated with the track, to reject tracks from the TRT-only tracking. Figure 4.3, shows the

d_0, z_0, η and ϕ[1] of the selected tracks [44]. In each plot, noisy detector modules can be seen as spikes in the parameter distributions. Such spikes are not seen in the equivalent distributions from the offline tracking, since the delay between data-taking and reconstruction allows accurate masking of noisy modules to be used. However, these noise spikes should not be interpreted as the performance of the Event Filter in a collision data-taking scenario. During cosmic data-taking, the Event Filter tracking was run in a loose configuration and was not optimised for the rejection of fake tracks. For this reason, noisy modules can have a much larger impact than in the nominal track reconstruction used for collision events.

With the exception of noise spikes, the distribution in d_0 is relatively flat and falls, as expected, far from the nominal interaction point. Tracks with $|d_0| > 300$ mm cannot have hits in any pixel layer, or the inner layer of the SCT. A similar effect is seen in z_0, where the drop around $|z_0| = 700$ mm corresponds to the edge of the SCT barrel. The η distribution is strongly peaked around η = -0.4, which corresponds to the position of the main access shaft. The asymmetries in this distribution can be attributed to the positions of the additional elevator shafts in the cavern. The ϕ distribution shows a peak at $-\frac{\pi}{2}$, since the majority of cosmic particles enter the cavern from directly above the detector. The small number of tracks with positive ϕ originate from events where two independent tracks were fitted for a single cosmic ray muon.

4.2.3 Track Reconstruction Efficiency

The cosmic tracks from the offline reconstruction were used as a reference to measure the reconstruction efficiency for Event Filter tracks. All offline and Event

[1]Throughout this chapter the variable ϕ is used to refer to the value of the azimuthal angle at the perigee, ϕ_0.

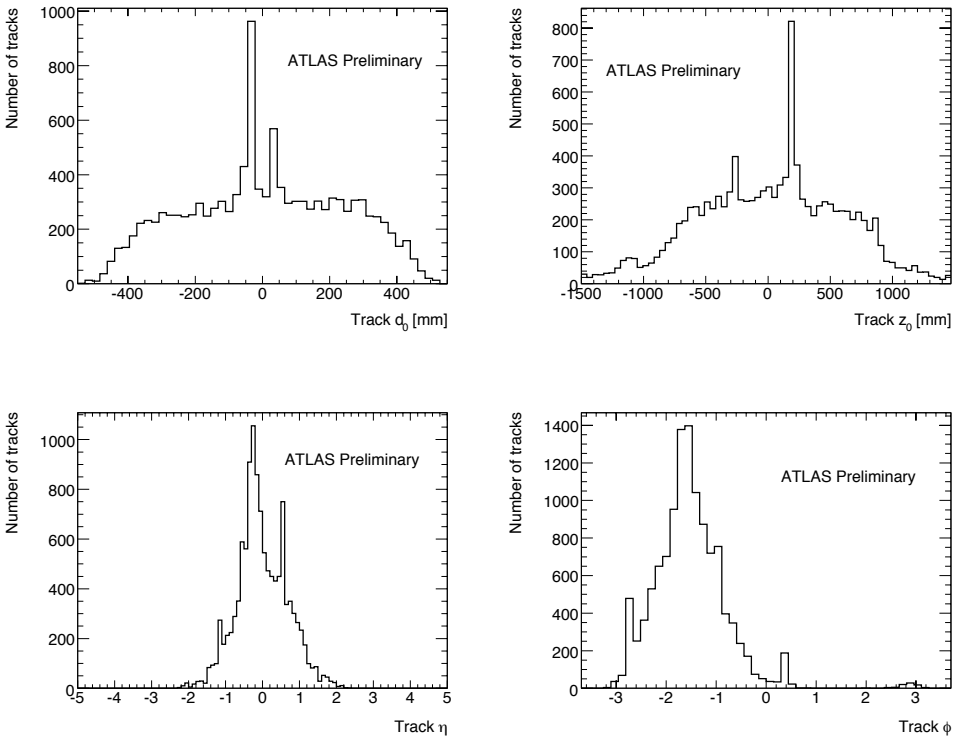

Figure 4.3: The track parameters d_0, z_0, η and ϕ of Event Filter tracks in 100k events recorded with the solenoid field on. All tracks shown originate from the inside-out tracking.

Filter tracks with at least one silicon hit were selected. A set of loose, medium and tight quality cuts were then applied to the offline tracks, where the 'tight' criteria were designed to select tracks that closely resemble the expected tracks from collision data. These cuts are shown in Table 4.1. A matching algorithm was used to associate each offline track with the closest Event Filter track in ΔR, where ΔR is given by:

$$\Delta R = \sqrt{\left(\eta_{offline} - \eta_{EF}\right)^2 + \left(\phi_{offline} - \phi_{EF}\right)^2}. \tag{4.1}$$

$\eta_{offline}$, $\phi_{offline}$, η_{EF} and ϕ_{EF} are respectively the pseudorapitity and azimuthal angle of the offline and Event Filter tracks. Each offline track was used in turn with each Event Filter track to calculate the value of ΔR. For each offline track, all Event Filter tracks were stored in order of smallest ΔR. After exhausting all combinations, the best matched track pairs were checked for overlaps. In the case that two offline tracks were best matched to the same Event Filter track, the pair with the smallest ΔR was retained, and the remaining offline track was associated with the second-best matched Event Filter track. This procedure was iterated until all overlaps were removed. The efficiency was measured per track and calculated separately for each track selection category using the measured numbers of Event Filter and offline tracks, N_{EF} and $N_{offline}$

$$\epsilon = \frac{N_{EF}}{N_{offline}}. \tag{4.2}$$

The binomial uncertainty is given by:

$$\sigma_\epsilon = \sqrt{\epsilon.\left(1-\epsilon\right)/N_{offline}}. \tag{4.3}$$

Figure 4.4 shows the efficiency to reconstruct Event Filter tracks with respect to loose offline tracks, as a function of d_0, for 100k events of the run 121416 recorded with the solenoid field on [44]. The efficiency is close to 100% in the

Track category	Cut
Loose	$\geq$8 barrel silicon hits $\lvert d_0 \rvert < 500$ mm $p_T > 1$ GeV -10 ns < TRTEventPhase < 40 ns
Medium	$\geq$10 barrel silicon hits $\geq$20 barrel TRT hits $\lvert d_0 \rvert < 250$ mm $p_T > 1$ GeV -5 ns < TRTEventPhase < 30 ns
Tight	$\geq$4 barrel pixel hits $\geq$12 barrel SCT hits $\geq$50 barrel TRT hits $\lvert d_0 \rvert < 40$ mm $p_T > 1$ GeV -5 ns < TRTEventPhase < 30 ns

Table 4.1: Classifications for offline tracks. The number of silicon hits is defined as the number of SCT layer hits plus twice the number of pixel hits. This ensures even weighting for both pixel and SCT hits, since two SCT hits are required for one three-dimensional measurement. The TRTEventPhase is the time between the read-out of the TRT detector and trigger being fired. The cut on the TRTEventPhase is designed to remove events where the TRT readout window may have missed some fraction of the hits.

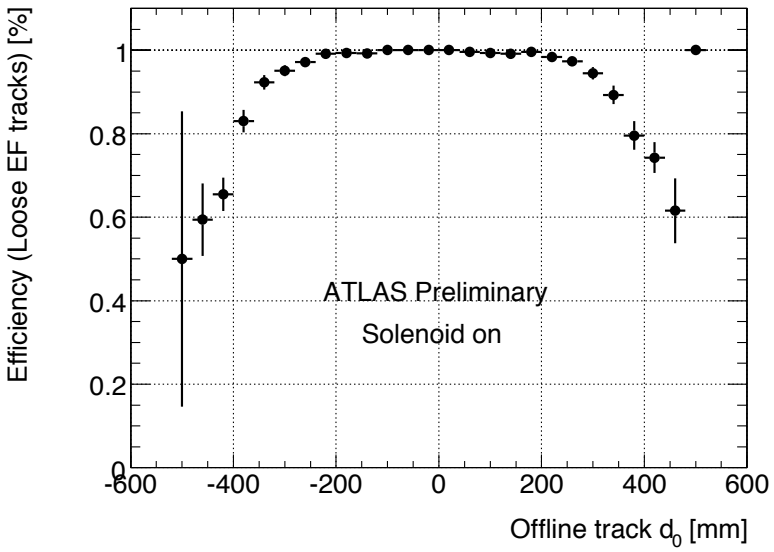

Figure 4.4: Event Filter tracking efficiency, based on 5.2k loose offline tracks. For medium and tight tracks the efficiency was found to be 100%, based on 1.7k and 120 offline tracks respectively.

central region $|d_0| < 200$ mm. Tracks at high $|d_0|$ enter the detector at very shallow angles, only leaving hits in the outer SCT layers. Although the Event Filter tracking efficiency is reduced in this region, these tracks are not representative of a typical collision track. Table 4.2 summarises the efficiencies for all track categories. Also shown for comparison are the efficiencies for three other runs from this data taking period. In runs with the solenoid field off, the cut on track p_T is not relevant, as the p_T cannot be determined from the straight-line tracks. The measured efficiencies are consistent between runs. In an ideal scenario, the same tracks would be reconstructed by both the offline and Event Filter tracking, leading to a 100% efficiency. However, since many details of the reconstruction are configurable, subtle differences between the offline and Event Filter can result in different tracks being reconstructed. These differences include cuts on the track p_T or number of silicon hits at the track seeding stage.

Run	Solenoid Status	Eff Loose [%]	Eff Medium [%]	Eff Tight [%]
121416	On	94.8 ± 0.3	100	100
121630	On	94.4 ± 0.3	99.9 ± 0.1	100
122129	Off	95.2 ± 0.2	99.9 ± 0.1	100
122189	Off	94.9 ± 0.2	99.9 ± 0.1	100

Table 4.2: The efficiency to reconstruct Event Filter tracks in each offline track category, for a selection of cosmic runs.

4.3 Studies with Early Collision Data

4.3.1 Data Set

During December 2009, ATLAS began taking data with collisions at a centre of mass energy of 900 GeV. Around 9 μb^{-1} of data was recorded at an instantaneous luminosity, L_{inst} of around 10^{26} $cm^{-2}s^{-1}$ [45]. During March 2010, the centre of mass energy was increased to 7 TeV. Data-taking began with two bunches of around 1 x 10^{10} protons and $L_{inst} \approx 10^{27}$ $cm^{-2}s^{-1}$. This study considers one 900 GeV run and one early 7 TeV run and, in each case, the data-set corresponds to every event that fired a Level-1 trigger. In both runs the pixel, SCT and TRT detectors were operational and the solenoid field was on. The trigger menu used was based on Level-1 items designed for early data-taking and contains minimum bias triggers as well as standard physics triggers such as low energy electron or jet triggers. Several Level-1 trigger items are shown in Table 4.3, along with their output rates measured in 7 TeV data. The output is dominated by the minimum bias triggers, although these triggers will be prescaled to use less of the available bandwidth as the rates of the standard physics triggers increase. The loosest minimum bias trigger, MBTS_1_1, requires at least one hit in each of the wheels, and has been shown to have an efficiency close to 100% for minimum-bias events [45]. Thus, the events considered in this tracking study correspond to minimum bias proton-proton collisions. A full physics menu is intended to be

Level-1 Trigger	Rate (Hz)
MBTS_1_1	54.31
MBTS_4_4	50.22
EM4	0.228
J10	0.058
MU6	0.009
All non-Minimum Bias	2.380

Table 4.3: The rates measured for a selection of Level-1 triggers in early 7 TeV collision data. MBTS_1_1 and MBTS_4_4 require respectively 1 and 4 hits in both MBTS wheels. For the remaining triggers, EM refers to an electron or photon object, J to a jet object and MU to a muon object. The associated numbers label the p_T cut on the object. The rates were calculated after applying cuts to remove non-collision background events: the MBTS_1_1 trigger was required to have fired and the timing between the hits on either side of the MBTS was required to be less than 10 ns.

deployed at $L_{inst} \approx 10^{30}$ cm^{-2}s^{-1}. The HLT algorithms were run in Full Scan mode for every event firing a Level-1 trigger, but not used for the trigger decision. This allowed studies to assess the performance of the Event Filter tracking.

4.3.2 Track Parameter Studies

Tracks reconstructed with the offline tracking algorithms were used as a reference to assess the performance of the Event Filter tracking algorithms. The offline track selection is based on [45] and is designed to select high quality tracks from the inside-out tracking. Offline tracks were required to have at least one pixel hit, at least six SCT hits, and to fulfil $p_T > 1$ GeV, $|d_0| < 1.5$ mm, $|\eta| < 2.5$ and $|z_0| < 200$ mm. The selected offline tracks were then matched to the Event Filter tracks using the matching algorithm described in Section 4.2.3. Only track pairs with $\Delta R < 0.1$ were considered, and this is part of the definition of the track reconstruction efficiency. However, studies of the matching showed that this cut had a negligible effect over a wide range of values of ΔR. A decrease in efficiency was observed when the ΔR cut approached the resolution of the Event Filter

tracks in η and ϕ, around $\Delta R = 0.003$. However, a cut at $\Delta R = 0.1$ is far from this region.

Figure 4.5 shows the track parameters of all Event Filter tracks that were matched to an offline track, for both 900 GeV and 7 TeV data. All distributions are normalised to the same area. The ϕ distribution is isotropic, as expected for a hermetic detector, and the distributions in η and ϕ are very similar at 900 GeV and 7 TeV. The track p_T distribution is harder for a higher collision centre of mass energy. The default value for d_0 is calculated with respect to the nominal (0,0,0) of the tracking co-ordinate system. The corrected d_0 accounts for a beamspot position that is shifted from the nominal interaction point, and reflects the true shape of the d_0 distribution. At 900 GeV the z_0 distribution is shifted to negative values, due to an offset in the z co-ordinate of the beamspot position. During 7 TeV running the transverse beam size was smaller, leading to narrowed distributions for d_0 and z_0.

Figure 4.6 shows the average number of pixel hits and SCT hits per track as a function of track η for both Event Filter and offline tracks from 7 TeV data. The increased number of hits at high η is due to hits in both barrel and endcap layers, and the η locations of the SCT endcap layers can be seen as spikes in the distribution of the number of SCT hits as a function of η.

4.3.3 Tracking Efficiency and Residual Studies

Using the efficiency definition given in Section 4.2.3, the Event Filter tracking efficiency was measured with respect to the offline tracks. In the data considered, both the offline and Event Filter tracking used a global χ^2 fitter and, since the Event Filter tracking was run in a full-scan mode, with an RoI the size of

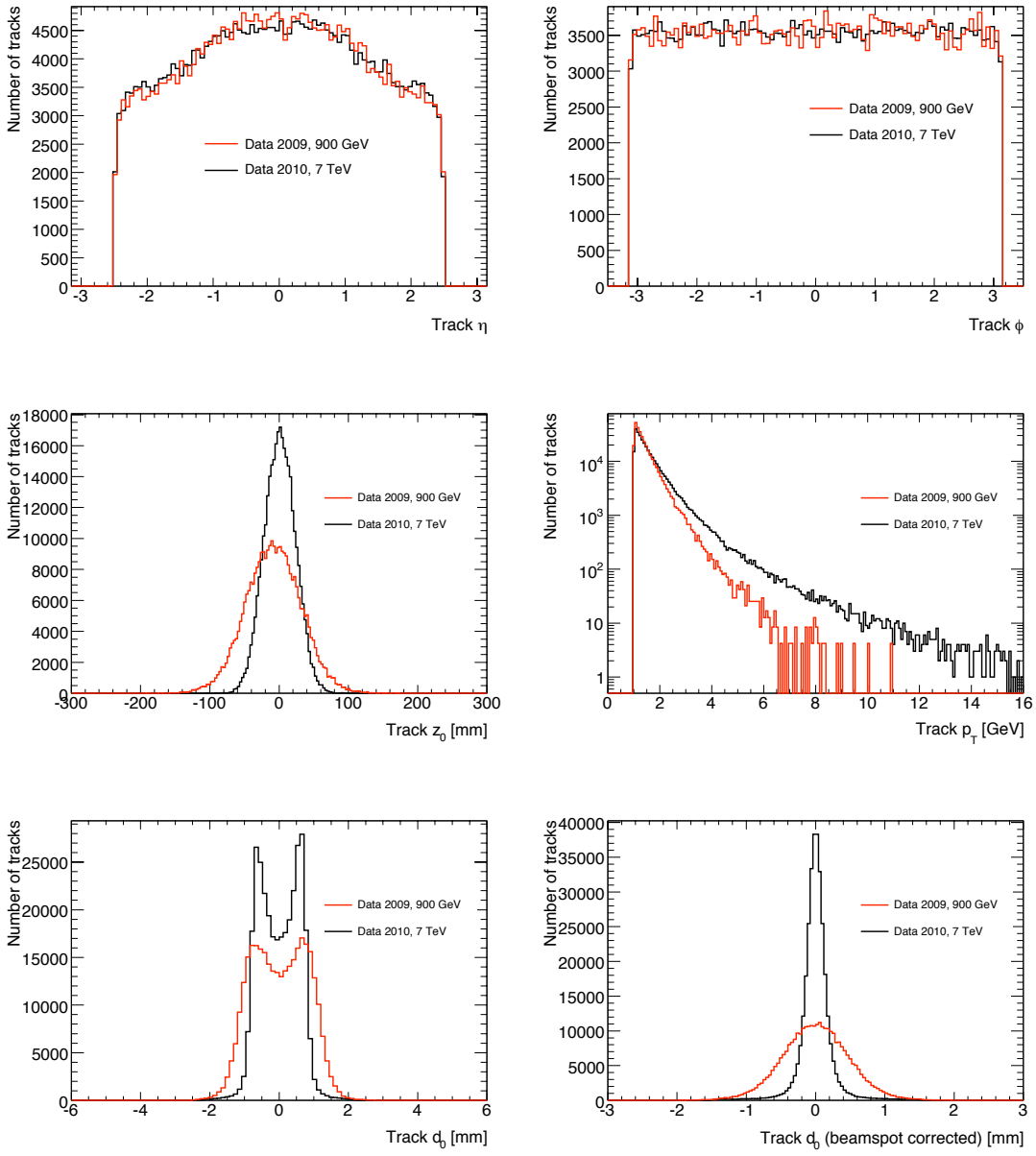

Figure 4.5: The track parameters η, ϕ, z_0, p_T, d_0 and corrected d_0 shown in red for 900 GeV data and black for 7 TeV data [46].

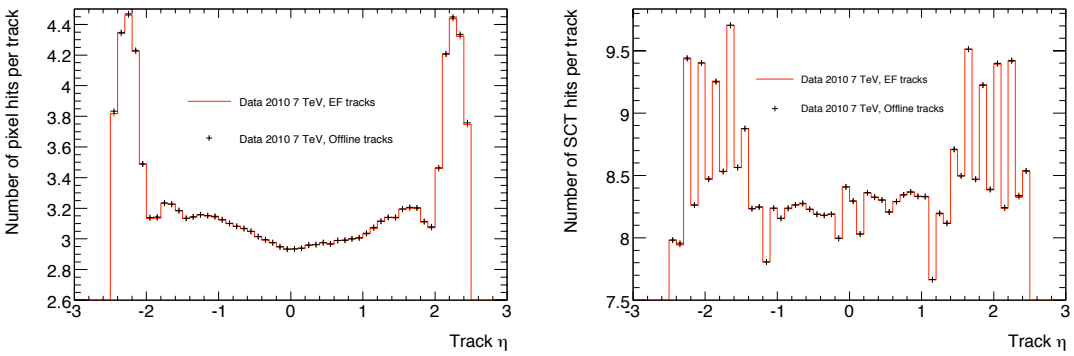

Figure 4.6: The average number of pixel and SCT hits per track for Event Filter and offline tracks [46].

the detector acceptance, the RoI-based tracking used in the Event Filter is not expected to affect the efficiency. The low luminosity during early data-taking allowed both the Event Filter and offline tracking to use track seeding without a z-vertex constraint although, as the luminosity increases, it is expected that a z-vertex constraint will be introduced in the Event Filter tracking. Both the Event Filter and offline tracking used the 'finding through fitting' vertexing method. There are, however, some differences between the offline and Event Filter tracking configurations. The offline tracking had a minimum p_T cut at 0.5 GeV at the track seeding stage, whereas in the Event Filter the minimum p_T for track seeds was 1 GeV. The offline reconstruction has access to a detailed map of the detector conditions on a run-by-run basis. In the online environment, it is not feasible to update this information so frequently, and the Event Filter tracking does not always have access to the fully accurate detector conditions.

Figures 4.7 and 4.8 show the efficiency as a function of the offline track p_T and η for 900 GeV data. A threshold effect is seen at low p_T. This is expected, due to the different cuts at the track seeding stage. The efficiency is close to 100% outside the threshold region. The corresponding plots for 7 TeV data are shown in Figures 4.9 and 4.10. The efficiency is seen to drop at high η, and this is

particularly noticeable with a p_T cut at 1 GeV.

Figure 4.11 shows the residual distributions for each track parameter for 900 GeV data. For each matched pair of Event Filter and offline tracks, the residual is defined as the difference between the Event Filter track parameter and the offline track parameter. The distributions have gaussian cores with non-gaussian tails. The quantity $\sigma_{95\%}$ is the standard deviation of the central part of the distribution containing 95% of the total number of entries. The corresponding distributions from collisions at 7 TeV are shown in Figure 4.12 and show a good improvement. This is expected, since the high-p_T tracks, which are more accurately reconstructed by the tracking software, form a larger fraction of the track sample.

Good tracking of charged particles in the Event Filter trigger will be vital in order to have the efficient, high-purity single lepton triggers needed for the charged Higgs analysis described in this thesis. The results shown in this chapter are an early performance study of the Event Filter tracking, and show that the Event Filter is performing well with respect to the full offline track reconstruction.

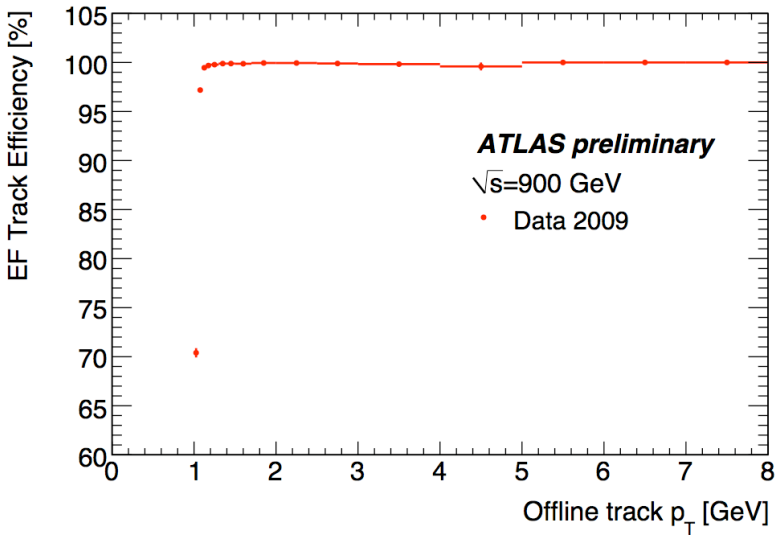

Figure 4.7: The efficiency to reconstruct Event Filter tracks, with respect to offline tracks, as a function of offline track p_T from 900 GeV data [46].

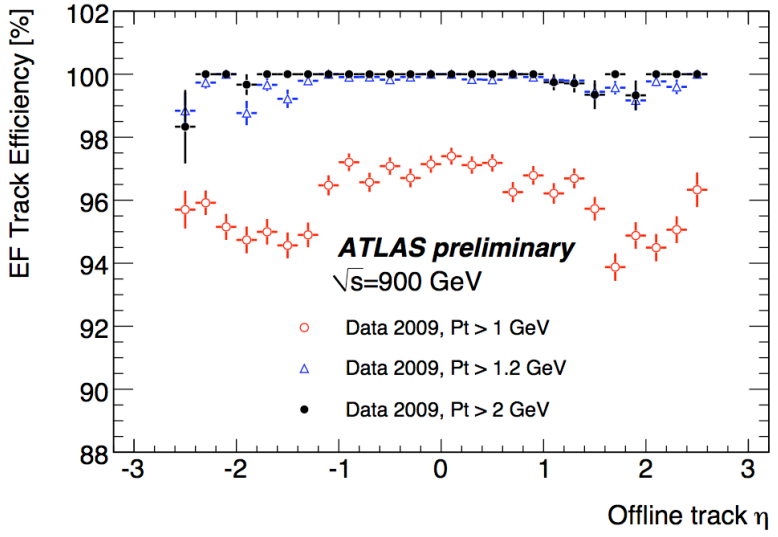

Figure 4.8: The efficiency to reconstruct Event Filter tracks, with respect to offline tracks, as a function of offline track η, for 900 GeV data [46]. Three different p_T thresholds are shown for the offline tracks.

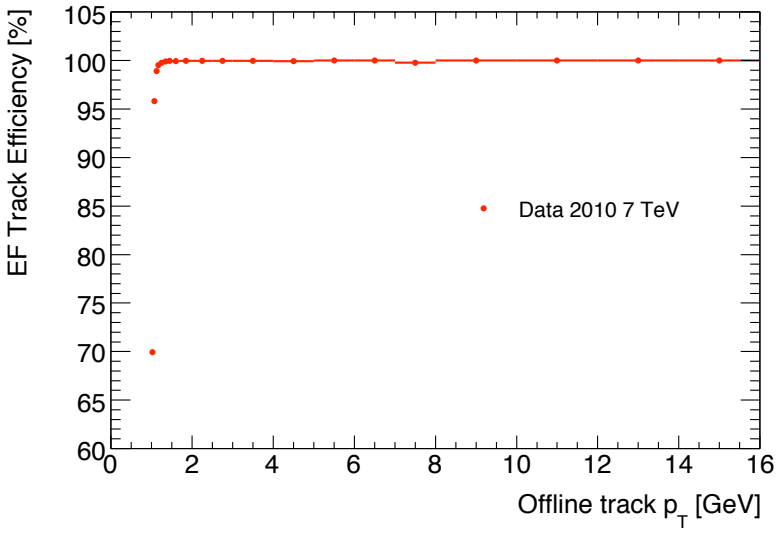

Figure 4.9: The efficiency to reconstruct Event Filter tracks, with respect to offline tracks, as a function of offline track p_T for 10 TeV data.

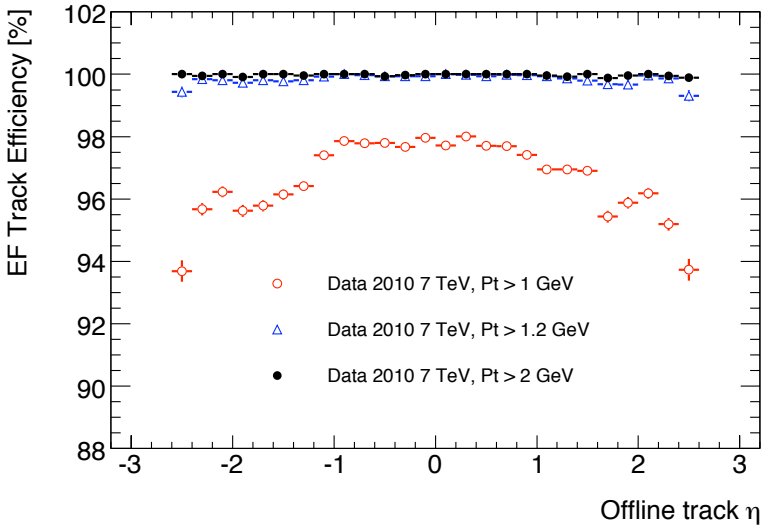

Figure 4.10: The efficiency to reconstruct Event Filter tracks, with respect to offline tracks, as a function of offline track η for 10 TeV data. Three different p_T thresholds are shown for the offline tracks.

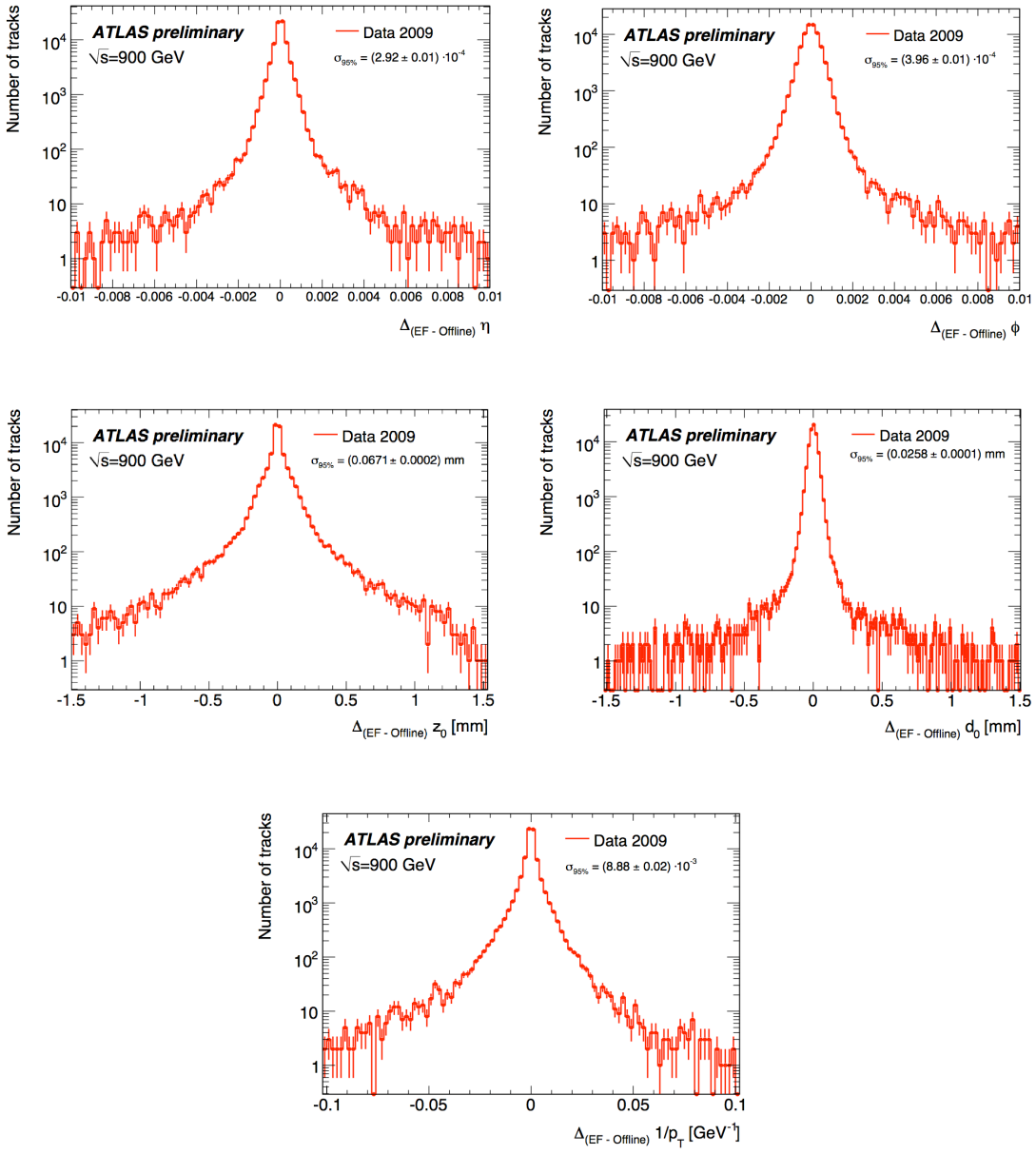

Figure 4.11: The track parameter residuals in η, ϕ, z_0, d_0 (with respect to (0,0,0)) and p_T from collisions at a centre of mass energy 900 GeV [46].

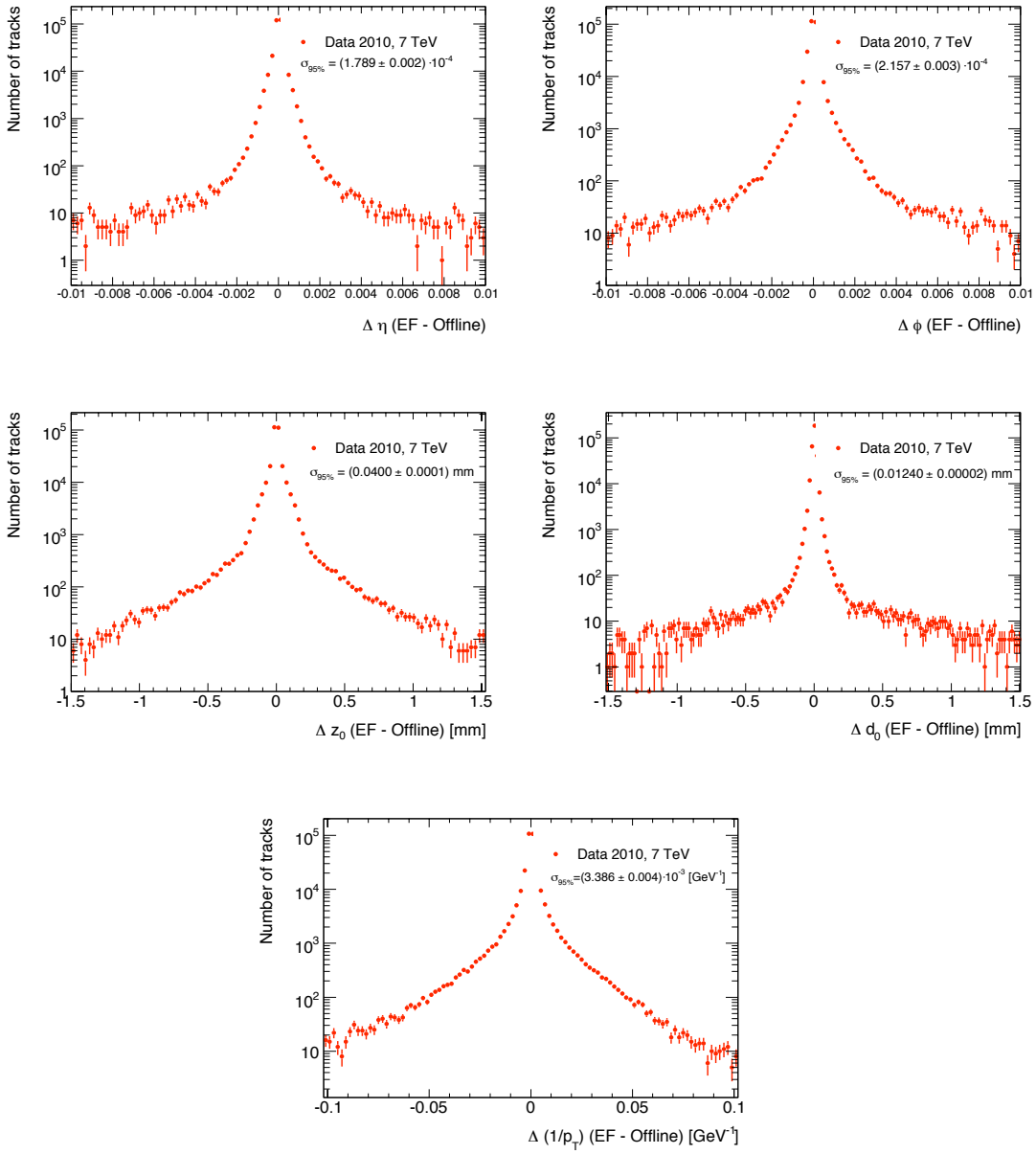

Figure 4.12: The track parameter residuals in η, ϕ, z_0, d_0 (with respect to (0,0,0)) and p_T from collisions at a centre of mass energy 7 TeV.

Chapter 5

Signal and Background Samples

This analysis considers the potential MSSM decay channel in which the hadronically decaying Standard Model W-boson in a $t\bar{t}$ decay is replaced by a charged Higgs boson, $H^{\pm}$. The $H^{\pm}$ subsequently decays to a charge conserving pair of charm and strange quarks ($H^{+} \rightarrow c\overline{s}$ or $H^{-} \rightarrow s\overline{c}$). This chapter describes the generation of Monte Carlo events in the charged Higgs signal channel, and in the relevant background channels.

5.1 Overview

The Monte Carlo events used in this analysis are part of an official ATLAS production effort, known as MC08. All samples were generated assuming collisions with a centre of mass energy of 10 TeV, and different Monte Carlo generators were used for different channels, depending on the strengths of each generator. In channels containing a top quark, the top quark mass was assumed to be 172.5 GeV. The PDF set CTEQ6M was used, and the generated events were subject to the full

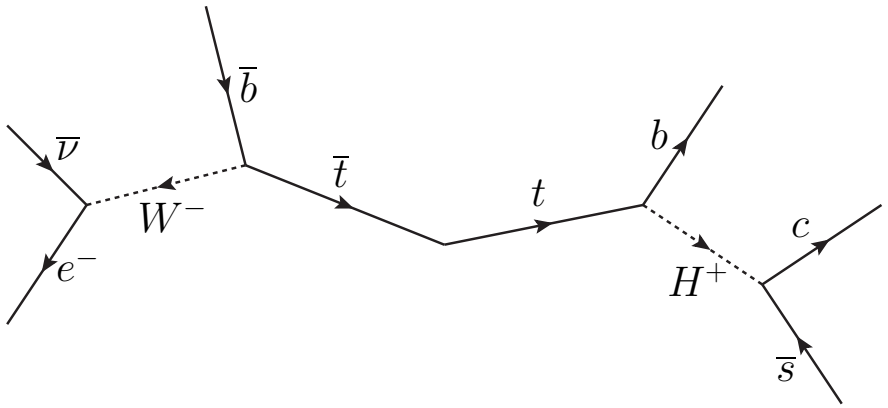

Figure 5.1: The leading order diagram for the production of a light H^+ boson in a semi-leptonic $t\overline{t}$ decay.

ATLAS detector simulation and event reconstruction. At the high instantaneous luminosities accessible by the LHC, analyses may be detrimentally affected by multiple proton-proton collisions within a single bunch crossing. This is known as pile-up, and is not modelled in the Monte Carlo events described in this chapter. A study of the effect of pile-up on this analysis is, however, described in Chapter 8.

5.2 Charged Higgs Signal

The charged Higgs signal channel is shown in Figure 5.1 and is identical to the SM decay of a $t\overline{t}$ pair in the semi-leptonic channel, with the exception of the mass and spin of the intermediate boson produced in the hadronic top quark decay. By reconstructing the invariant mass of the di-jet system from the charged Higgs or W-boson, the presence of charged Higgs-mediated events may be inferred. In the following, the signal channel is described using the case where a positively charged Higgs boson, H^+, is produced. However, the charge conjugate decay mediated by a negatively charged Higgs boson, H^-, is also a valid decay mode and was produced and analysed at the same time.

The leading order Monte Carlo generator Pythia [47] was used to generate events in the signal channel for four charged Higgs mass points: 90, 110, 130 and 150 GeV. In the generation, charged Higgs bosons were produced by forcing top quark to decay as $t \rightarrow bH^+$, and the antitop quark to decay as $\overline{t} \rightarrow \overline{b}W^-$. The charged Higgs was forced to decay to $c\overline{s}$ or $s\overline{c}$. The signal events were generated in two separate groups, corresponding to the decay mode of the W-boson. In the first group, the W-boson decayed to either an electron or a muon, and in the second group it decayed to a tau. The tau was forced to decay leptonically, with the decay modelled by Tauola [48]. The channel where the tau decays hadronically was not considered. The details of the signal samples are shown in Table 5.1.

It is possible to perform this analysis for charged Higgs mass points below 90 GeV. However, charged Higgs masses far below the W-boson mass have already been excluded [9], and it has been shown at the Tevatron [26] that the sensitivity for a charged Higgs analysis of this type is greatly reduced when the H^+ and W-boson masses are degenerate. This argument will be further motivated in Chapter 7. A further source of charged Higgs events from $t\overline{t}$ decays is from the potential decay mode $t\overline{t} \rightarrow b\overline{b}H^+H^-$. However, given the current Tevatron limits on the branching ratio $t \rightarrow bH^+$, the contribution of this channel would be at least an order of magnitude smaller than for the signal channel shown in Figure 5.1. In this analysis, the decay mode $t\overline{t} \rightarrow b\overline{b}H^+H^-$ was therefore considered to be negligible.

m_{H^+} (GeV)	$\mathcal{B}(t \to bH^+)$	Dataset ID	$\mathcal{B} \times \sigma$ (pb)	N_{events}	L_{int} (pb^{-1})
Semileptonic $t\bar{t} \to b\bar{b}H^+W^-(H^+ \to c\bar{s},\ W \to e, \mu + \nu)$					
90	22%	109421	29.4	25000	850
110	14%	109422	20.6	25000	1213
130	8%	109420	12.6	25000	1984
150	12%	109423	18.1	25000	1381
Semileptonic $t\bar{t} \to b\bar{b}H^+W^-(H^+ \to c\bar{s},\ W \to \tau + \nu)$					
90	22%	109784	15.5	9720	627
110	14%	109785	10.9	9930	911
130	8%	109786	6.7	9650	1440
150	12%	109787	9.5	9840	1036

Table 5.1: The simulated signal samples $t\bar{t} \to b\bar{b}H^+W^-$. The second column shows the Tevatron upper limits on $\mathcal{B}(t \to bH^+)$, and the column labelled $\mathcal{B} \times \sigma$ shows the cross-section to produce events in the signal channel, assuming the NLO cross-section for top quark pair production, $\sigma_{t\bar{t}} = 401.6$ pb [24], and a branching ratio $\mathcal{B}(t \to bH^+)$ at the Tevatron limit for each mass point. Also assumed are the branching ratios $\mathcal{B}(\tau \to l + \nu\text{s}) = 0.352$, $\mathcal{B}(W \to e, \mu + \nu) = 0.213$ and $\mathcal{B}(W \to \tau + \nu) = 0.113$.

5.3 Standard Model $t\bar{t}$ Background

Standard model $t\bar{t}$ events were generated using the next to leading order Monte Carlo generator MC@NLO [49]. MC@NLO considers all possible next to leading order diagrams for the stage $pp \to t\bar{t}$. The top-quark pair then decays as $t\bar{t} \to W^+W^-b\bar{b}$ according to the leading order diagram. Higher order effects due to the real and virtual emission diagrams at the $pp \to t\bar{t}$ stage lead to a small fraction of events having a negative weight. Observable quantities are described by the weighted sum of events, so the event weight must be accounted for in the analysis. The parton showering and hadronisation were modelled by HERWIG [50]. The underlying event, consisting of the proton remnants, was modelled using Jimmy [51] (for multiple parton interactions) and by Herwig (for the remaining underlying event processes).

Only the fully-leptonic and semi-leptonic decay channels were generated, by forcing one W-boson to decay to an electron, muon or tau, and allowing the remaining W-boson to decay freely. The details of the generated events are shown in Table 5.2 and are listed as $t\bar{t}$ not fully hadronic (MC@NLO) .

Process	Dataset ID	$\mathcal{B} \times \sigma$ (pb)	N_{events}	L_{int} (pb^{-1})
$t\bar{t}$ not fully-hadronic (MC@NLO)	105200	218.4	166496	913.4
Single top s-channel ($e\nu_e$)	108343	0.76	2858	3761
Single top s-channel ($\mu\nu_\mu$)	108344	0.76	8065	10612
Single top t-channel	105502	43.2	25053	580.0
Single top Wt-channel	105500	14.3	9999	699.2

Table 5.2: Monte Carlo samples for Standard Model background processes with top quarks in the final state, together with their cross-sections and the number of events. The $t\bar{t}$ events in the not fully-hadronic channel are $t\bar{t}$ pairs decaying in the di-lepton or semi-leptonic modes, and the NLO cross-section is taken from [24]. The quoted cross-sections for single top events have been scaled with the appropriate k-factor to account for NLO corrections.

5.4 Single Top Background

At leading order, single top quarks can be produced by three different mechanisms, which are shown in Figure 5.2. At the Tevatron, the dominant production mechanisms are the s-channel and t-channel diagrams. However, at the LHC the s-channel contribution is very small as a result of the increased collision energy, and the Wt-channel becomes of greater interest. [52]. The Wt-channel most closely resembles the charged Higgs signal channel, as a result of the two W-bosons that are produced in each event.

The Monte Carlo generator AcerMC [53] was used to generate single top events in the t-channel and the Wt-channel. The details and relevant cross-sections are given in Table 5.2. In the t-channel, the top quark was forced to

decay leptonically. The hadronic decay of the single top was considered to be a negligible background. The Wt-channel diagram contains two W-bosons, whose decay modes can be used to characterise the event in the same way as for a $t\bar{t}$ decay. Only the di-lepton and semi-leptonic decay channels were produced for the Wt channel, with the fully-hadronic channel assumed to be negligible. The cross-sections given in Table 5.2 reflect these generator level cuts. For the s-channel diagram, events were generated using MC@NLO, and the resulting top quark was forced to decay leptonically. Separate samples were generated for s-channel events with an electron or a muon in the final state. Samples with a tau in the final state were not available. For all single top events, the parton shower was modelled using HERWIG and the underlying event was modelled by Jimmy.

Since we search for a charged Higgs in the decay of a top quark, single top events can provide additional charged Higgs events, but they are not considered in this study. This is, in part, because single top events are produced with a much smaller cross-section than $t\bar{t}$ events. Additionally, if the single top quark is forced to decay to a charged Higgs boson that subsequently decays hadronically, only the Wt-channel can mimic the final state of the signal without requiring the misidentification of a jet as a lepton. For this reason, single top events are considered only as a background. However, this choice is motivated further in Section 6.3, where the effect of event selection cuts on the single top background is described.

5.5 W + Jets Background

A leptonically decaying W-boson produced in association with additional jets from initial state radiation, as shown in Figure 5.3, can lead to the same final

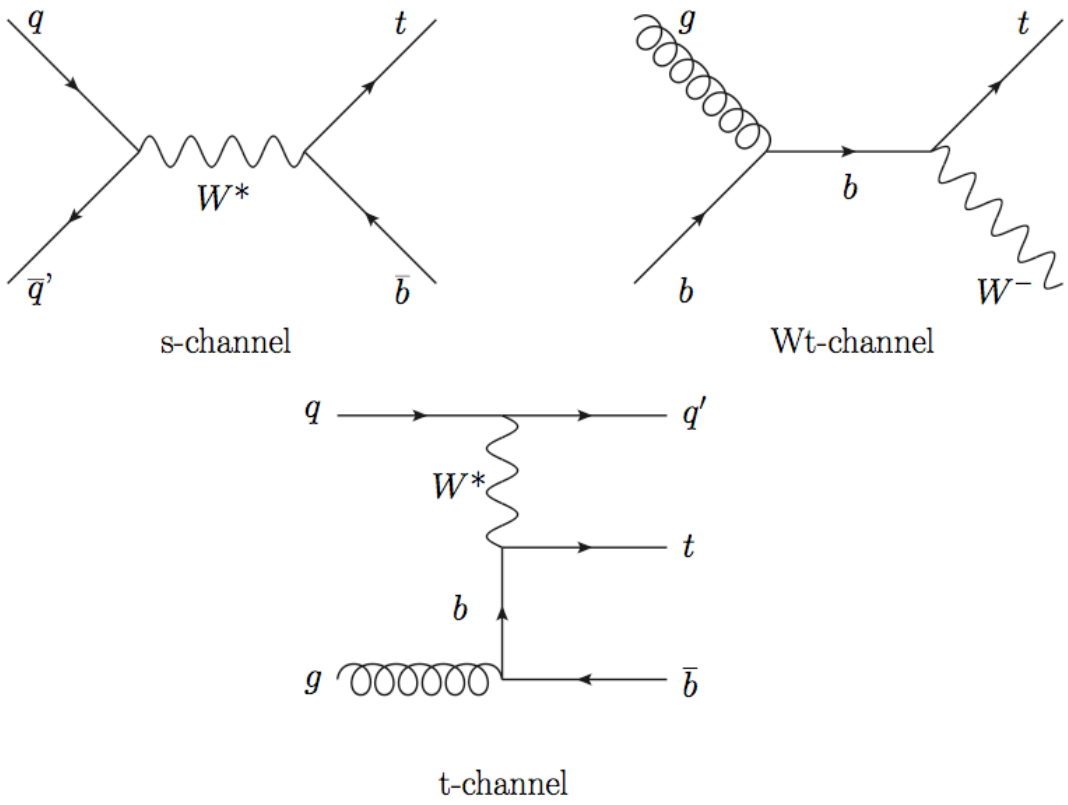

Figure 5.2: The three main production mechanisms for single top quarks at the LHC. Both the t-channel and s-channel diagrams proceed via a virtual W-boson. The Wt channel, in contrast, requires the production of both a real top and a real W-boson.

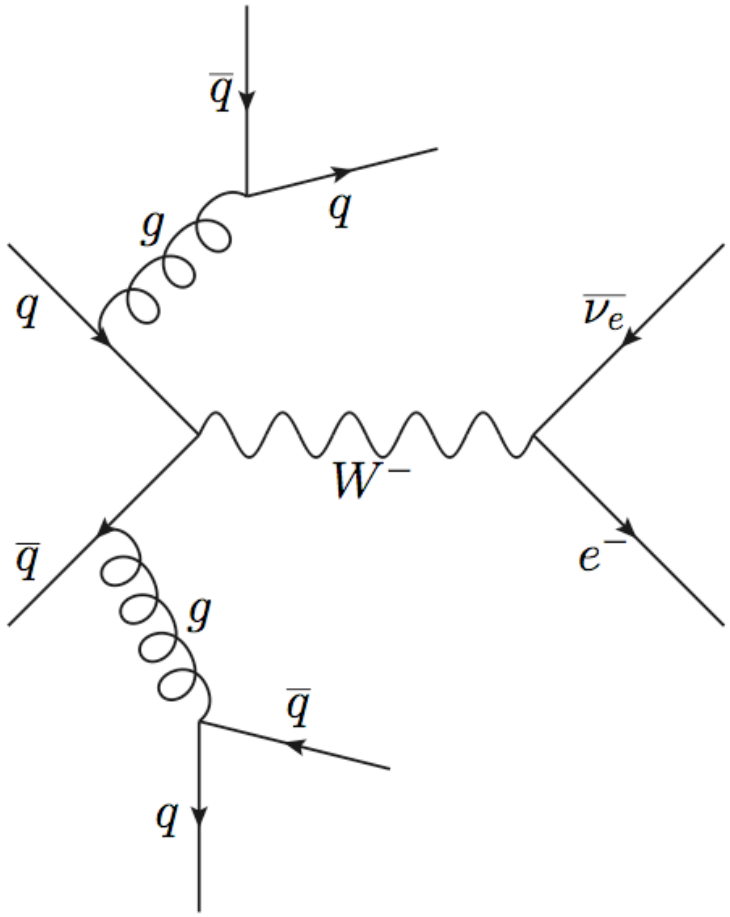

Figure 5.3: Jets produced in association with a W-boson can provide a high p_T lepton, large E_T^{miss} and several high p_T jets, closely resembling a semi-leptonic $t\bar{t}$ decay.

state as the charged Higgs signal channel. Measurements at the Tevatron have previously found this process to be a non-negligible background in top quark-related studies. The probability for four additional jets to be produced in a given event is low, but the large cross-section for W-boson production means that this is an important background to study at the LHC.

W + jets events were produced using the ALPGEN [54] Monte Carlo generator, which is specifically designed to generate multi-parton events in hadron-hadron collisions, and is the default generator used by ATLAS to model decay

channels with a large number of jets in the final state. ALPGEN is a leading order generator and, depending on the process, can provide the matrix element for up to six additional hard partons in an event. For a given process, an (N+1)-jet final state can result from two different mechanisms: either by the soft radiation evolution of an (N+1)-parton final state, or by the radiation of a hard, large angle parton from an N-parton final state. This presents a technical problem in the simulation of events with additional jets and can lead to double-counting effects. The MLM [55] matching scheme was used to remove overlaps and can be summarised as follows:

- The cross-sections are calculated separately for the processes pp $\rightarrow$ X + n jets, where X is the process of interest and n = 0,1,...n_{max}.
- Parton-level events are generated in numbers proportional to their respective cross-sections, and with a minimum transverse energy threshold, E_T^{min} for each parton, and minimum separation in ΔR of R_{min} between the partons.
- Parton showering is performed with no veto on hard emissions in the event.
- A cone algorithm is applied to the event, with a cone size R_{min} and a minimum transverse energy cut at E_T^{min}, and defines the jets present in the event after parton showering.
- Beginning with the hardest parton, partons and jets are matched if their separation in $\eta - \phi$ space is less than R_{min}.
- Events are rejected if not all jets have a matching parton.
- In the sample with the highest multiplicity of additional jets (nmax), events with an additional hard parton from the parton shower are not rejected, giving an inclusive sample.

The W + jets events used in this analysis are shown in Table 5.3 and are described fully in [56]. The W + light flavour samples include all processes with u,d,s or c-quarks in the matrix element calculation. Separate samples were generated for events containing b-quarks, and are listed as $Wb\bar{b}$ + N partons. The MLM matching parameters used were $E_T^{min} = 20$ GeV and $R_{min} = 0.7$. Overlaps can occur between the light and heavy flavour samples, since a b-quark can originate from the matrix element calculation in the $Wb\bar{b}$ + N partons sample, or from parton showering of the W + light flavour events. These overlaps are generally suppressed by the MLM matching in an exclusive W + light jets sample. However, in the inclusive (nmax) sample, the effect is larger. For the samples listed in Table 5.3, phase space cuts on the $Wb\bar{b}$ + N partons samples were used to minimise the effects of these overlaps.

5.6 QCD Background

QCD multi-jet processes do not have the same features as the charged Higgs signal. However, due to their large cross-sections and a non-negligible lepton mis-identification rate, they may contribute background events. The size of this background is difficult to predict using Monte Carlo techniques due to the large statistics required. The lepton mis-identification rate is also difficult to model, and depends strongly on the real performance of the detector and reconstruction algorithms. For these reasons, the QCD background is not included in this analysis. It is expected that, once the QCD processes are well understood in data, appropriate cuts can be optimised to remove the majority of these events. In addition, the charged Higgs search performed in this thesis is a shape analysis. Since the kinematics of the final state objects in QCD events are unlikely to reflect those of top-pair events, any surviving QCD background events are expected to

Process	Dataset ID	$\mathcal{B} \times \sigma$ (pb)	N_{events}	L_{int} (pb^{-1})
$W \rightarrow e\nu$ + 0 parton	107680	12425.3	149429	12.0
$W \rightarrow e\nu$ + 1 parton	107681	2577.1	30233	11.7
$W \rightarrow e\nu$ + 2 partons	107682	824.7	218420	264.8
$W \rightarrow e\nu$ + 3 partons	107683	248.0	44811	180.7
$W \rightarrow e\nu$ + 4 partons	107684	68.4	11969	175.0
$W \rightarrow e\nu$ + $\geq$ 5 partons	107685	20.2	3500	173.3
$W \rightarrow \mu\nu$ + 0 parton	107690	12353.3	145983	11.8
$W \rightarrow \mu\nu$ + 1 parton	107691	2629.7	29731	11.3
$W \rightarrow \mu\nu$ + 2 partons	107692	844.6	467164	553.1
$W \rightarrow \mu\nu$ + 3 partons	107693	246.4	42743	173.5
$W \rightarrow \mu\nu$ + 4 partons	107694	67.7	11900	175.8
$W \rightarrow \mu\nu$ + $\geq$ 5 partons	107695	19.9	3500	175.8
$W \rightarrow \tau\nu$ + 0 parton	107700	12417.5	1152353	92.8
$W \rightarrow \tau\nu$ + 1 parton	107701	2570.4	35224	13.7
$W \rightarrow \tau\nu$ + 2 partons	107702	820.8	107106	130.5
$W \rightarrow \tau\nu$ + 3 partons	107703	247.3	43622	176.4
$W \rightarrow \tau\nu$ + 4 partons	107704	67.5	12000	177.8
$W \rightarrow \tau\nu$ + $\geq$ 5 partons	107705	20.7	3500	169.1
$Wb\bar{b}$ + 0 parton	106280	6.3	15500	2475
$Wb\bar{b}$ + 1 parton	106281	6.1	15457	2534
$Wb\bar{b}$ + 2 partons	106282	3.5	8953	2558
$Wb\bar{b}$ + $\geq$ 3 partons	106283	2.0	5000	2500

Table 5.3: The background channels due to the the production of a W-boson in association with light or heavy flavour jets. Each quoted cross-section has been scaled with the appropriate k-factor to account for NLO corrections.

contribute a flat background shape, thereby having little effect on the final result.

This argument is motivated further in Chapter 7.

Chapter 6

Event Selection

The charged Higgs signal channel is characterised by a high-p_T lepton, a large missing transverse energy, E_T^{miss} and four quarks, plus additional radiation from the initial and final states. These features must be accurately reconstructed and utilised to select potential signal events, whilst efficiently rejecting the background. This section gives an overview of the techniques used by ATLAS to reconstruct the final state physics objects from the detector information. The event selection strategy is discussed, and the effect of the event selection cuts on the signal and background channels is described quantitatively for data-taking scenarios at both $\sqrt{s} = 10$ TeV and $\sqrt{s} = 7$ TeV. This analysis has been described in [57, 58] and the selection cuts are based on those used by the ATLAS Top Working Group in a Monte Carlo study of the $t\bar{t}$ cross-section measurement in the semileptonic channel at $\sqrt{s} = 10$ TeV [59].

6.1 Object Reconstruction

The ATLAS offline reconstruction software is designed to interpret the information provided by the detector as physics objects such as electrons, muons, taus, photons and jets. Jets are described in detail in Section 6.1.4, but are the physical manifestation of quarks and gluons in the detector. The reconstruction provides information on the multiplicity of these objects along with measured quantities such as their p_T, η, ϕ and, in some cases, information about the quality of the object. The following sections describe each part of the reconstruction chain that is relevant to this analysis.

6.1.1 Triggers

During early data-taking, the luminosity provided for ATLAS is not expected to exceed 10^{32} cm^{-2}s^{-1}, and it is expected that low-p_T single lepton triggers may be used un-prescaled. At higher luminosities, these triggers will be tightened either by a higher p_T threshold or higher quality cut on the lepton. For this analysis, single lepton triggers were used with a p_T threshold of 15 GeV. The trigger chains used were EF_mu15 and EF_e15_medium; these correspond to either an electron or a muon reconstructed in the Event Filter with $p_T > 15$ GeV. In the case of the electron chain, the suffix 'medium' defines the quality of the reconstructed electron and is described in Section 6.1.2.

6.1.2 Electrons

Electrons are charged particles subject to electromagnetic interactions. As such, they leave hits in the Inner Detector and, typically, deposit all of their energy in

the ECAL. The ATLAS electron reconstruction software [31] is optimised to efficiently reconstruct electrons with $p_T > 20$ GeV and $|\eta| < 2.5$ using information from the Inner Detector and the calorimeter systems. Electron reconstruction begins with a seed cluster of energy deposits in neighbouring cells of the second layer of the ECAL. The energy deposit is measured in a window of fixed size around the cluster, and the measured energy is corrected for effects such as variations as a function of η and ϕ, for energy loss in the presampler, and for longitudinal leakage. The Inner Detector hits are used to reconstruct tracks, as described in Section 4.1, and these tracks are extrapolated to the ECAL. For each cluster, the closest matching track in ΔR is associated with the cluster to form an electron candidate. Monte Carlo studies have shown [31] that for electrons at $|\eta| = 0.3$, the expected energy resolution is 1.2% for a 100 GeV electron, rising to 2.5% for a 20 GeV electron.

Hadronic activity can also lead to Inner Detector tracks and energy deposits in the calorimeter. Quality cuts are used to reject this hadronic background. Three levels of cuts, 'loose', 'medium' and 'tight', have been defined in [60], and are described briefly below.

- Loose: The loose cuts are the basic selection criteria, defined to give a high electron reconstruction efficiency, but without optimised background rejection. Information from the second layer of the ECAL is considered, and the longitudinal shower containment and shower shape are used for a coarse rejection of the hadronic background.

- Medium: The medium cuts reject much of the hadronic background. Track quality cuts are applied, rejecting electron candidates whose associated track has a low number of pixel or SCT hits, or a large transverse impact parameter. A cut on the matching parameter ΔR between track and

cluster, and information on the shower shape in the first ECAL layer are also used.

- Tight: The tight selection places additional cuts on the number of pixel b-layer hits, TRT hits, and TRT high-threshold hits on the track. The impact parameter cut is tightened, and a cut is made on the ratio of the cluster energy to the track momentum, E/p.

In this analysis, medium electrons were used,which are inclusive of the electrons passing the tight selection cuts. Figure 6.1 shows the p_T, η, ϕ and number of medium electrons reconstructed in Standard Model $t\bar{t}$ events and non-$t\bar{t}$ events. The non-$t\bar{t}$ background channels considered are listed in Tables 5.2 and 5.3 and have been normalised according to these cross-sections. In these plots, the distributions from $t\bar{t}$ events are derived from Standard Model $t\bar{t}$ Monte Carlo events. However, the distributions should be considered as a reflection of both the charged Higgs signal events and the Standard Model $t\bar{t}$ background events, due to the similarities between the two channels. This argument is further motivated in Section 6.2. Electrons reconstructed in $t\bar{t}$ events typically have higher p_T and are more central than in the non-$t\bar{t}$ background events.

In this analysis, electrons were required to have $p_T > 20$ GeV and $|\eta| < 2.5$, and were vetoed in the region $1.37 < |\eta| < 1.52$, which corresponds to a region of decreased instrumentation in the ECAL. The loose, medium and tight selections do not include cuts on the electron isolation. An additional cut was applied to reject electrons with more than 6 GeV of additional energy deposited in a cone of $\Delta R = 0.2$ around the electron. This cut will be important for the rejection of QCD background, and will be optimised once the QCD background is understood from data.

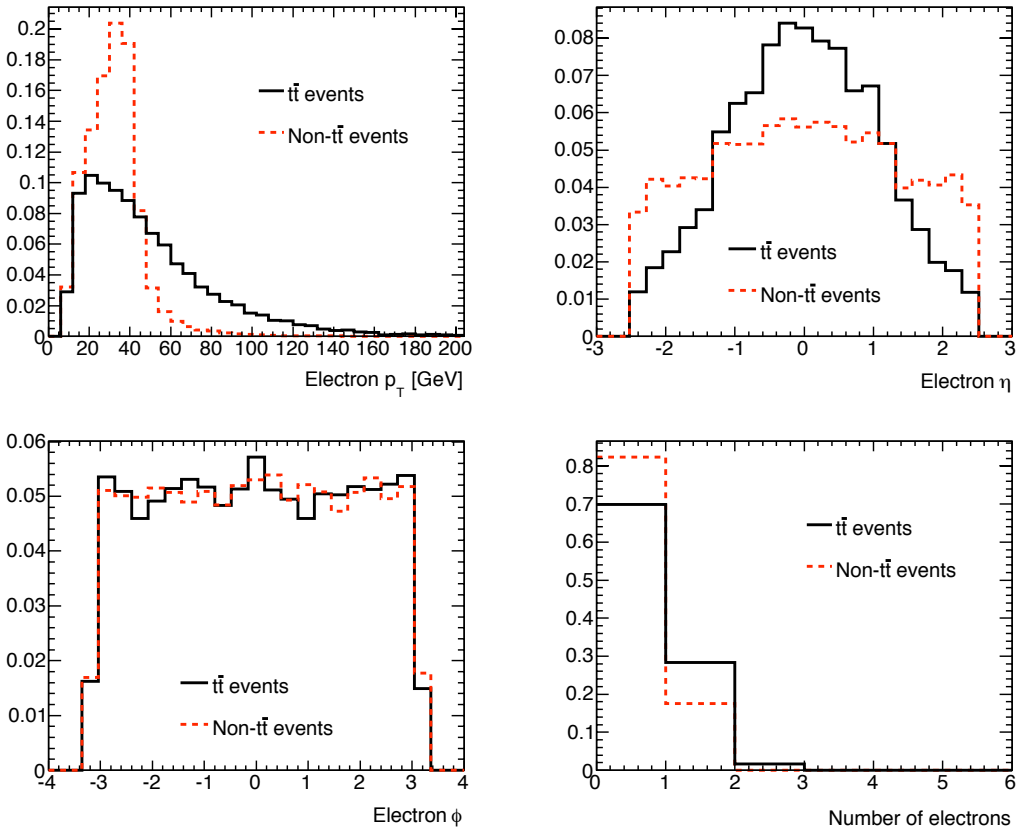

Figure 6.1: The p_T, η, ϕ and number of medium electrons reconstructed in Standard Model $t\bar{t}$ events and non-$t\bar{t}$ background events, as described in Tables 5.2 and 5.3. All distributions have been normalised to unit area.

6.1.3 Muons

A muon will typically leave a track in both the Inner Detector and the outer Muon Spectrometer, with very little energy deposited in the calorimeters. Tracks are reconstructed in the muon spectrometer with $|\eta| < 2.7$ but, particularly for low p_T tracks, multiple scattering effects can lead to poor resolution on the measured p_T. There may also be large numbers of fake tracks, which do not correspond to real muons. This analysis uses muons reconstructed by the STACO algorithm [61], which improves the stand-alone measurement made by the Muon

Spectrometer. Each track is corrected to account for the energy loss of the candidate muon in the calorimeters, and is projected backwards towards the interaction point. A matching algorithm rejects any muon candidate without a matching Inner Detector track, and the matched Inner Detector and Muon Spectrometer tracks are combined. The energy correction is a function of the track p_T and η, and reflects the non-gaussian energy loss of a muon traversing the beampipe, Inner Detector and calorimeters before reaching the muon spectrometer. However, if the measured energy loss in the calorimeters is much larger than that predicted by the correction, the measured value can be used to correct the muon energy.

The STACO muon reconstruction is limited to $|\eta| < 2.5$ by the coverage of the Inner Detector. In general, the resolution on the measured muon p_T depends on both p_T and η. At high p_T the straighter tracks are more easily reconstructed but the small sagitta limits the resolution, whilst multiple scattering can affect very low p_T muons. The resolution is also affected by inhomogeneities in the magnetic field strength, particularly in the region between the barrel and endcap toroids. For a 100 GeV muon in the central region of the detector, the p_T resolution is around 3% [31], increasing to around 6% for a 400 GeV muon.

Figure 6.2 shows the p_T, η, ϕ and number of STACO muons reconstructed in Standard Model $t\bar{t}$ events and non-$t\bar{t}$ background events. The muon p_T distribution from $t\bar{t}$ events is peaked at lower p_T than for the equivalent electron distribution. This is due to the presence of charged mesons, such as $\pi^{\pm}$ and b-mesons in the hadronisation of quarks and gluons, whose decay rate to muons is much larger than to electrons. Muons in $t\bar{t}$ events are also produced more centrally than in the non-$t\bar{t}$ background events. For this analysis, muons were required to have $p_T > 20$ GeV, $|\eta| < 2.5$ and less than 6 GeV of energy deposited inside a cone of radius $\Delta R = 0.2$ around the muon.

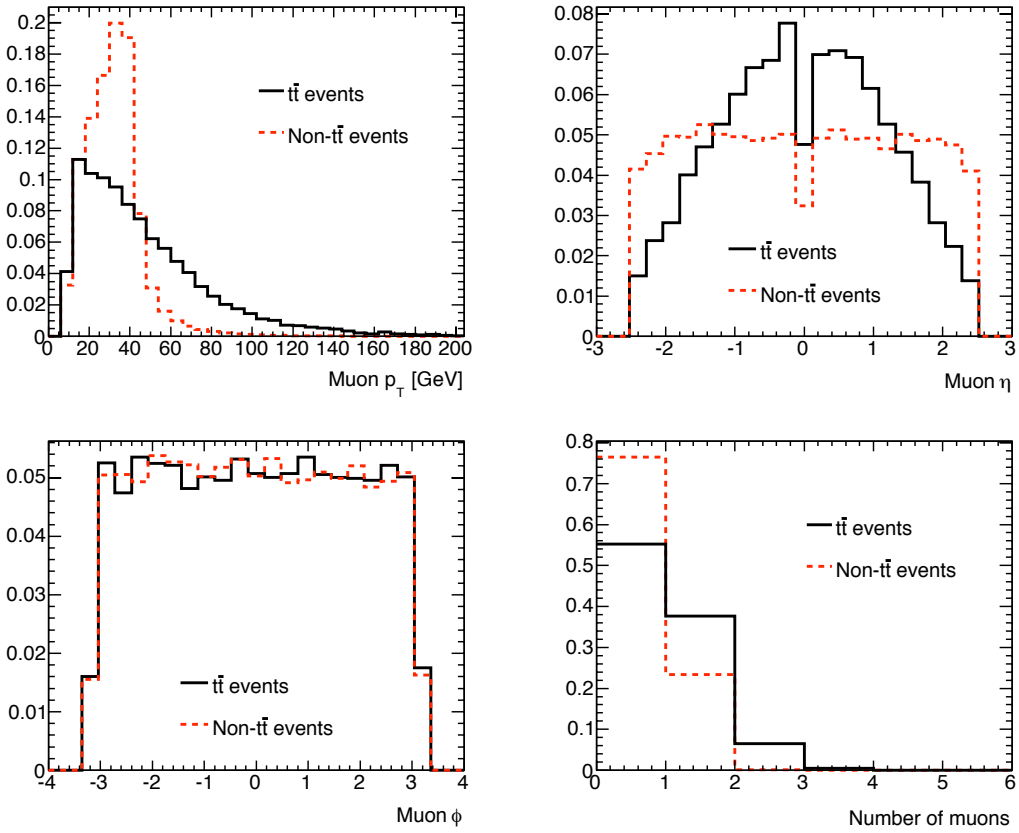

Figure 6.2: The p_T, η, ϕ and number of STACO muons reconstructed in Standard Model $t\bar{t}$ events and non-$t\bar{t}$ background events. All distributions have been normalised to unit area.

6.1.4 Jets

The charged Higgs signal channel contains four quarks plus, in many events, additional quarks and gluons resulting from initial and final state radiation. These partons fragment on the timescale of the strong interaction, forming showers of particles that can be measured in the detector. The particle showers can be grouped together to form jets, whose properties are related to those of the original parton. In general, jet reconstruction begins with a jet-finding algorithm, which clusters together particles that are likely to have originated from the same parton.

This is followed by a calibration step, where the energy of the jet is corrected to account for detector effects. The definition of a jet can vary, depending on the reconstruction method used. Cone-jet algorithms use a geometrical definition of a jet, while clustering algorithms combine nearby calorimeter cells if they satisfy some criteria based on the cell energy and the distance from the jet centre.

At a hadron collider the momentum fractions of the colliding partons are not known, and the system may be boosted. Jet-finding must, therefore, be based on quantities that are invariant under a longitudinal boost in order to treat all events equally. This analysis uses a seeded cone-jet algorithm [62], based on the parameters η, ϕ and E_T. By definition, the transverse quantities ϕ and E_T satisfy the invariance requirement. η is not invariant, however the difference in η between two detector objects is invariant under a longitudinal boost. Towers are formed from the calorimeter cells by collecting cells in a three-dimensional region, typically with size 0.1×0.1 in η and ϕ. Cells with negative energy, due to noise effects, within a tower are removed by recombination with nearby positive energy cells. Jets are then seeded by towers containing transverse energy $E_T > 1$ GeV. Beginning with the highest energy tower, a cone of radius $\Delta R = 0.4$ is drawn around the seed. The calorimeter cells contained within this cone are used to calculate the E_T weighted centre of the cells, and the cone is re-drawn at this central value. The process is iterated until a stable jet-cone is found, and is repeated for each seed. This seeding method can lead to overlaps between jets. If two jets overlap by more than a given overlap fraction, the jet with the lower E_T is discarded, and its constituent particles can be associated with the remaining jet. Cone-jets are not infra-red safe, meaning that the results of the jet finding are sensitive to soft radiation, in particular at the midpoint between two jet seeds. However, infra-red safety is mainly important in QCD studies, where the number of jets found experimentally is compared to theoretical predictions. It is expected

to have a negligible effect on this analysis.

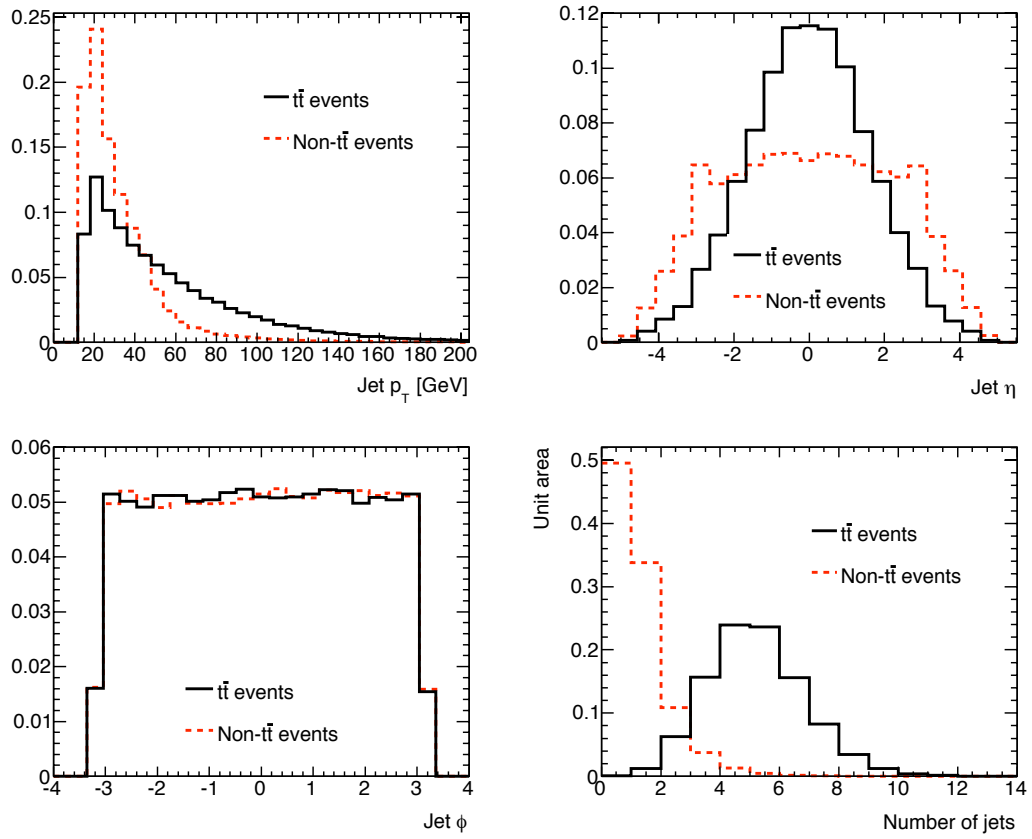

Figure 6.3: The p_T, η, ϕ and number of jets reconstructed in Standard Model $t\bar{t}$ events and non-$t\bar{t}$ background events. All distributions are normalised to unit area. Since no event selection cuts other than a lepton isolation cut have been applied, the distribution from Standard Model $t\bar{t}$ events includes events decaying in both the semi-leptonic and di-lepton channels. All distributions have been normalised to unit area.

The jet energy calibration [31] corrects the measured jet energy for effects including non-linearities in the calorimeter response as a function of particle p_T and η, poorly instrumented regions of the detector, parton showering effects, and the underlying event. Typically, an offset correction is derived from minimum-bias data, in order to correct for additional energy present in jets due to the underlying event. The jet energies are then corrected for their dependence on η, using

di-jet events where one jet is in the central region of the calorimeter. The derived correction makes jet energies measured at any value of η equivalent to those measured in the central region. Finally, the jet response is derived as a function of p_T, using p_T balancing in $\gamma+$ jet or $Z+$ jet events. The p_T of the photon is well measured by the ECAL, whilst the p_T of the Z-boson can be measured reliably using the well-reconstructed decay products e^+e^- or $\mu^+\mu^-$. In this Monte Carlo analysis, however, the calibration was derived from simulated QCD di-jet events, by comparing reconstructed jets with truth-level particle jets. In general, the jet energy calibration depends on the choice of jet algorithm. The overall correction factor applied to the jet energies is known as the Jet Energy Scale (JES) and corrects the reconstructed jets back to the particle-jet level. This is not equivalent to the parton-level energy, which is discussed in Section 7.3.2.

Figure 6.3 shows the p_T, η, ϕ and number of jets reconstructed in Standard Model $t\bar{t}$ events and non-$t\bar{t}$ background events. For this analysis, only jets with $p_T > 15$ GeV were retained from the jet finding. As for electrons and muons, the jets from $t\bar{t}$ decays are typically higher p_T and more central than in non-$t\bar{t}$ decays. However, the most striking difference is in the jet multiplicity, where $t\bar{t}$ events contain, on average, 4 or 5 jets, whilst the number of jets in non-$t\bar{t}$ events is peaked at zero. This analysis requires events to have at least four jets, each with $p_T > 20$ GeV after calibration, and $|\eta| < 2.5$.

6.1.5 b-Tagging

In the semi-leptonic decay of a top-quark pair, two of the four resulting quarks are b-quarks. Like all quarks and gluons, the b-quark will hadronise to form a shower of particles. However, the hadronisation of a b-quark results in, amongst other particles, a b-hadron which has a relatively long lifetime of around 1.5 ps

and can travel around 3 mm in the detector before decaying. The resulting vertex is displaced from the primary vertex, and this separation can be resolved by the Inner Detector. A jet can thus be 'tagged' as originating from a b-quark by analysing the tracks associated with the jet. A reliable identification of the b-jets is valuable for the rejection of non-$t\bar{t}$ events, which are much less likely to contain a b-quark. For early-data analyses, the b-tagging strategy must be very robust, since the detector will be in a commissioning phase. The b-tagging used in this analysis is based on impact parameter and secondary vertex tagging, which are described below.

Impact Parameter Tagging

Impact parameter-based algorithms [31, 63] use the track impact parameters to derive a variable that can discriminate between b-jets and light jets. For a given jet, the d_0 and z_0 of each track are calculated with respect to the primary vertex, and used to calculate the impact parameter significances d_0/σ_{d_0} and z_0/σ_{z_0}. Here, σ_{d_0} and σ_{z_0} are the uncertainties on the impact parameter from the track fit. The impact parameter significances, S_i, for each track, i, are used as the discriminating variables, giving a high weight to well-measured tracks. The S_i can be compared to known distributions for b and light jets, and a track weight can be defined by the ratio of the probability functions $\mathrm{b}(S_i)/\mathrm{u}(S_i)$. Track weights are combined to give an over-all jet weight. The algorithm IP2D uses only the transverse impact parameter significance, while IP3D also uses the longitudinal significance.

Secondary Vertex Tagging

Secondary vertex algorithms [31, 63] identify b-jets by reconstructing a decay vertex that is displaced from the primary vertex. Tracks consistent with the primary

vertex are removed by a cut on the impact parameter significance. Track pairs are combined, and the invariant mass used to reject tracks from candidate vertices that are consistent with non-b secondary decays such as K_s^0 or the conversion of a photon to an electron-positron pair. The remaining tracks are used to make a secondary vertex and, for the algorithm SV1, a jet weight is derived using several properties of the vertex as discriminating variables. These include the mass of the assumed particle at the vertex, and the fraction of the jet energy that is related to the secondary vertex.

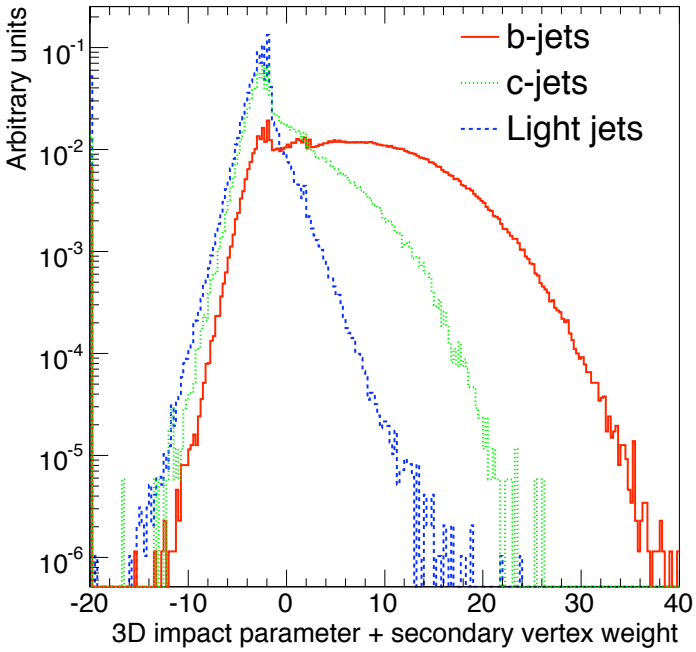

Figure 6.4: The b-tagging weight distribution IP3D + SV1 for b-jets, c-jets, light (u,d,s) jets taken from [31] This weight is used to assign b-tags to reconstructed jets, and includes information from the transverse and longitudinal impact parameter significances, and the secondary vertex.

This analysis uses the combined weight IP3D + SV1, which is shown in Figure 6.4 for b, c and light jets. The IP3D + SV1 weight for b-jets is typically higher than for c or light jets, since the measurable decay length of the b-hadron

results in tracks that are not evenly distributed around the primary vertex. Since c-hadrons also have a measurable (although shorter) decay length, however, the rejection of c-jets in the b-tagging process is limited as the weight distributions for b and c-jets have a large overlap. The peak of the IP3D + SV1 weight distribution is displaced from zero, which is thought to be due to detector misalignment included in the Monte Carlo simulations.

Typically, only tracks with $p_T > 1$ GeV, $\eta < 2.5$ and that are within the jet cone $\Delta R < 0.4$ are used for b-tagging. The selected tracks are also required to have at least 7 silicon hits, with at least two of the hits in the pixel detector, and one hit in the pixel b-layer. In this analysis, jets were tagged if they had a combined weight (IP3D + SV1) > 4.2, as recommended by the ATLAS Top Working Group. This results in a b-tagging efficiency of around 50%. For a b-tagging efficiency of 60%, a light jet rejection of around 150 can be obtained [31], although the performance is affected by the jet multiplicity of the event and the jet p_T and η. Jets at low p_T and/or high η can suffer from material effects in the Inner Detector, degrading the track quality. For jets with high p_T, the resulting high p_T b-hadrons can pass through the inner pixel layer before decaying, leading to decreased information on the reconstructed track. Figure 6.5 shows the IP3D, SV1 and IP3D + SV1 weights for each jet, along with the number of b-tagged jets in Standard Model $t\bar{t}$ and non-$t\bar{t}$ events. The IP3D and SV1 algorithms typically yield jet weights of less than zero for light jets, and the non-$t\bar{t}$ events, which contain fewer b-jets, are more strongly peaked towards negative weights. The b-jet multiplicity distribution illustrates the very small number of non-$t\bar{t}$ events that contain a b-tagged jet. This anaysis requires that two of the four leading (highest p_T) jets are b-tagged.

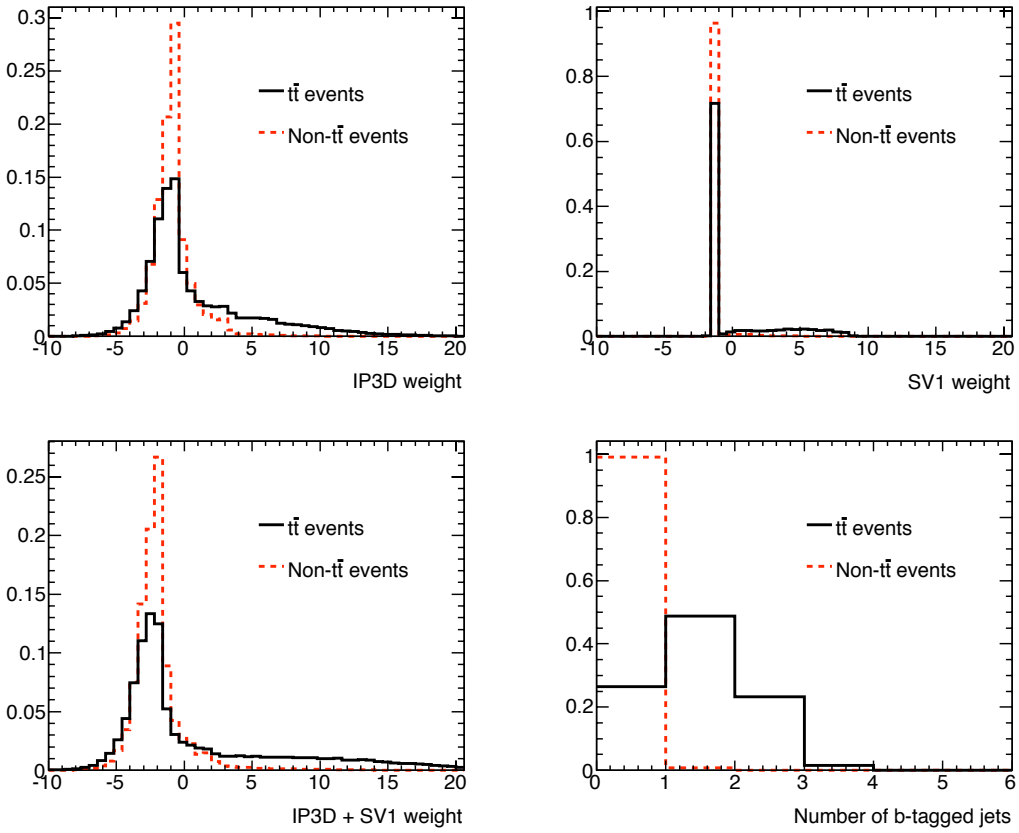

Figure 6.5: The b-tagging weight distributions IP3D, SV1 and (IP3D + SV1) for each jet, along with the number of jets in each event for Standard Model $t\bar{t}$ events and non-$t\bar{t}$ background events. Each distribution is normalised to unit area.

6.1.6 Missing E_T

Top pair decays in the semileptonic channel are expected to have a large missing transverse energy, E_T^{miss} due to the neutrino from the leptonically decaying W-boson. The determination of E_T^{miss} is challenging, as it involves several sub-detectors, and can be strongly affected by detector imperfections such as crack regions, or by high p_T muons that pass outside the geometrical acceptance of the detector. The measurement should, ideally, have a linear response over a large range of measured E_T^{miss}, and a good resolution.

The measurement of the E_T^{miss} is a three-stage process [31]. In the first stage, a rough estimate is derived from the calibrated calorimeter cell energies and the tracks measured in the Muon Spectrometer. The muon tracks used in the E_T^{miss} calculation are required to have a matching Inner Detector track in order to reduce the effect of fake tracks, but the contribution of the track to the E_T^{miss} is based only on information from the Muon Spectrometer. The STACO muons described in Section 6.1.3 are not used here in order to avoid double-counting effects, since the STACO algorithm accounts for energy loss of the muon in the calorimeters. In the second stage, a correction is applied to the measured E_T^{miss} to account for the energy lost by particles whilst traversing the cryostat between the LAr and tile calorimeters. The final stage refines the E_T^{miss} measurement, using the high-p_T physics objects such as electrons, photons and jets that have already been reconstructed in the event. Each calorimeter cell is associated with the relevant high-p_T object, and the contribution of these cells to the E_T^{miss} is replaced by the measurement from the object itself. Not all cells can be attributed to an object and for the remaining cells, the calibrated cell energies contribute to the calculation of the E_T^{miss}, after satisfying a noise cut. This method is found [31] to give a resolution of 8% for a measured E_T^{miss} of 50 GeV, and 3% for a measured E_T^{miss} of 200 GeV based on a mixture of $W \rightarrow l\nu$ and $t\bar{t}$ events.

This analysis requires the measured E_T^{miss} in the event, after the calibrations described above, to be greater than 20 GeV.

6.2 Event Selection Strategy

The Standard Model $t\bar{t}$ decays in the semi-leptonic channel are an irreducible background to the charged Higgs signal channel. Since both channels have essentially the same decay, with the exception of the intermediate boson on the hadronic side of the decay, it is not possible to use kinematic cuts to isolate the signal events. Figure 6.6 shows a selection of parameter distributions for objects in charged Higgs signal events for a 130 GeV charged Higgs, and for Standard Model $t\bar{t}$ background events. The parameter distributions are very similar, with the exception of the p_T of the b-tagged jets. In the signal decay, one of the b-jets is produced in association with the charged Higgs. As the charged Higgs mass increases, the available phase space for the decay is reduced, and the b-jet p_T is reduced accordingly.

Kinematic cuts are, however, still applied in this analysis, and their purpose is two-fold. Firstly, they select high quality top-pair candidate events; these events can be either charged Higgs signal events, or $t\bar{t}$ background events. Secondly, they are designed to reject a large fraction of the non-$t\bar{t}$ background events described in Chapter 5. Events were required to have passed one or both of the triggers EF_e15_medium or EF_mu15. Events were then rejected if they did not satisfy the following criteria, which are a summary of the requirements given in Sections 6.1.2 to 6.1.6.

1. Exactly one electron or exactly one muon.
2. The lepton has $p_T > 20$ GeV and $|\eta| < 2.5$ (a veto of electrons within $1.37 < |\eta| < 1.52$) and isolation < 6 GeV in a cone of $\Delta R = 0.2$ around the lepton.
3. $E_T^{miss} > 20$ GeV.

4. At least four jets with $p_T > 20$ GeV and $|\eta| < 2.5$.

5. Two of the four leading jets have a b-weight (IP3D + SV1) > 4.2.

Items 1 and 2 are referred to collectively as the lepton cut, where the veto of events with more than one lepton reduces much of the background from Standard Model $t\bar{t}$ events in the di-lepton channel. Item 3 is referred to as the E_T^{miss} cut, item 4 as the jet cut and item 5 as the 2-tag cut. No upper limit is imposed on the number of jets, since initial and final state radiation can lead to additional jets in an event. In the following, the jets with b-weight (IP3D + SV1) > 4.2 are referred to as b-tagged jets.

The philosophy of the analysis is then to calculate the invariant mass of the di-jet system from the intermediate boson on the hadronic side of the top-pair decay. This will be a H^+ boson in the case of a signal event, or a W-boson in the case of a Standard Model $t\bar{t}$ background event. The primary mass peak due to the Standard Model W-boson may then be accompanied by a secondary peak, due to the presence of a charged Higgs boson whose mass is not degenerate with the W-boson mass.

6.3 Cut Flow for 10 TeV Collisions

Table 6.1 shows the effect of each selection cut on the expected number of events for the H^+ signal and each of the main backgrounds, assuming 200 pb^{-1} of data at $\sqrt{s} = 10$ TeV [57]. The numbers quoted for the signal assume $\mathcal{B}(t \to bH^+) = 10\%$. This choice is arbitrary, since only the cut efficiencies are used in Chapter 7.5 to set limits, but it is in the region of the current Tevatron limits. For the Standard Model $t\bar{t}$ background, the quoted numbers assume $\mathcal{B}(t \to bH^+) = 0$. As expected

the background is dominated by the Standard Model $t\bar{t}$ events, with the single top and W+jets channels contributing smaller numbers of events. The signal acceptance is seen to decrease with an increasing charged Higgs mass. This is largely due to the double b-tag cut; for a heavier charged Higgs the associated b-jet is typically softer and more difficult to tag. The trigger efficiency is shown after all selection cuts have been applied.

6.4 Cut Flow for 7 TeV Collisions

Charged Higgs signal and Standard Model $t\bar{t}$ background events were generated following the descriptions given in Sections 5.2 and 5.3, but assuming $\sqrt{s} = 7$ TeV. Charged Higgs signal events were only generated for $m_{H^+} = 130$ GeV. The ATLAS detector simulation and object reconstruction is, however, constantly evolving and the samples were reconstructed using a later version of the software than was used for the study at $\sqrt{s} = 10$ TeV. Additionally, at the time this study was performed, the production of Monte Carlo events at $\sqrt{s} = 7$ TeV had only just begun, and the full range of non-$t\bar{t}$ background channels was not available. In order to produce results that were directly comparable with those derived with the 10 TeV Monte Carlo events, the decision was taken to make a generator-level comparison of the kinematical distributions and selection efficiencies between 7 TeV and 10 TeV. Scaling factors were then derived that, when applied to the efficiencies in Table 6.1, derived at $\sqrt{s} = 10$ TeV, give the expected efficiencies from events at $\sqrt{s} = 7$ TeV, which have been simulated and reconstructed with the same version of the software.[1] The selection efficiencies for non-$t\bar{t}$ background events were assumed to remain the same.

[1]The results shown in this section are the work of Paul Miyagawa, who used the analysis tools developed for the study at 10 TeV to repeat the analysis assuming 1 fb^{-1} of data collected at $\sqrt{s} = 7$ TeV.

The generator-level information allows the parent particles of the final state leptons, quarks and neutrinos to be identified. Since the events have not undergone detector simulation, the quarks are final state particles whose flavour is known. The following set of cuts was applied:

1. Exactly one final state lepton (e/μ) from W-boson decay with $p_T > 20$ GeV and $|\eta| < 2.5$. Isolation cuts are not relevant here, since the leptons have not undergone detector simulation.

2. The neutrino from the leptonic W-boson decay has $p_T > 20$ GeV.

3. All four quarks from the $t\bar{t}$ decay have $p_T > 20$ GeV and $|\eta| < 2.5$.

Table 6.2 shows a comparison of the resulting selection efficiencies for both 10 TeV and 7 TeV charged Higgs signal and $t\bar{t}$ background events. Items 1 and 2 above are referred to as the lepton and neutrino cuts, respectively. Item 3 is shown as three separate efficiencies, separating out the 'light quarks' originating from the W-boson or charged Higgs, from the two b-quarks. The label *b quark (W)* refers to the b-quark on the leptonic side of the $t\bar{t}$ decay, while *b quark (H)* refers to the b-quark on the hadronic side. The scale factors show the ratio of these efficiencies using 10 TeV and 7 TeV events. The overall scale factor is designed to be applied to the selection efficiencies shown in Table 6.1.

Figures 6.7 to 6.10 compare the kinematic distributions of the generator level leptons, light quarks and b-quarks in Standard Model $t\bar{t}$ events, and light quarks in charged Higgs signal events, at 7 TeV and 10 TeV. For 7 TeV events, the distributions are slightly more central and, as a result, the selection efficiencies are typically higher.

The top-anti-top system has the same kinematic properties, whether the quarks subsequently decay via a W-boson or a charged Higgs. By definition,

the leptonically decaying top (or anti-top) quark always decays via a W-boson and the resulting decay products (b, l, ν) should also have the same kinematics, regardless of whether the event is a signal or $t\bar{t}$ background event. This means that the scale factors for the lepton, neutrino and b-quark (W) should be the same for both Standard Model $t\bar{t}$ and charged Higgs signal events. The differences observed in Table 6.2 can be attributed to differences between Pythia, which was used to generate the signal events, and MC@NLO, which was used to generate the Standard Model $t\bar{t}$ background events. Since MC@NLO is a next to leading order generator, these results are assumed to be the most reliable, and the signal scale factors for the leptonic side of the decay are replaced with those from the $t\bar{t}$ background.

On the hadronic side of the decay, the W-boson and charged Higgs have different masses, which leads to differences in the kinematics of the light quarks and, consequently, the light quark scale factor. Only two boson mass points were available for study (the 80.4 GeV W-boson, and the 130 GeV charged Higgs). In order to infer the scale factors for the remaining charged Higgs mass points, the light quark scale factor was parameterised as a linear function of the boson mass. The overall scale factors for the signal samples were found to be 1.054 (90 GeV), 1.059 (110 GeV), 1.065 (130 GeV) and 1.071 (150 GeV) for the signal samples, and 1.043 for the Standard Model $t\bar{t}$ background.

The event selection efficiencies described in Sections 6.3 and 6.4 will be used in Chapters 7 and 8 to derive the expected upper limits on the branching ratio $\mathcal{B}(t \to bH^+)$. The limits derived assuming collisions at $\sqrt{s} = 7$ TeV and $\sqrt{s} = 10$ TeV should be directly comparable, since the scaling factors derived for $\sqrt{s} = 7$ TeV account for the different versions of the software used to reconstruct events at the two centre of mass energies.

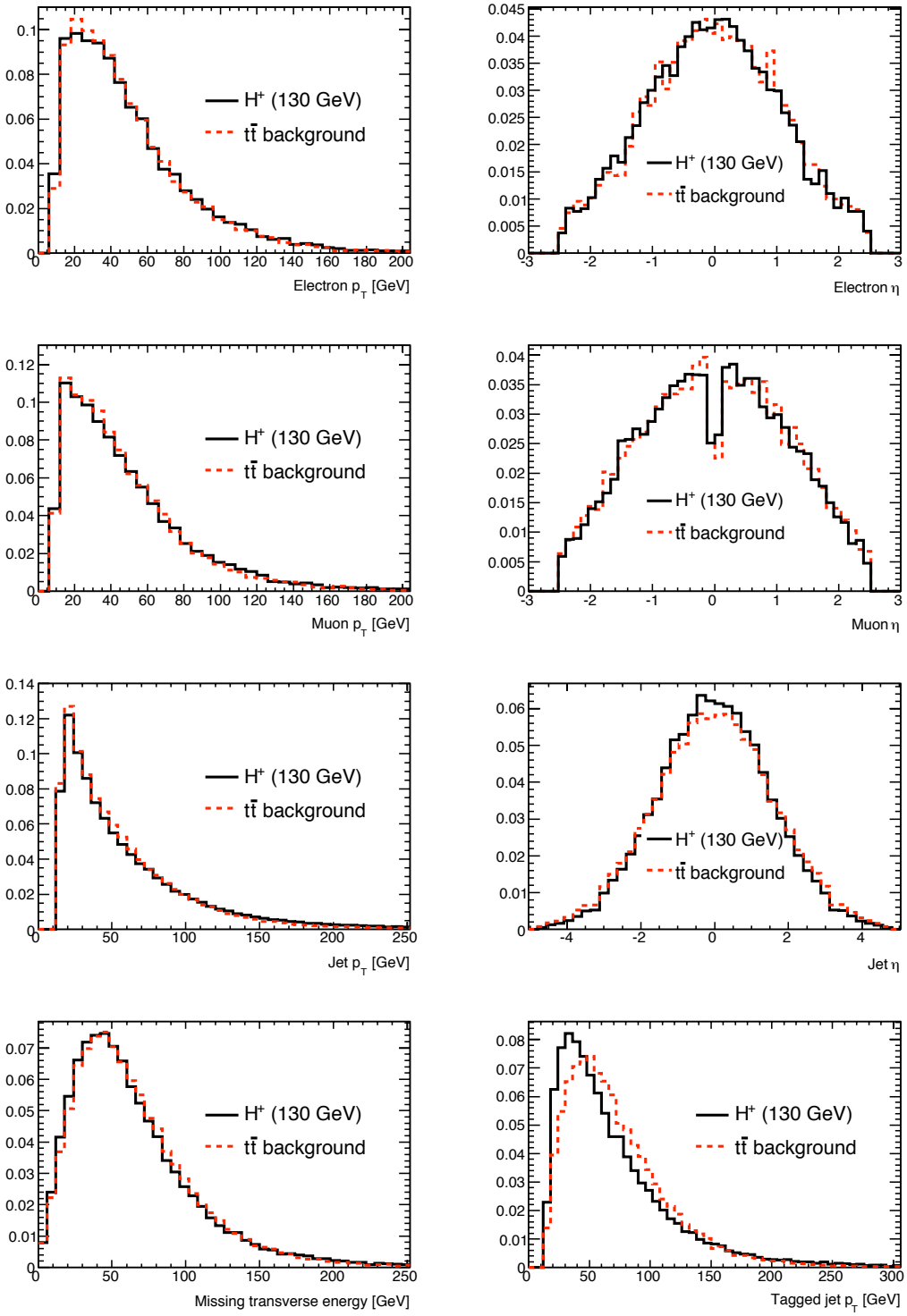

Figure 6.6: Parameter distributions for electrons, muons, jets and E_T^{miss}, together with the p_T of b-tagged jets. The distributions labelled $t\bar{t}$ background refer to Standard Model $t\bar{t}$ events. The non-$t\bar{t}$ backgrounds such as single top and W + jets are not shown here.

Process	Expected number of events after					
	no cut	1 lepton	E_T^{miss}	4 jets	2 b-tags	trigger
$H^+ \to c\bar{s}$, 90 GeV	4757	1880	1687	1052	267	235
$H^+ \to c\bar{s}$, 110 GeV	4757	1908	1719	1066	236	208
$H^+ \to c\bar{s}$, 130 GeV	4757	1921	1719	1040	188	165
$H^+ \to c\bar{s}$, 150 GeV	4757	1968	1753	969	121	107
SM $t\bar{t}$, not all hadronic	43680	17022	15428	7828	2117	1869
Single top, Wt-channel	2853	1210	1077	249	39	35
Single top, t-channel	8635	3428	3072	479	102	89
Single top, s-channel ($e\nu$)	152	72	64	4	2	1
Single top, s-channel ($\mu\nu$)	152	91	82	7	2	2
Wbb + jets	2320	795	678	131	29	26
$W \to e\nu$ + jets	17739	8107	6902	2288	7	7
$W \to \mu\nu$ + jets	17519	10136	8799	2997	10	8
$W \to \tau\nu$ + jets	17641	1229	1058	387	1	1

Table 6.1: Cut flow table for the charged Higgs boson signal channel, assuming $\mathcal{B}(t \to bH^+) = 10\%$, and for the main Standard Model backgrounds [57]. The number of events shown after each cut assumes collisions at a centre of mass energy of 10 TeV and an integrated luminosity of 200 pb^{-1}. All numbers are rounded. For the $Wb\bar{b}$ + jets channel, the initial number of events corresponds only to the samples $Wb\bar{b}$ + 2,3 partons, as listed in Table 5.3. The samples $Wb\bar{b}$ + 0,1 partons were found not to survive the selection cuts. Similarly, the numbers quoted for the $(W \to e/\mu/\tau + \nu)$ + jets channels correspond only to the samples $(W \to e/\mu/\tau + \nu)$ + 4,5 partons.

Signal $m_{H^+} = 130$ GeV					
Energy	7 TeV		10 TeV		Scale factors
Cut	Number of events	Efficiency	Number of events	Efficiency	for 7 TeV
none	23231	-	29800	-	-
lepton	19079	0.821	24041	0.807	1.017
neutrino	17028	0.893	21336	0.887	1.007
light quarks	14486	0.851	17452	0.818	1.040
b quark (W)	13330	0.920	15773	0.904	1.018
b quark (H)	10783	0.809	12656	0.802	1.009
Overall	-	0.464	-	0.425	1.094

SM $t\bar{t}$ (not hadronic)					
Energy	7 TeV		10 TeV		Scale factors
Cut	Number of events	Efficiency	Number of events	Efficiency	for 7 TeV
none	42574	-	149014	-	-
lepton	34524	0.811	119439	0.802	1.011
neutrino	30710	0.890	106539	0.892	0.998
light quarks	21638	0.705	73179	0.687	1.026
b quark (W)	19600	0.906	65938	0.901	1.006
b quark (H)	17778	0.907	59670	0.905	1.002
Overall	-	0.418	-	0.401	1.043

Table 6.2: A generator-level comparison of the event selection efficiencies at $\sqrt{s} = 7$ TeV and $\sqrt{s} = 10$ TeV, for Standard Model $t\bar{t}$ events (using MC@NLO) and for charged Higgs events with $m_{H^+} = 130$ GeV (using Pythia) [58]. The overall scale factor was found to be 4.3% for Standard Model $t\bar{t}$ events, and 9.4% for charged Higgs signal events. The scale factors for the lepton, neutrino and b quark (W) cuts are expected to be the same for the Standard Model $t\bar{t}$ and charged Higgs signal events. The variations are attributed to the different Monte Carlo generators used for the two channels.

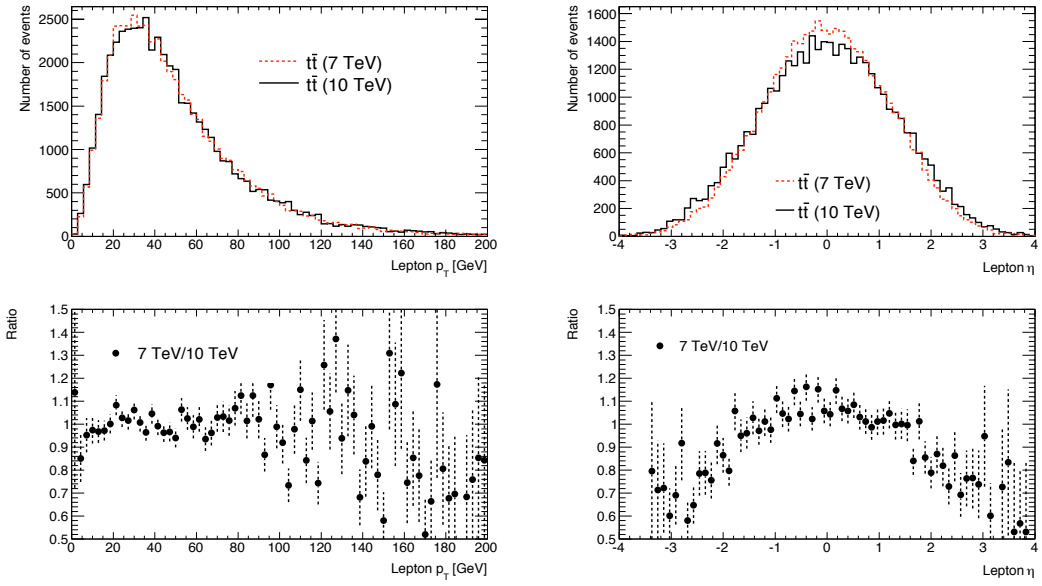

Figure 6.7: A generator-level comparison of the lepton (e, μ) p_T and η distributions in Standard Model $t\bar{t}$ events for $\sqrt{s} = 7$ TeV and $\sqrt{s} = 10$ TeV [58].

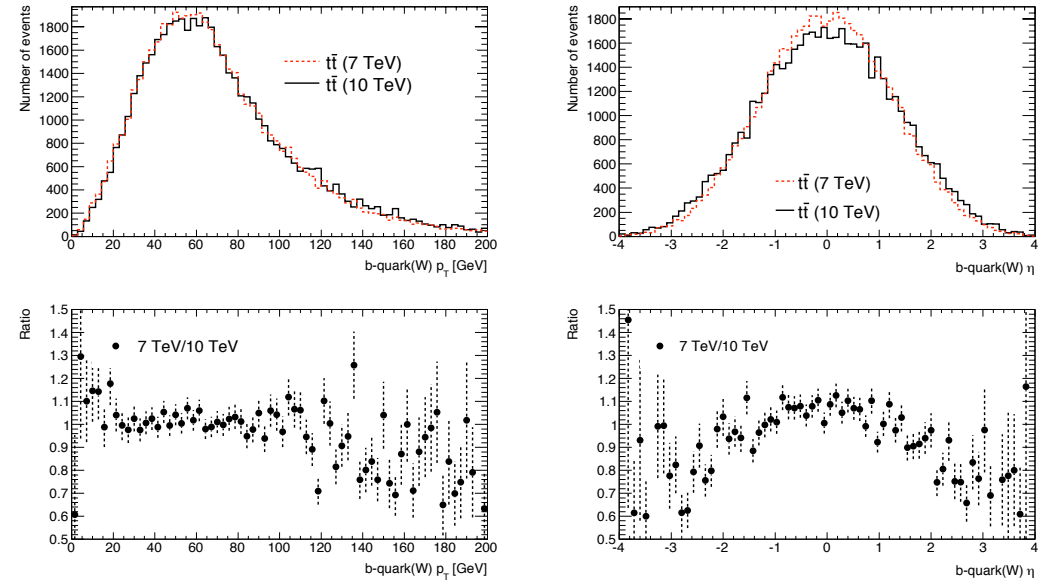

Figure 6.8: A generator-level comparison of the b-quark p_T and η distributions in Standard Model $t\bar{t}$ events for $\sqrt{s} = 7$ TeV and $\sqrt{s} = 10$ TeV [58].

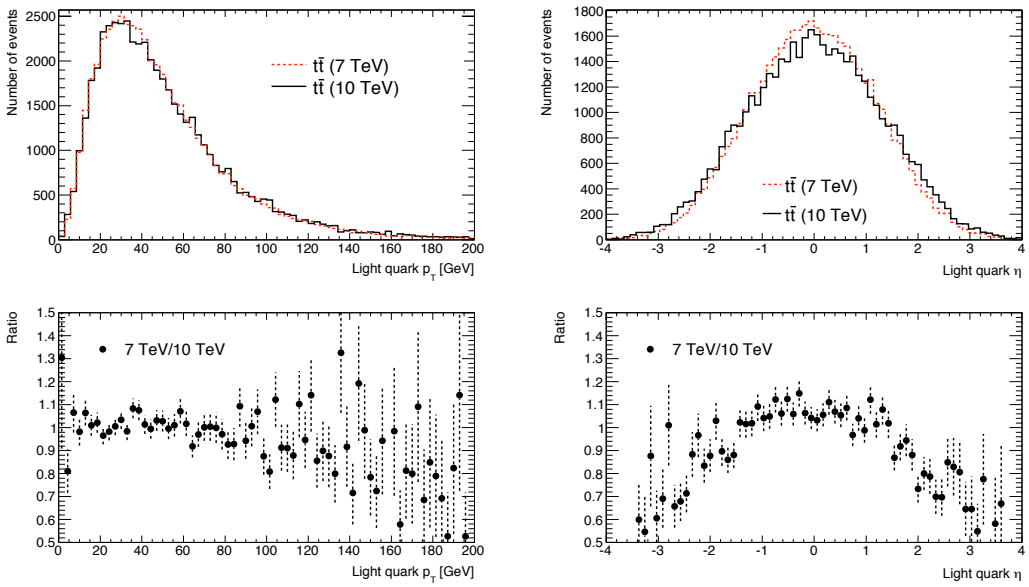

Figure 6.9: A generator-level comparison of the light quark p_T and η distributions in Standard Model $t\bar{t}$ events for $\sqrt{s} = 7$ TeV and $\sqrt{s} = 10$ TeV [58].

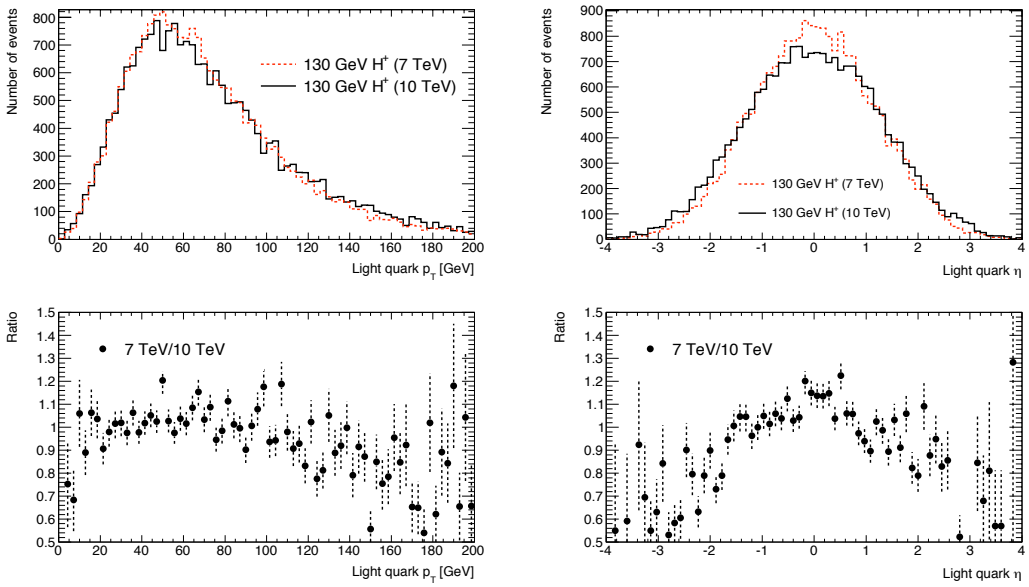

Figure 6.10: A generator-level comparison of the light quark p_T and η distributions in charged Higgs signal events with $m_{H^+} = 130$ GeV for $\sqrt{s} = 7$ TeV and $\sqrt{s} = 10$ TeV [58].

Chapter 7

Analysis

This chapter describes the analysis techniques used to derive the expected upper limits on the branching ratio $B(t \rightarrow bH^+)$ using the Monte Carlo samples described in Chapter 5 and the event selection cuts described in Chapter 6. A kinematic fit was used to increase the discriminating power between signal and background events, and a maximum likelihood method was used to evaluate the expected upper limits.

7.1 Di-jet Mass Reconstruction

Top-pair decays are complicated to study, due to the high multiplicity of jets in the final state. To reconstruct any high level object in the event, such as the top quarks or the intermediate bosons, requires the final state jets to be associated with the partons from the $t\bar{t}$ decay. An incorrect jet to parton assignment will clearly destroy the kinematics of the event. This analysis is based on the shape of the mass spectrum of the reconstructed di-jet from charged Higgs or W-boson

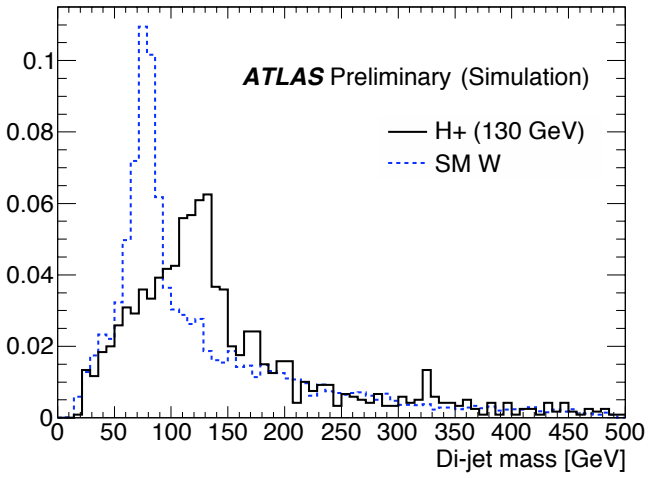

Figure 7.1: The reconstructed di-jet mass spectra from Standard Model $t\bar{t}$ events and for an example H^+ mass point of 130 GeV [57]. The charged Higgs distribution is from events where the W-boson on the leptonic side of the decay decays as $W \to e/\mu + \nu$. Both distributions are normalised to unity.

decays. Since the event selection cuts described in Section 6.2 reject events that do not have two of the four hardest (leading) jets tagged as b-jets, the two untagged jets of the four hardest jets can be assigned to the di-jet system. The invariant mass of this di-jet should reflect the mass of the charged Higgs or W-boson. This assumes that the four hardest jets in the event originate from the four partons from $t\bar{t}$ decay, and that the b-jets have been correctly tagged. The resulting di-jet mass distributions for the W-boson and a 130 GeV charged Higgs are shown in Figure 7.1. [57] The distributions are not well separated, with large widths and long tails. This situation deteriorates further as the charged Higgs mass decreases, and the signal and background tend to approximately the same distribution. For this reason, a kinematic fitting technique is employed to improve the separation between the signal and background distributions.

7.2 The Kinematic Fit

The resolution of the di-jet mass peak from charged Higgs signal or $t\bar{t}$ background decays can be improved by reconstructing the entire $t\bar{t}$ event and imposing constraints on the top quark and W-boson masses. This kinematic fitting method is based on the technique used to fit the top quark mass at the CDF experiment [64] and has two main advantages.

1. The constraints on the top quark and W-boson masses are used to rescale the p_T of the final state lepton and jets within their experimental resolutions. This rescaling of jet energies leads to an improved measurement of the di-jet mass.

2. The fitter selects the combination of jets that are most likely to originate from the di-jet system. Although this is trivial with the requirement of two b-tagged jets, this feature of the fitting would allow events with one or zero b-tagged jets to be included in the future.

The following χ^2 function can be defined to describe a generic $t\bar{t}$ event in the semi-leptonic decay channel.

$$\begin{aligned}\chi^2 &= \frac{(M_{jjb}-M_t)^2}{\Gamma_t^2}+\frac{(M_{l\nu b}-M_t)^2}{\Gamma_t^2}+\frac{(M_{l\nu}-M_W)^2}{\Gamma_W^2}+ \\ &\sum_{i=l,4jets}\frac{(p_T^{i,fit}-p_T^{i,meas})^2}{\sigma_i^2}+\sum_{j=x,y}\frac{(p_j^{UE,fit}-p_j^{UE,meas})^2}{\sigma_{UE}^2}.\end{aligned} \tag{7.1}$$

The first two terms of Equation 7.1 constrain the masses of the reconstructed top quarks on both the hadronic and leptonic side of the event. The hadronic side top quark mass is formed using the four-vector sum of the two untagged jets and one of the b-tagged jets. The leptonic side top mass is formed from the four-vector sum of the lepton, the neutrino (discussed in Appendix A) and the

remaining b-tagged jet. The top quark width, Γ_t, was taken to be 1.5 GeV, and M_t is the mass of the top quark, 172.5 GeV, consistent with the PDG value [65]. As discussed in Chapter 5, the Monte Carlo events were also generated with $M_t = 172.5$ GeV.

By definition, the intermediate boson on the leptonic side of the event (constructed from the lepton and neutrino) is a W-boson, for both signal and $t\bar{t}$ background events, and its mass can be constrained to the W-boson mass, 80.4 GeV. This is described by the third term, where Γ_W was taken to be 2.12 GeV. The transverse energy of the neutrino is attributed to the measured E_T^{miss}, and the neutrino four vector is initially calculated by requiring that the four-vector sum of the lepton and neutrino gives a W-boson mass of 80.4 GeV. The details of this calculation are given in Appendix A, and result in two possible initial solutions for the neutrino four-vector. Under this assumption, the third term of Equation 7.1 will not contribute to the χ^2. The purpose of this term is motivated below, along with the strategy to deal with the multiple neutrino solutions.

For each event, the χ^2 function is minimised using MINUIT [66]. In the fit, the transverse momenta of the lepton and the four leading jets are permitted to vary within their experimental uncertainties, while the η and ϕ remain fixed. This is described by the fourth term of Equation 7.1, where the σ_i represent the experimental resolutions for the jet and lepton objects. The resolution on the measured jet p_T, σ_{jet}, was derived from Monte Carlo by comparing the p_T of generator level and reconstructed jets, as described in Section 7.3.2.

The final term describes the unclustered energy, UE, which is defined as the four-vector sum of the energy not contained in the final state lepton or the four leading jets. The sum encompasses the remaining jets that were not part of the four leading jets, and any energy that was not clustered into jets. This includes,

for example, the jets with $p_T < 15$ GeV that were not retained after the jet finding. This construct completes the description of the event and allows the E_T^{miss} to be recalculated at each stage of the fit, using

$$p_T^{\nu} = -(\sum_{i=l,4jets} p_T^i + p_T^{UE}). \tag{7.2}$$

This, in turn, modifies the neutrino four-vector, leading to the requirement of the third term in Equation 7.1. The resolution on the unclustered energy was taken to be $0.4\sqrt{UE}$, following [13].

After minimisation, the χ^2 describes how much a given event resembles a $t\bar{t}$ event. Although the p_T of the final-state objects can be rescaled to satisfy the constraints on the top quark and W-boson masses, this will clearly impose a χ^2 penalty. Thus, the χ^2 value is powerful in rejecting events that are either badly reconstructed, or originate from non-$t\bar{t}$ processes. The mass of the intermediate boson on the hadronic side of the decay is left unconstrained in the fit. The intention is that the rescaling of the momenta of the final-state objects, based on known constraints, will lead to an improved measurement of the mass of this boson.

It is not known *a priori* which of the neutrino solutions is the correct one. There are also two possible assignments of the four leading jets to the partons from $t\bar{t}$ decay that are consistent with the b-tagging information. This corresponds to an interchange of the b-jets. The two untagged jets attributed to the di-jet system originate from the same charged boson and are indistinguishable in terms of jet assignment. For each combination, the χ^2 function was fitted, and the combination yielding the lowest χ^2 was taken to be the correct assignment. Only the four leading jets were considered in the fit.

7.3 Jet Corrections

The generic jet energy calibrations described in Section 6.1.4 correct jet energies back to the truth-particle level. The energy of each calibrated jet then reflects the energy deposited in the detector by all constituent particles of a given hadron shower. This, however, does not precisely reflect the energy of the original parton. The generic jet corrections do not take into account differences in the fragmentation of light (u, d, s, c) quarks, and b-quarks. For example, the component particles of a b-jet typically have a harder p_T spectrum, due to the higher mass of the b-quark. In addition, semi-leptonic decays in b-jets produce a neutrino, which cannot be measured as part of the jet and, instead, contributes to the generic E_T^{miss} of the event. A $t\bar{t}$ decay in the semi-leptonic channel also results in a busy detector environment; it is possible that jets can overlap, leading to mis-measurement of their energy.

The χ^2 fitting technique described in Section 7.2 assesses the quality of events by constraining, for example, the four-vector sum of the two un-tagged jets and one of the b-tagged jets to reproduce the top-quark mass. Clearly, this will be biassed if the jet energies are measured in a systematically incorrect way. The following jet corrections are designed to correct the calibrated jet energies back to the parton-level energies. The corrections are based on $t\bar{t}$ Monte Carlo events in the semi-leptonic decay channel, and are derived separately for light jets and b-jets in order to give the best possible measurement of the parton-level energies.

7.3.1 Light-jet Correction

Each jet was corrected with a light-jet correction derived by the ATLAS Top Working Group. This correction was derived from hadronically decaying top

quarks in Standard Model $t\bar{t}$ Monte Carlo events, in which the four-vector sum of the light (u, d, s, c) quark pair resulting from the decay $W \rightarrow qq'$ was constrained to reproduce the W-boson mass on an event-by-event basis. This is a p_T and η-dependent correction to the jet energies.

7.3.2 Top-specific Correction

The light-jet correction, based on the W-boson mass, does not contain any information about b-jets. In order to correct the b-jet energies for hadronisation and parton showering effects, a response function was derived[1], which corrects the calibrated jet energies back to the original parton-level energies. This is referred to as the top-specific correction, and is a p_T-dependent function derived using the generator-level information in MC@NLO $t\bar{t}$ events as follows. The selection cuts described in Section 6.1 were applied, and the light-jet correction, described in Section 7.3.1, was applied to all jets in the event. Events were then selected where all four of the leading jets were matched to the generator-level quarks within $\Delta R < 0.2$. The transverse momentum of the generator-level quark, p_T^{true}, was compared with that of the calibrated jet, p_T^{cal}, using:

$$\text{Response} = \frac{p_T^{true} - p_T^{cal}}{p_T^{cal}} \tag{7.3}$$

and the response was parameterised as a function of p_T^{cal} as:

$$\text{Response} = e^{A+B.p_T^{cal}} + C. \tag{7.4}$$

The response functions were evaluated separately for b-quarks, and light (u,d,s,c) quarks, and are shown in Figure 7.2, along with the p_T resolution, σ_{jet}, as a function of p_T, which was derived using a similar method. This correction could also be derived as a function of η, although larger Monte Carlo statistics would be

[1]Work by Alex Martyniuk at the University of Manchester

required. As expected, the top-specific correction for the light jets is essentially flat, since the light jet correction was applied before the top-specific correction was derived.

The jet correction procedure for each event is as follows. Each jet was corrected with the light-jet correction. The relevant top-specific correction was then applied to each jet; b-tagged jets were corrected with the response function derived from b-quarks and all other jets were corrected with the response function derived from light quarks. These corrections were applied before performing the χ^2 fit.

7.4 Di-jet Mass Templates

Figure 7.3 shows the di-jet mass distribution from Standard Model $t\bar{t}$ background events both before and after the kinematic fitting. The fitter rescales the jet and lepton transverse momenta in order to best satisfy the constraints on m_t and m_W. The constraints on the top-quark mass prevent the di-jet mass from exceeding m_t, and the excess of events on the high-mass side of the fitted di-jet mass peak is attributed to those events lying in the tail of the unfitted distribution. However, these contributions to the di-jet mass distribution can result from badly reconstructed events, incorrect jet assignment, or final state radiation from one of the four jets of interest, and are not necessarily useful for this analysis.

The χ^2 value is a powerful discriminant for selecting well measured events with the correct jet assignment. Events requiring a large rescaling of the jet and lepton p_T in order to satisfy the constraints on m_t and m_W will have a large χ^2 value. Figure 7.4 (left) shows the di-jet mass distribution from Standard Model $t\bar{t}$ background events using events with $\chi^2 > 10$ and those with $\chi^2 < 10$. Events

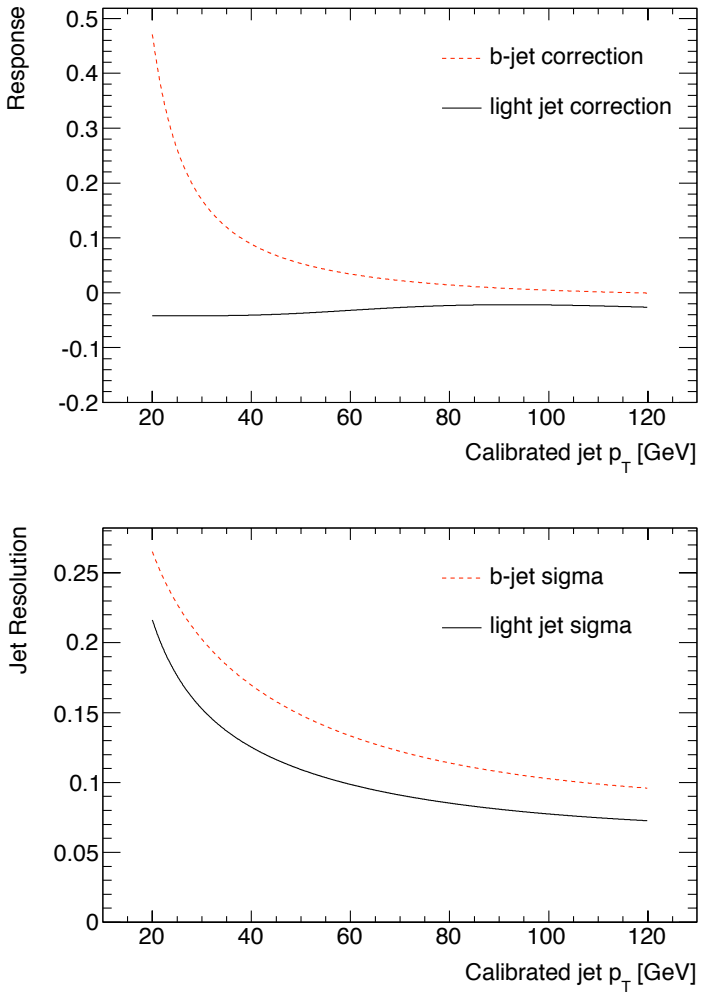

Figure 7.2: Above, the top specific correction for b-jets and light (u,d,s,c) jets as derived from MC@NLO $t\bar{t}$ events. Below, the jet p_T resolutions, σ_{jet}, for b-jets and light (u,d,s,c) jets, which are used in the χ^2 minimisation.

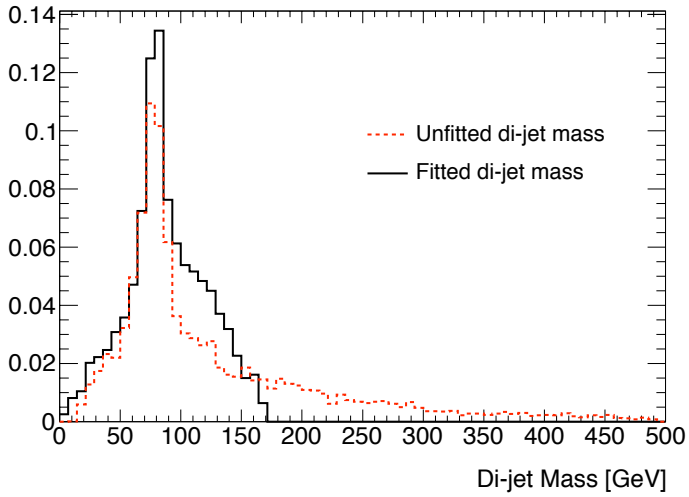

Figure 7.3: The di-jet mass distribution from Standard Model $t\bar{t}$ background events before and after the kinematic fitting. The normalisation is to unit area.

with $\chi^2 > 10$ have a relatively flat distribution, whereas those with $\chi^2 < 10$ are strongly peaked around the W-boson mass.

The χ^2 value is strongly correlated with the mass of the reconstructed top quark on the hadronic side of the $t\bar{t}$ decay (before the rescaling of the jet and lepton p_T). This quantity is referred to as M_{top}. The χ^2 value is less well correlated with the di-jet mass, suggesting that a tighter χ^2 cut would, in addition to rejecting more events, have a limited effect on the resolution of the di-jet mass distribution. Studies showed that rejecting events with $M_{top} > 195$ GeV significantly improved the di-jet mass resolution. A double sided cut, retaining only events with 195 GeV$> M_{top} > 155$ GeV was found to remove many events from the peak of the di-jet mass distribution, and was not used in the analysis. Figure 7.4 (right) shows the di-jet mass distribution from Standard Model $t\bar{t}$ background events using events with $\chi^2 < 10$, where the events have been separated into those with $M_{top} < 195$ GeV and $M_{top} > 195$ GeV.

Events were rejected if they had $\chi^2 > 10$, or if $M_{top} > 195$ GeV. The effect

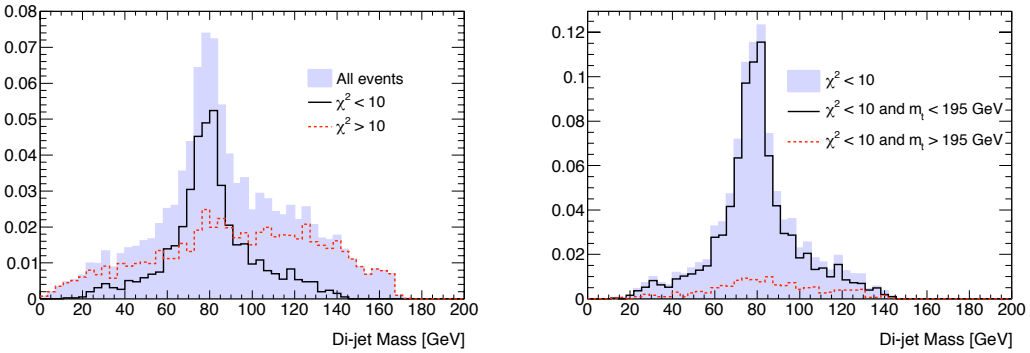

Figure 7.4: The di-jet mass distribution from Standard Model $t\bar{t}$ background events after the kinematic fitting. (Left) The blue histogram shows the distribution for all events, and has been normalised to unit area. The black and red lines respectively show the same distribution separated into events with $\chi^2 < 10$ and $\chi^2 > 10$. (Right) The blue histogram shows all events with $\chi^2 < 10$. The black and red lines respectively show the same distribution separated into events with $M_{top} < 195$ GeV and those with $M_{top} > 195$ GeV.

of these cuts is shown in Table 7.1 and the overlaid di-jet mass distributions for the W-boson and a 130 GeV H^+ are shown in Figure 7.5. The efficiency of the χ^2 cut is low, and many events are lost. However, the di-jet mass distributions from the remaining events show good separation between the H^+ signal and Standard Model $t\bar{t}$ background. In a shape analysis such as this, there is a trade-off between maximising the number of signal events and generating a distribution with good power to distinguish between signal and background. The templates for each charged Higgs mass point, the Standard Model $t\bar{t}$ background and the non-$t\bar{t}$ background are shown separately in Figure 7.6. These final templates are used to set limits in the remaining chapters.

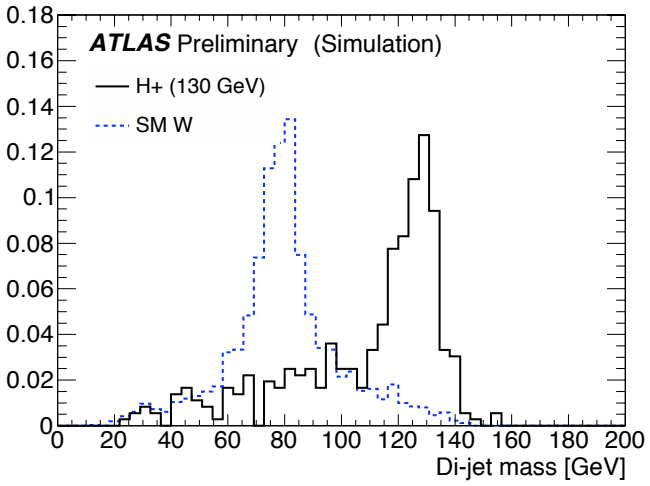

Figure 7.5: The di-jet mass distribution for a 130 GeV charged Higgs and the Standard Model W-boson after fitting [57]. The charged Higgs distribution is from events where the W-boson on the leptonic side of the decay decays as $W \rightarrow e/\mu + \nu$. A cut has been made on the χ^2 of the best jet assignment at 10 and the reconstructed top mass on the hadronic side of the decay is required to be less than 195 GeV.

7.5 Limit Setting

7.5.1 The Binned Maximum Likelihood Method

The probability of observing a particular set of data, x_i, is described by the likelihood:

$$L(x_i; a) = \prod_i P(x_i; a) \tag{7.5}$$

where a describes the parent distribution from which the data are drawn. The maximum likelihood method is a statistical estimator based on the likelihood; given a particular parent distribution, it provides an estimate, $\hat{a}$, of the value of a that makes the recorded data-set most likely.

In this analysis, the maximum likelihood method is applied to the binned template distributions shown in Figure 7.6. The binned maximum likelihood is

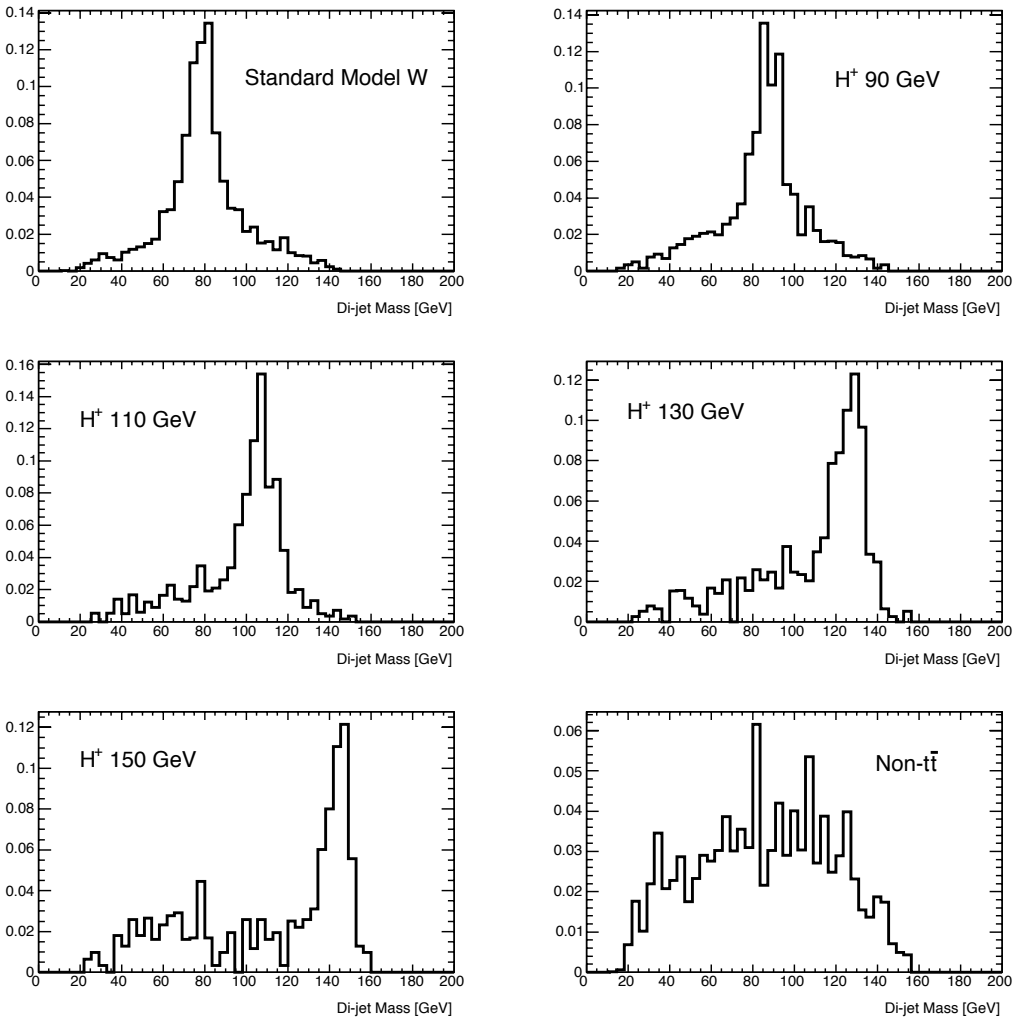

Figure 7.6: The di-jet mass templates for each charged Higgs mass point (90, 110, 130 and 150 GeV) along with the background shapes from $t\bar{t}$ and non-$t\bar{t}$ background events. The final charged Higgs templates include events where the W-boson decays as $W \rightarrow e/\mu + \nu$ and $W \rightarrow \tau + \nu$ As the charged Higgs mass approaches the W-boson mass, the signal template tends to that of the $t\bar{t}$ background.

described by

$$\text{Likelihood} = \prod_i \frac{\nu_i^{n_i} e^{-\nu_i}}{n_i!} \tag{7.6}$$

where the product is over the number of bins, i. In each bin ν_i is the expected number of events, while n_i is the observed number of events. Since the bin contents are subject to Poisson statistics, this definition accounts for the fact that the overall normalisation of the distribution is not known *a priori*.

7.5.2 Likelihood Definition

Assuming no signal beyond the Standard Model, a binned maximum likelihood was used to find the upper limit on the branching ratio $\mathcal{B}(t \to bH^+)$ at 95% confidence level (CL). The limits found assume a charged Higgs decaying with $\mathcal{B}(H^+ \to c\overline{s}) = 1$ and an integrated luminosity, $\mathcal{L}_{int}$, of 200 pb^{-1} at a collision centre of mass energy of 10 TeV. The likelihood function, LH, is based on the shapes of the template distributions shown in Figure 7.6 and is given by:

$$LH = \prod \frac{\nu_i^{n_i} e^{-\nu_i}}{n_i!} \bigotimes G(N_{bkg}, \sigma_{N_{bkg}}). \tag{7.7}$$

This is constructed from the binned likelihood described in Section 7.5.1 together with a Gaussian constraint on the number of background events, N_{bkg}. The shape of the n_i represents an observed data-distribution, while ν_i is the expected number of events in each bin, i, based on the shapes of the template distributions. ν_i can be parameterised as:

$$\begin{aligned} \nu_i = \\ N_{t\bar{t}} \times 2 \times \mathcal{B}(t \to H^+b)[1 - \mathcal{B}(t \to H^+b)] \times A_{H^+} \times P_i^{H^+} \times \mathcal{B}(W \to \ell\nu) + \\ N_{t\bar{t}} \times [1 - \mathcal{B}(t \to H^+b)]^2 \times A_W \times P_i^W \times \mathcal{B}(W \to \ell\nu)[2 - \mathcal{B}(W \to \ell\nu)] + \\ N_{bkg} \times P_i^{bkg}. \end{aligned} \tag{7.8}$$

Here, $N_{t\bar{t}}$ is the expected total number of $t\bar{t}$ events that are produced, encompassing all possible decay modes. Thus, $N_{t\bar{t}} = \sigma_{t\bar{t}} \times \mathcal{L}_{int}$. A_{H+} and A_W are the acceptances for H^+- and W-mediated events through the event selection cuts, and are derived from Table 7.1. Note that A_W is derived from a Monte Carlo sample containing both semi-leptonic and fully leptonic $t\bar{t}$ decays, so this is the acceptance for inclusive lepton $t\bar{t}$ events. The prior probabilities $P_i^{H^+}$, P_i^W and P_i^{bkg} are respectively the probabilities to find signal, $t\bar{t}$ and non-$t\bar{t}$ events in each bin of the relevant template distribution (shown in Figure 7.6), and describe the shape of the Monte Carlo templates. For example, the first line of Equation 7.8 describes the expected number of charged Higgs signal events in each bin of the data distribution. Beginning with the total number of $t\bar{t}$ events, multiplying by $2 \times \mathcal{B}(t \to H^+b)[1 - \mathcal{B}(t \to H^+b)]$ gives the number of these events where one top quark decays to bH^+ and the other to bW. Multiplying by A_{H^+} gives the total number of charged Higgs signal events that are expected to pass the selection cuts, and further multiplication by $P_i^{H^+}$ gives the expected number of charged Higgs signal events in each bin of the data histogram. The factor $\mathcal{B}(W \to \ell\nu)$ is included, to represent the leptonically decaying W-boson from the other top quark. The remaining two lines of equation 7.8 describe respectively the expected numbers of $t\bar{t}$ background and non-$t\bar{t}$ background events in each bin. The factor $\mathcal{B}(W \to \ell\nu)[2 - \mathcal{B}(W \to \ell\nu)]$ accounts for the fact that the Standard Model $t\bar{t}$ Monte Carlo sample contains both semi-leptonic and fully-leptonic $t\bar{t}$ decays.

The number of signal and $t\bar{t}$ background events are correlated - their relative proportions depend on the branching ratio $\mathcal{B}(t \to bH^+)$. The number of non-$t\bar{t}$ background events, however, is independent of this branching ratio, and studies in the ATLAS Top Working Group are ongoing to use data to estimate the size of non-$t\bar{t}$ backgrounds to top analyses. At the point where this analysis is performed on real data, the number of non-$t\bar{t}$ events is expected to be known to a precision

of around 30%. For this reason, the number of non-$t\bar{t}$ background events is an input to the likelihood fit, and has a Gaussian constraint. Due to the presence of the product in Equation 7.7 and the relatively large number of bins, the negative log likelihood is used, and the quantity -($\ln LH$) is minimised using MINUIT. There are three parameters in the fit:

- The branching ratio $\mathcal{B}(t \to bH^+)$.
- The total number of $t\bar{t}$ events, $N_{t\bar{t}}$. This includes all $t\bar{t}$ events, decaying via a W-boson or a charged Higgs, into any $t\bar{t}$ final state (fully-leptonic, semi-leptonic or fully-hadronic).
- The number of non-$t\bar{t}$ background events, N_{bkg}.

After all selection cuts, the predicted number of non-$t\bar{t}$ events is $N_{bkg} = 30 \pm 9$, as described in Table 7.1, where a 30% uncertainty has been assigned in order to reflect the expected uncertainty on the number of non-$t\bar{t}$ background events in data.

7.5.3 Pseudo-data

The performance of the likelihood fit is tested using 1000 simulated pseudo-experiments. The test assumes a null-Higgs hypothesis and the expected di-jet mass distribution is constructed using the templates shapes for the $t\bar{t}$ and non-$t\bar{t}$ backgrounds combined according to their expected contributions. The purpose of the pseudo-data test is to ascertain to what extent statistical fluctuations of a template distribution containing zero charged Higgs signal events can be interpreted by the likelihood fit as a non-zero signal contribution. The test also allows

the likelihood fit to be checked for possible bias. Each pseudo-experiment is generated using bin-by-bin Poisson fluctuations of the expected distribution. The content of each bin is replaced by a random number selected from a Poisson distribution centred on the bin content. Several example pseudo-data distributions are shown in Figure 7.7.

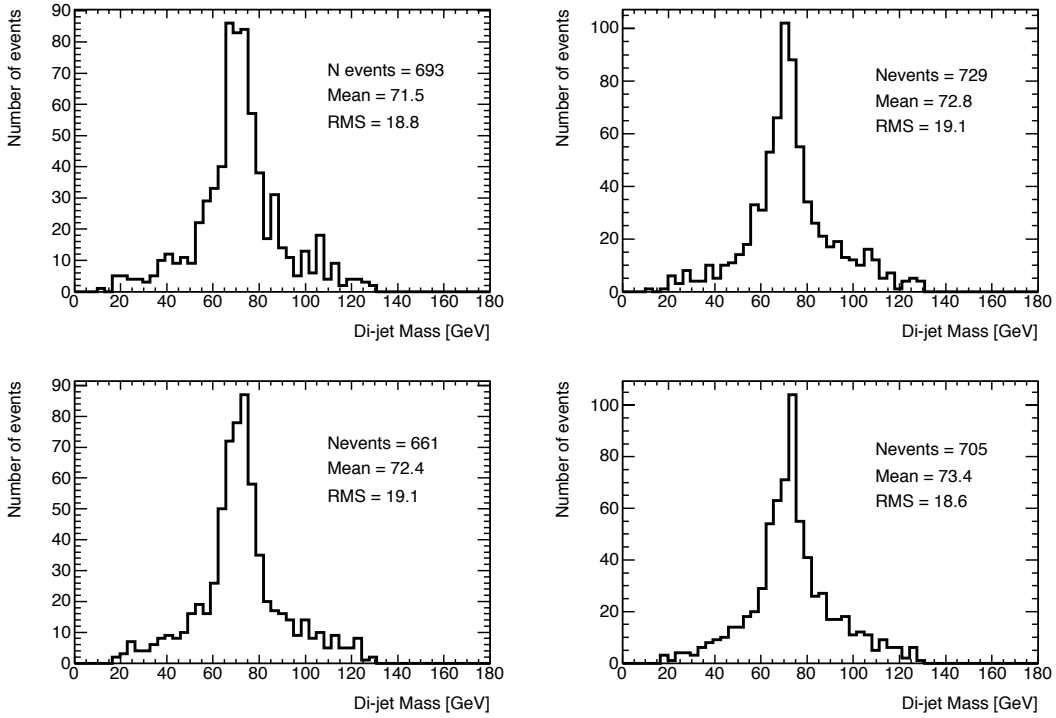

Figure 7.7: Four example pseudo-data distributions generated by Poisson smearing of the bin contents of the template distributions. A null-Higgs hypothesis was assumed. The template distribution was normalised to the expected number of $t\bar{t}$ and non-$t\bar{t}$ background events. However, the Poisson smearing alters the bin contents, meaning that the normalisation of each pseudo-data sample is not necessarily identical.

For each pseudo-experiment, the negative log likelihood is minimised. This essentially determines what fractional composition of the charged Higgs signal, Standard Model $t\bar{t}$ background and non-$t\bar{t}$ background template distributions best reproduces the pseudo-data distribution. The fitted branching ratio $\mathcal{B}(t \to bH^+)$

for a given pseudo-experiment can be positive if the pseudo-data distribution contains an excess of events around the charged Higgs mass of interest, or negative if there is an absence of events. The branching ratio is not constrained to have physical, positive values. Over all pseudo-experiments, the fitted number of signal events (derived from the fitted branching ratio $\mathcal{B}(t \to bH^+)$) is expected to be zero, as a result of the null-Higgs hypothesis, and the numbers of $t\bar{t}$ and non-$t\bar{t}$ background events are expected to reproduce the numbers given in Table 7.1. For this reason, this analysis also provides a measurement of the $t\bar{t}$ cross-section. The results of the likelihood fit are shown in Figure 7.8.

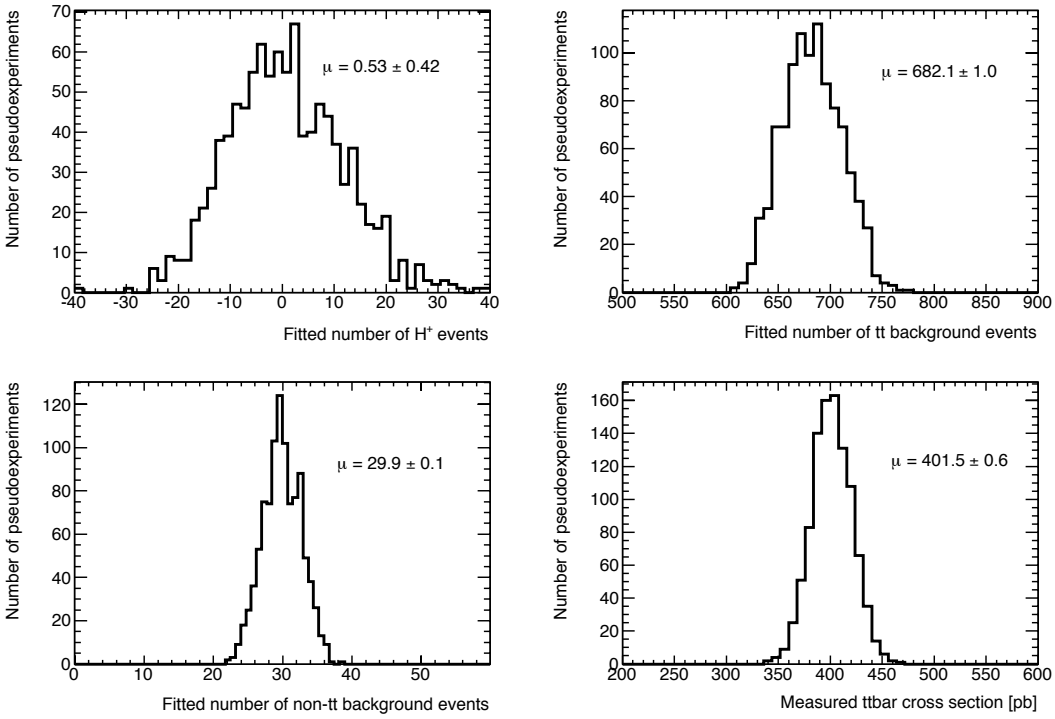

Figure 7.8: The output of the likelihood fit, assuming a 130 GeV charged Higgs. Shown are the fitted number of signal and background events from each pseudo-experiment, along with the fitted $t\bar{t}$ cross section. The mean, μ, of a Gaussian fit is shown on each plot, and each parameter is consistent with the input value.

The likelihood fit is tested for any possible bias by considering the pull distribution of the fitted branching ratio $\mathcal{B}(t \to bH^+)$, where:

$$\text{Pull} = \frac{\mathcal{B}(t \to bH^+)^{fit} - \mathcal{B}(t \to bH^+)^{exp}}{\sigma^{fit}}. \tag{7.9}$$

For each pseudo-experiment, $\mathcal{B}(t \to bH^+)^{fit}$ is the branching ratio provided by the likelihood fit and σ^{fit} is the error from the fit. $\mathcal{B}(t \to bH^+)^{exp}$ is the expected branching ratio which, in this null-Higgs scenario, is zero. The pull is shown as a function of the charged Higgs mass in Figure 7.9, and shows that the output of the fit does not have a mass-dependent bias.

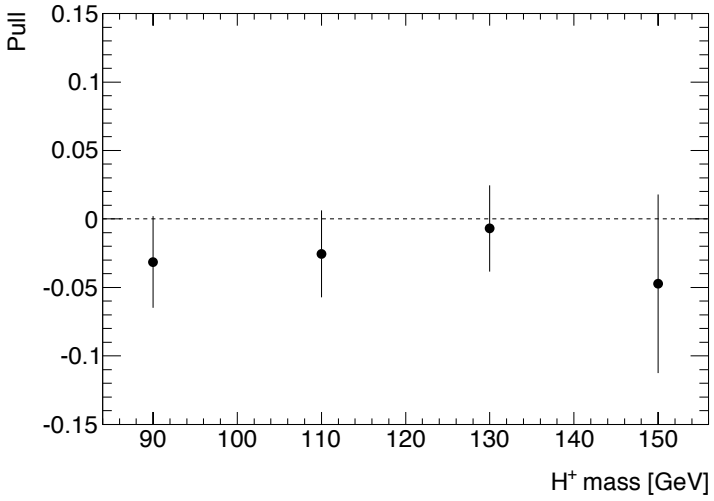

Figure 7.9: The pull on the fitted branching ratio $\mathcal{B}(t \to bH^+)$, over all pseudo-experiments, as a function of the charged Higgs mass.

7.5.4 Limit Extraction

The upper limit on $\mathcal{B}(t \to bH^+)$ at 95% CL is extracted using the likelihood shape as a function of $\mathcal{B}(t \to bH^+)$. For each pseudo-experiment, the negative log likelihood is minimised to find the values of the three fit parameters that best

describe the data. $N_{t\bar{t}}$ and N_{bkg} are fixed to the fit results, and LH is computed over the range $0 \leq \mathcal{B}(t \rightarrow bH^+) \leq 1$. An example result from one pseudo-experiment is shown as the solid line in Figure 7.10. Also shown as the dashed line is the integral of this curve. The upper limit on $\mathcal{B}(t \rightarrow bH^+)$ at 95% CL for this pseudo-experiment is given by the projection on to the x-axis where the integration reaches 95% of the total positive area. This process is repeated for each pseudo-experiment and the null-Higgs expectation for the upper limit at 95% CL is given by the mean value of the upper limit over all pseudo-experiments.

The expected upper limits are shown, as a function of the charged Higgs mass, as the black line in Figure 7.11. The expected limits increase as the charged Higgs mass approaches the W-boson mass, due to the large overlap between the signal and $t\bar{t}$ background templates. In the peak of the template distribution from $t\bar{t}$ events, the effect of Poisson fluctuations can vary the bin content by a larger number of events than in the tails of the distribution. As a result, the limits on $\mathcal{B}(t \rightarrow bH^+)$ are looser for a 90 GeV charged Higgs than, for example, for a 130 GeV charged Higgs. The red line in Figure 7.11 shows the current best limits provided by the Tevatron experiments with 2.2 fb^{-1} data [13] [14]. The expected limits from ATLAS are substantially below the Tevatron limits; however this analysis has, so far, only accounted for statistical uncertainties. The following chapter describes the estimation of the systematic uncertainties that affect this measurement, which will be shown to increase the expected upper limits.

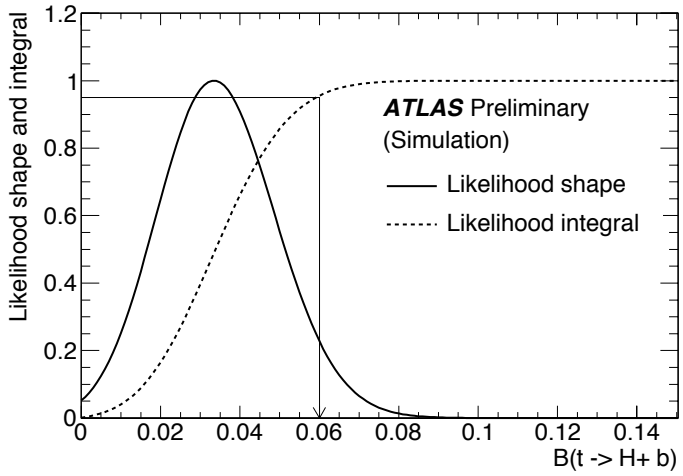

Figure 7.10: Example likelihood shape (solid line) and likelihood integral (dotted line) as a function of positive $\mathcal{B}(t \to bH^+)$ for one pseudo-experiment [57]. In both cases, the maximum value is normalised to one. The arrow shows the position of the upper limit at 95% confidence level from this particular pseudo-experiment.

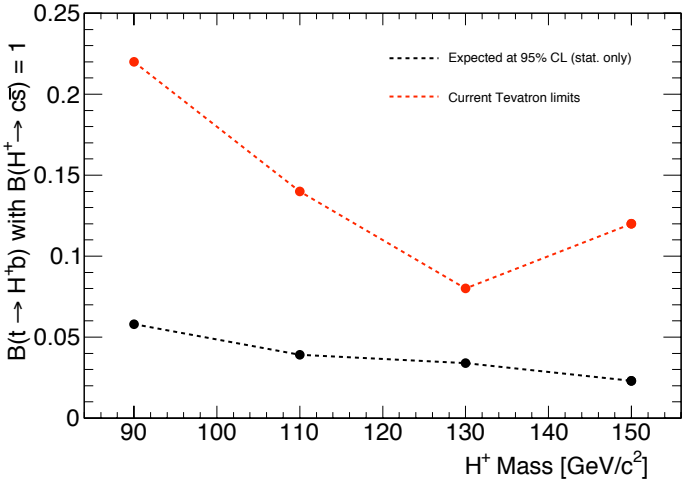

Figure 7.11: Expected upper limits on $\mathcal{B}(t \to bH^+)$, assuming 200 pb^{-1} of data at $\sqrt{s} = 10$ TeV, along with the current limits from the Tevatron with 2.2 fb^{-1} data. The limits from ATLAS do not include systematic uncertainties.

Process	Expected number of events after							
	no cut	1 lepton	E_T^{miss}	4 jets	2 b-tags	trigger	χ^2	M_{top}
$H^+ \to c\bar{s}$, 90 GeV	4757	1880	1687	1052	267	235	89	74
$H^+ \to c\bar{s}$, 110 GeV	4757	1908	1719	1066	236	208	84	72
$H^+ \to c\bar{s}$, 130 GeV	4757	1921	1719	1040	188	165	57	49
$H^+ \to c\bar{s}$, 150 GeV	4757	1968	1753	969	121	107	33	28
SM $t\bar{t}$, not all hadronic	43680	17022	15428	7828	2117	1869	794	683
Single top, Wt-channel	2853	1210	1077	249	39	35	12	9
Single top, t-channel	8635	3428	3072	479	102	89	17	14
Single top, s-channel ($e\nu$)	152	72	64	4	2	1	0	0
Single top, s-channel ($\mu\nu$)	152	91	82	7	2	2	0	0
Wbb + jets	2320	795	678	131	29	26	5	3
$W \to e\nu$ + jets	17739	8107	6902	2288	7	7	1	1
$W \to \mu\nu$ + jets	17519	10136	8799	2997	10	8	2	1
$W \to \tau\nu$ + jets	17641	1229	1058	387	1	1	0	0

Table 7.1: The effect of all applied cuts on the charged Higgs signal, assuming $\mathcal{B}(t \to bH^+) = 10\%$, and on the main Standard Model backgrounds. The integrated luminosity is 200 pb^{-1} and all numbers are rounded.

Chapter 8

Systematic Uncertainties

This chapter deals with the systematic uncertainties that affect the expected limits on the branching ratio $\mathcal{B}(t \to bH^+)$ derived in Chapter 7. Each systematic effect is described, and its effect on the expected limit is quantified. The total systematic uncertainty is then included in the expected upper limit. Finally, the effect of pile-up on the sensitivity of the analysis is assessed.

8.1 Sources of Systematic Error

There are many potential sources of systematic uncertainty on the extracted upper limits on $\mathcal{B}(t \to bH^+)$. In this analysis, systematic uncertainties have two effects. Firstly they change the acceptances of signal and background events through the selection cuts and, secondly, they perturb the shape of the di-jet mass distribution used in the limit setting. Since the total number of $t\bar{t}$ events is used as a parameter in the likelihood fit, the overall normalisation of the data-distribution is a result of the fit. For this reason, the result of the upper limit on $\mathcal{B}(t \to bH^+)$

is essentially independent of the uncertainty on the integrated luminosity which, in early data, is expected to be around 20% [59]. This argument also applies to other uncertainties on the overall normalisation, such as the theoretical $t\bar{t}$ cross section, or the trigger and object reconstruction efficiencies, which affect the signal and backgrounds in the same way. The analysis is, instead, sensitive to changes in the relative number of charged Higgs signal and $t\bar{t}$ background events. The dominant systematic effects are expected to be those that change the shape of the di-jet mass distribution, or change the acceptance of the signal channel relative to the background channels.

The systematic uncertainties can be separated into generator-level uncertainties, and those due to detector effects. At the generator level, the results can be affected by the choice of Monte Carlo generator, the tools used to model the hadronisation, parton showering and underlying event, and the amount of QCD radiation present. The uncertainties due to detector effects include uncertainties on the scale and resolution of experimental quantities such as the jet and lepton energies. Uncertainties affecting the overall normalisation are not considered here. The effect of a $\pm 1\sigma$ change in each source of systematic error is simulated in the Monte Carlo events, and the samples are used to derive the new event selection efficiencies, and perturbed di-jet mass distributions. The important systematic contributions are described Sections 8.1.1 to 8.1.5 and the resulting event selection efficiencies are discussed in Section 8.3.

8.1.1 Monte Carlo Generator

This analysis is based on the comparison of a 'data' distribution to a set of template shapes derived from Monte Carlo simulations. This is a potential source of systematic error, since the exact shape of the templates can depend on the

Monte Carlo generator used, and how the generator was tuned to reflect experimental data. The analysis of the $H^+ \to c\overline{s}$ channel at CDF [13] compares data to the results of Pythia, after the results of this Monte Carlo generator have been tuned to reflect the properties of measured data at $\sqrt{s} = 1.96$ TeV. The resulting systematic uncertainty due to the choice of Monte Carlo generator is, therefore, small. At the high energies accessible by the LHC, however, the reliability of Monte Carlo simulations has not yet been thoroughly verified.

The systematic uncertainty due to the choice of Monte Carlo generator was estimated by comparing the results using the nominal events generated with MC@NLO to a set of events generated using AcerMC. Since AcerMC is a leading-order generator, whilst MC@NLO is a next-to-leading-order generator, this accounts for the effect of generating events at different orders in perturbation theory. This systematic uncertainty also covers the effect of different modelling of the hadronisation, parton showering and underlying event. In this analysis, MC@NLO was interfaced to Herwig/Jimmy for modelling these effects, whilst AcerMC was interfaced to Pythia. Figure 8.1 shows a comparison of the di-jet mass distributions from $t\overline{t}$ decays generated using MC@NLO and Acer MC.

8.1.2 Initial and Final State Radiation

In a $t\overline{t}$ event, QCD gluons can be radiated from either the incoming partons inside the protons (Initial State Radiation) or from the final state quarks (Final State Radiation). In this analysis, each top-pair event is reconstructed under the assumption that the four highest p_T jets reconstructed in the detector can be attributed to the four quarks from the $t\overline{t}$ decay. A hard gluon radiated from the initial state could have high enough p_T to form one of the four leading jets. A gluon radiated from a final state quark would reduce the momentum of the

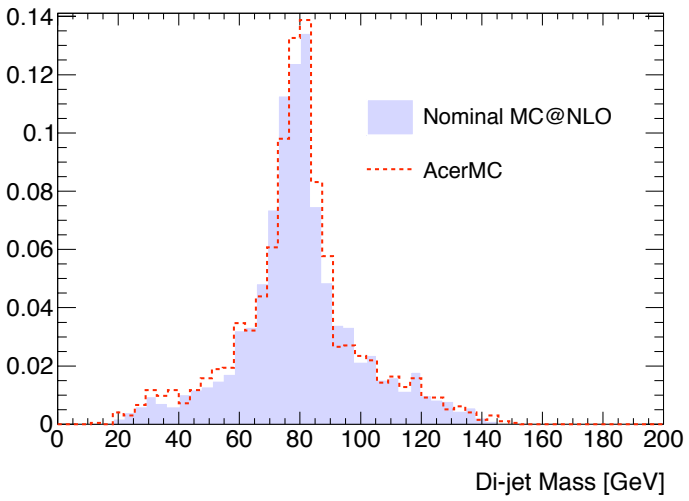

Figure 8.1: A comparison of the di-jet mass distribution from Standard Model $t\bar{t}$ events using the nominal MC@NLO events and using events generated with AcerMC. The distributions are normalised to unit area.

measured quark-jet, assuming that the gluon is radiated at an angle large enough to fall outside of the original jet-cone. Initial and final state radiation, therefore, can affect both the event selection efficiency and the shape of the di-jet mass distribution.

The amount of initial and final state radiation is sensitive to the QCD scale, Λ, which describes the energy scale at which QCD interactions become significant. Standard Model $t\bar{t}$ events were generated using AcerMC and varying the value of Λ in the running coupling α_s by factors of 2 and 0.5. Figure 8.2 shows a comparison of the di-jet mass distribution from $t\bar{t}$ decays generated with the standard Acer MC settings, and with increased QCD radiation. The additional radiation is seen to broaden the di-jet mass distribution substantially.

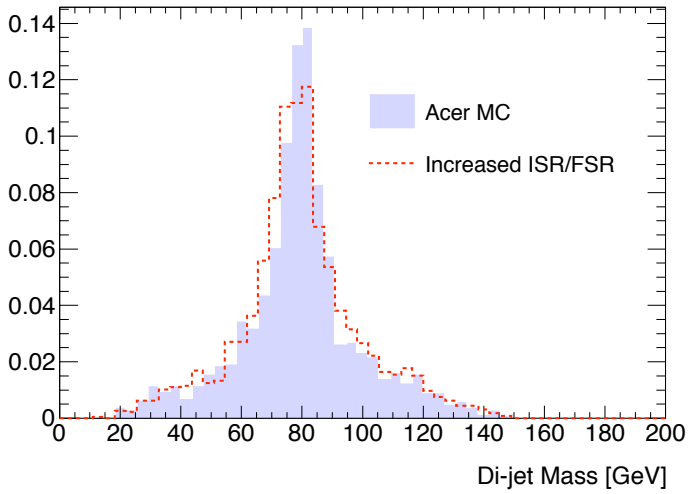

Figure 8.2: A comparison of the di-jet mass distribution from Standard Model $t\bar{t}$ events generated with the standard Acer MC settings and with additional QCD radiation. The distributions are normalised to unit area.

8.1.3 Lepton Energy Scale

Following [59] the systematic effect of the Lepton Energy Scale (LES) was modelled by scaling all lepton energies up (LES positive) and down (LES negative) by 1%. The E_T^{miss} was then corrected accordingly. Figure 8.3 shows the effect of this re-scaling on the di-jet mass distribution. The lepton energy is not directly related to the di-jet mass and, as expected, the effect of this systematic uncertainty on the di-jet mass distribution is very small.

8.1.4 Jet Energy Resolution

Reconstructed jets have a non-zero energy resolution as a result of detector effects such as calorimeter sampling. Detector simulations and test-beam studies have led to an estimate of the jet energy resolution, but studies of real data will be required to ascertain whether this estimate is correct. This systematic uncertainty

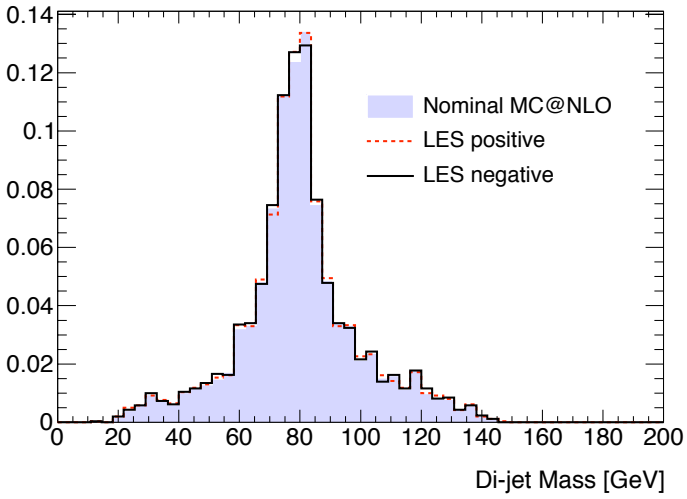

Figure 8.3: A comparison of the di-jet mass distribution from the MC@NLO Standard Model $t\bar{t}$ events in the nominal case and with rescaling of lepton energies to reflect the uncertainty on the lepton energy scale. The distributions are normalised to unit area.

considers the scenario in which the true resolution of the jet energies measured in the detector is larger than expected, and will only be required for early-data analyses since, in the long term, studies of real data will give the true jet energy resolution. Following [59] the jet energies, E, were given additional smearing based on a Gaussian distributed with:

$$\sigma = 0.45 * \sqrt{E} \qquad (|\eta| < 3.2),$$
$$\sigma = 0.63 * \sqrt{E} \qquad (|\eta| > 3.2). \tag{8.1}$$

The two different values of σ reflect the fact that the jet energies are better measured in the central region of the calorimeters. To model the resolution effect, each jet energy was replaced with a number picked randomly from a Gaussian distribution centred on E, with width σ. The E_T^{miss} was then corrected accordingly. Figure 8.4 shows the effect of the jet energy resolution systematic on the di-jet mass distribution from Standard Model $t\bar{t}$ events. This systematic effect was found to slightly broaden the peak of the di-jet mass distribution.

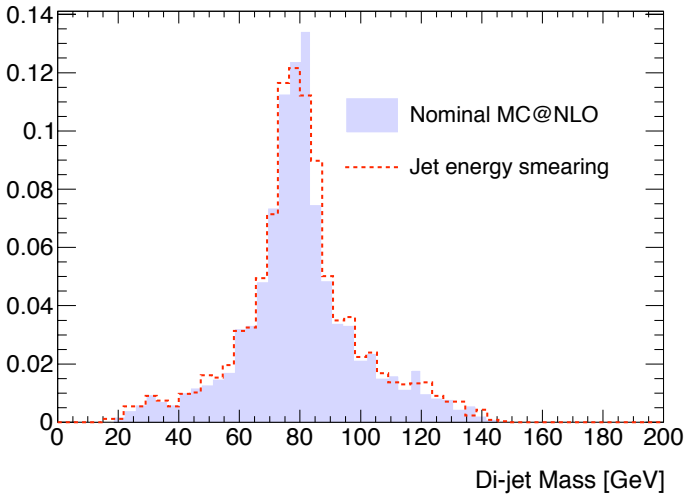

Figure 8.4: A comparison of the di-jet mass distribution from the MC@NLO Standard Model $t\bar{t}$ events in the nominal case and with rescaling of jet energies to reflect the jet energy resolution. The distributions are normalised to unit area.

8.1.5 Jet Energy Scale

The Jet Energy Scale, described in Section 6.1.4, describes the size of the correction required to calibrate measured jet energies, in order to reproduce the truth particle level information. As the integrated luminosity recorded by ATLAS increases, the measurement of the Jet Energy Scale will be more tightly constrained; ultimately it is expected to be measured with a precision of $\leq 2\%$. During early data-taking, however, the percentage uncertainty on the jet energy is expected to be [59]:

$$\begin{aligned} &\pm 7\% \quad (|\eta| < 3.2) \\ &\pm 15\% \quad (|\eta| > 3.2) \end{aligned} \tag{8.2}$$

The systematic uncertainty due to the Jet Energy Scale was modeled by rescaling the energy of all jets in each event in the positive direction (JES positive) and in the negative direction (JES negative). The E_T^{miss} was then corrected accordingly. Figure 8.5 shows the effect of the Jet Energy Scale uncertainty on the di-jet

mass distributions from Standard Model $t\bar{t}$ events, both before and after the χ^2 fitting. In both cases, systematically increasing (decreasing) the jet energies gives a positive (negative) shift to the position of the di-jet mass peak. However, the effect is more pronounced in the unfitted distribution; the re-scaling of jet energies in the χ^2 fit corrects, to some extent, for the Jet Energy Scale uncertainty.

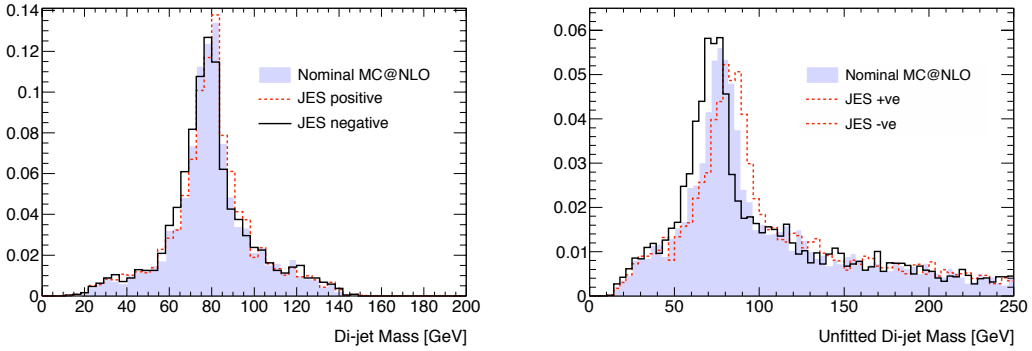

Figure 8.5: Comparisons of the di-jet mass distributions from MC@NLO Standard Model $t\bar{t}$ events in the nominal case and with rescaling of jet energies to reflect the uncertainty on the jet energy scale. (Left) The fitted di-jet mass distribution used in the analysis. (Right) The di-jet mass distribution before χ^2 fitting. All distributions are normalised to unit area.

8.2 Jet Energy Scale Recalibration

The systematic uncertainty due to the Jet Energy Scale has the scope to be reduced in size by using an 'in situ' calibration of the jet energies. This technique has been used, for example, in the measurement of the top-quark mass at CDF [67], and is based on the mass distribution of the W-boson in Standard Model $t\bar{t}$ events. The recalibration is derived from the di-jet mass distribution before the χ^2 fitting (described in Chapter 7.2) is performed, since this distribution has been shown in Figure 8.5 to be more sensitive to changes in the Jet

Energy Scale than the equivalent fitted distribution.

In the recalibration, the peak position of the unfitted di-jet mass distribution after the effect of the Jet Energy Scale has been simulated is compared to the nominal peak value using a Gaussian fit over a 1.5σ range. Before fitting, the distributions are re-binned with finer binning, an example of which is shown in Figure 8.6 (left). The ratio of the two peak positions is then used as a re-scaling factor, and is applied to the energies of all jets in order to correct for the effect of the Jet Energy Scale uncertainty. The re-scaling factors were found to be 1.056 for the positive Jet Energy Scale systematic, and 0.932 for the negative Jet Energy Scale systematic, and Figure 8.6 (right) shows the resulting di-jet mass distributions after the recalibration has been applied. The recalibration largely corrects the shift in the di-jet mass distribution due to the Jet Energy Scale uncertainty. In a study of real data, the recalibration will be derived by comparing the unfitted di-jet mass distribution from data with the equivalent distribution from Standard Model $t\bar{t}$ Monte Carlo events.

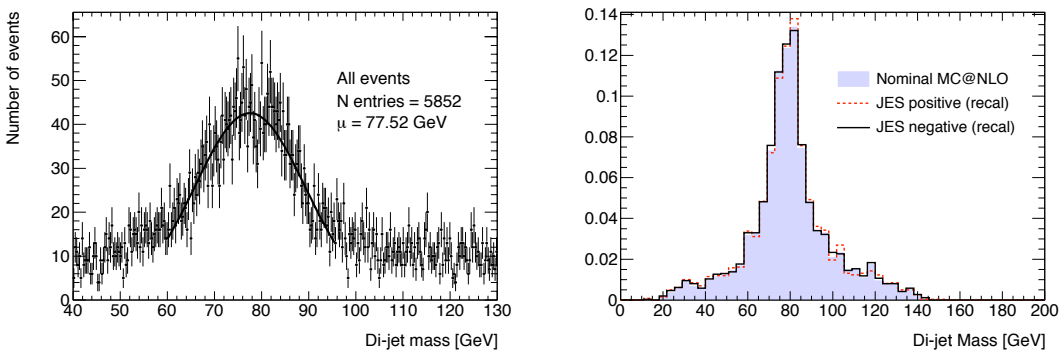

Figure 8.6: (Left) The unfitted di-jet mass distribution used to derive the Jet Energy Scale recalibration. This is the peak region of Figure 8.5 (right) with finer binning. (Right) A comparison of the di-jet mass distribution from the MC@NLO Standard Model $t\bar{t}$ events in the nominal case and with rescaling of jet energies to reflect the uncertainty on the jet energy scale, and the jet energy recalibration applied to all jets in the event. The normalisation is to unit area.

The Jet Energy Scale recalibration is one inclusive number that does not account for the region of the detector in which the jets fall. Figure 8.7 shows the unfitted di-jet mass distribution separated into events where both jets fall in the central, $|\eta| < 1.475$, region (CC), and where one jet is in the central region and the other in the forward,$|\eta| > 1.475$, region (CF). The mean of the distribution from CC and CF events was found to vary by around 2 GeV. Weighting by the number of events in each category leads to an uncertainty of 1.2% on the size of the Jet Energy Scale recalibration. In future studies, however, different rescaling factors can be derived for these different categories of event. Events where both jets fell in the forward region were a negligible contribution to the di-jet mass distribution.

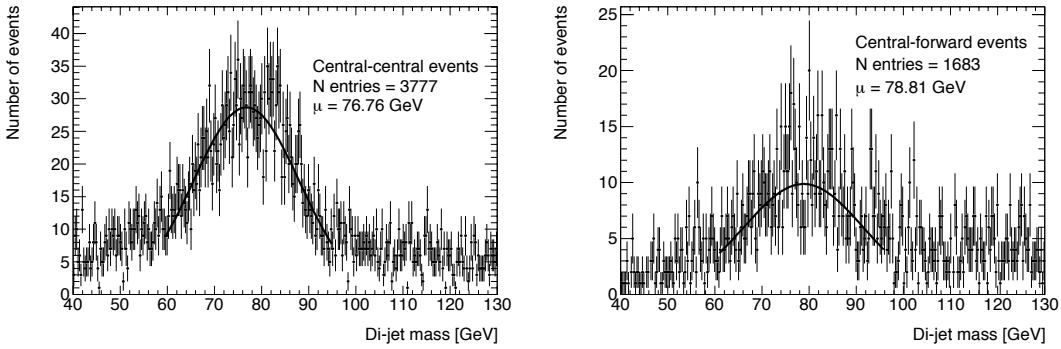

Figure 8.7: (Left) The unfitted di-jet mass distribution from events where both jets fall in the central region, $|\eta| < 1.475$. (Right) The same distribution from events where one jet falls in the central region and the other in the forward region, $|\eta| > 1.475$.

Other systematic effects can affect the JES recalibration if they change the peak position of the un-fitted di-jet mass distribution. Potential sources of uncertainty are the choice of Monte Carlo generator, and the amount of initial and final state radiation, although these effects have not yet been fully studied.

The Jet Energy Scale recalibration is derived from the mass distribution of

the W-boson in Standard Model $t\bar{t}$ events and, by definition, it only contains information about light (u, d, s, c) quarks, since the W-boson is kinematically forbidden to decay to a tb-pair. The recalibration is, however, applied to all jets. An additional systematic uncertainty was introduced to account for any potential differences between the b-Jet Energy Scale and the light-Jet Energy Scale. This was modelled by rescaling the energies of all b-tagged jets up and down by 3%, and is referred to in the following as the bJES systematic. The size of this uncertainty may be a conservative estimate, but it will be better understood from studies of real data. There is also scope to reduce the size of this systematic uncertainty by using the top quark mass, in addition to the W-boson mass, to derive the Jet Energy Scale recalibration.

8.3 Event Selection Efficiencies

The full list of systematics, and the changes introduced to model their effects, are summarised in Table 8.1. Table 8.2 shows a selection of the perturbed event selection efficiencies after different systematic uncertainties have been introduced. These efficiencies can be compared with the nominal efficiencies in Table 6.1. The effect of the Jet Energy Scale uncertainty (shown as MC@NLO $t\bar{t}$ $+\sigma_{JES}$ / $-\sigma_{JES}$) is initially quite large. The acceptances after applying the Jet Energy Scale recalibration are shown in Table 8.2 as MC@NLO $t\bar{t}$ + JES recal, and are close to the value obtained for the nominal sample. Note that charged Higgs signal Monte Carlo events were not available with modeling of increased or decreased ISR/FSR. In estimating this systematic contribution, the event selection efficiencies for each mass point were re-scaled to match the change in the Standard Model $t\bar{t}$ events due to this effect.

Systematic	Change Introduced
Jet Energy Resolution ($\|\eta\| < 3.2$)	$0.45 * \sqrt{E}$
Jet Energy Resolution ($\|\eta\| > 3.2$)	$0.63 * \sqrt{E}$
Jet Energy Scale ($\|\eta\| < 3.2$)	$\pm 7\%$
Jet Energy Scale ($\|\eta\| > 3.2$)	$\pm 15\%$
b-jet Energy Scale	b-tagged jet energy $\pm 3\%$
Lepton Energy Scale	$\pm 1\%$
Monte Carlo Generator	MC@NLO vs AcerMC

Table 8.1: Summary of the changes introduced to model the effect of each systematic uncertainty.

8.4 Limit Setting

For each source of systematic uncertainty, 1000 pseudo-experiments were generated from the di-jet mass distribution perturbed by the systematic uncertainty under consideration. The likelihood fit was then performed as described in Chapter 7.5. The nominal template distributions, shown in Figure 7.6, were fitted to the perturbed pseudo-data distributions and the size of the systematic uncertainty was taken to be the shift in the expected upper limit on $\mathcal{B}(t \to bH^+)$ from the nominal result, given in Section 7.5.4. The size of each systematic uncertainty is shown in Table 8.3. After the JES recalibration, the analysis is largely insensitive to the JES.

The combined effect of all systematic uncertainties on the expected upper limit on $\mathcal{B}(t \to bH^+)$ at 95% CL is based on a Gaussian smearing of the original likelihood function according to:

$$LH'(x') = \int_0^1 LH(x) \times \frac{1}{\Delta(x')\sqrt{2\pi}}\ exp\left(-\frac{1}{2}.\left[\frac{x'-x}{\Delta(x')}\right]^2\right) dx. \qquad (8.3)$$

In Equation 8.3, both x and x' represent the branching ratio $\mathcal{B}(t \to bH^+)$. $LH(x)$ is the likelihood function with no systematic smearing, an example of which is

Sample	Expected number of events after							
+ syst	no cuts	lepton	MET	4 jets	2 b-tags	trigger	χ^2	M_{top}
MC@NLO $t\bar{t}$								
nominal	43680	17022	15428	7828	2117	1869	794	683
$+\sigma_{\text{JES}}$	43680	17022	15555	8407	2242	1982	801	666
$-\sigma_{\text{JES}}$	43680	17022	15379	7247	1977	1748	724	629
$+\sigma_{\text{JER}}$	43680	17022	15453	7819	2106	1862	774	669
$+\sigma_{\text{bJES}}$	43680	17022	15457	7857	2133	1883	790	681
$-\sigma_{\text{bJES}}$	43680	17022	15415	7808	2090	1845	784	677
$+\sigma_{\text{LES}}$	43680	17077	15509	7874	2131	1880	793	685
$-\sigma_{\text{LES}}$	43680	16971	15372	7806	2106	1860	790	680
MC@NLO $t\bar{t}$ + JES recal								
$+\sigma_{\text{JES}}$	43680	17022	15459	7944	2140	1889	790	683
$-\sigma_{\text{JES}}$	43680	17022	15427	7813	2113	1866	796	685
H^+ (130 GeV) + JES recal								
$+\sigma_{\text{JES}}$	4757	1921	1723	1052	191	167	58	51
$-\sigma_{\text{JES}}$	4757	1921	1717	1038	188	165	57	49
AcerMC $t\bar{t}$								
default	43680	17164	15545	8673	2248	1989	798	688
less I/FSR	43680	17727	16040	8900	2251	1993	806	701
more I/FSR	43680	17395	15677	9356	2432	2152	841	720

Table 8.2: Cut flow table for systematics samples, assuming 200 pb^{-1} of data recorded at $\sqrt{s} = 10$ TeV.

shown as the solid line in Figure 8.8 (left). The smeared likelihood function $LH'(x')$ is calculated from the convolution of $LH(x)$ with a Gaussian whose width describes the combination in quadrature of all systematic uncertainties. The effect of this smearing on the likelihood shape is shown as the dashed line in Figure 8.8 (left) for one particular pseudo-experiment. For each pseudo-experiment, the expected upper limit on $\mathcal{B}(t \to bH^+)$ at 95% confidence level is given by the projection onto the x-axis where the integral of the smeared distribution reaches 95% of the total positive area. Figure 8.8 (right) shows the upper limit extracted from each pseudo-experiment, and the resulting 1σ and 2σ bands around the mean value. Each pseudo-experiment, for example, Figure 8.8 (left) contributes

Systematic	Definition	$\Delta\mathcal{B}$	ΔA (%)
Jet Energy Resolution	$\lvert n-p\rvert$	0.00709	2.1
Jet Energy Scale	$(\lvert n-+ve\rvert+\lvert n--ve\rvert)/2$	0.00070	0.2
MC Generator	$n-m$	0.00558	0.6
ISR/FSR	$(\lvert m-+ve\rvert+\lvert m--ve\rvert)/2$	0.00535	3.3
b-jet Energy Scale	$(\lvert n-+ve\rvert+\lvert n--ve\rvert)/2$	0.00752	0.6
Lepton Energy Scale	$(\lvert n-+ve\rvert+\lvert n--ve\rvert)/2$	0.00084	0.4
Combination	In quadrature	0.01262	-

Table 8.3: The effect of systematic uncertainties on $\mathcal{B}(t \to bH^+)$ assuming a 130 GeV H^+, where n and m are the nominal branching ratios using respectively the MC@NLO and AcerMC samples, and p is the branching ratio when the jet energy resolution has been simulated. Where shown, $\pm ve$ give the extracted upper limits on the branching ratio for the positive and negative variations of each systematic. $\Delta\mathcal{B}$ is the change in the extracted upper limit on the branching ratio at 95% confidence level. Also shown for reference is the percentage change in acceptance, ΔA, associated with each systematic effect.

one entry to Figure 8.8 (right).

The expected limits for charged Higgs masses of 90 to 150 GeV are shown in the top half of Table 8.4, assuming 200 pb^{-1} of data at $\sqrt{s} = 10$ TeV. The expected limit is considerably higher as the charged Higgs mass approaches the W-boson mass. This is an unavoidable consequence of using a likelihood fitting technique based on the di-jet mass distribution in the mass region where the signal and background templates tend to the same distribution. These results are summarized in Figure 8.9, along with the Tevatron limits from 2.2 fb^{-1} of data. Also shown in Table 8.4 are the equivalent limits assuming 1 fb^{-1} of data at $\sqrt{s} = 7$ TeV[1], which are summarised in Figure 8.10. The results at 7 TeV are based on the re-scaled event selection efficiencies described in Section 6.4, and the di-jet mass templates shown in Figure 7.6. The limits derived show that ATLAS has the potential to substantially improve on the Tevatron results in early data scenarios with collisions at either $\sqrt{s} = 7$ TeV and $\sqrt{s} = 10$ TeV.

[1]Work by Paul Miyagawa

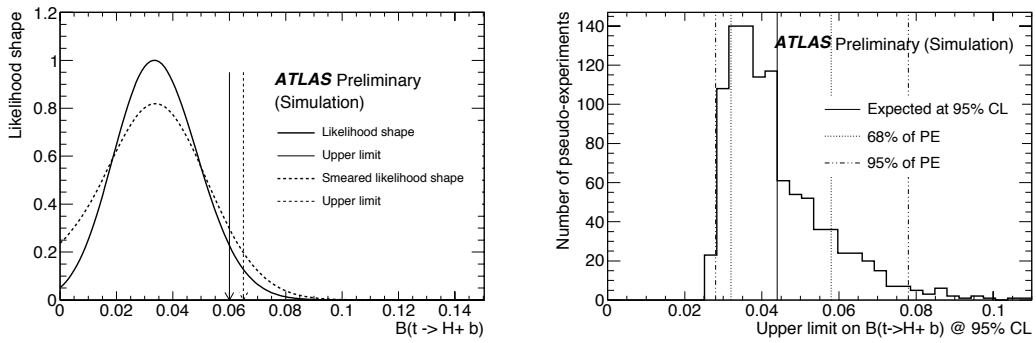

Figure 8.8: (Left) An example likelihood shape for one pseudo-experiment before (solid line) and after (dotted line) systematic smearing. The solid and dotted arrows show the respective upper limits at 95% confidence level that can be derived from this pseudo-experiment. (Right) The upper limit on $\mathcal{B}(t \to bH^+)$ at 95% confidence level for each pseudo-experiment assuming a H^+ mass of 130 GeV. The mean (solid line) is taken as the expected value given a null-Higgs hypothesis. The dotted and dashed lines show the values of $\mathcal{B}(t \to bH^+)$ which contain 68% and 95% of entries respectively.

8.5 Pile-up Studies

At the design luminosity of 10^{34} cm^{-2}s^{-1}, an average of 23 inelastic proton-proton collisions are expected to occur in every bunch crossing. An 'interesting' collision may cause the trigger to fire, but the resulting snapshot recorded by the detector is an overlay of many proton-proton interactions. This effect is known as pile-up, and is an important background to many ATLAS analyses since it results in the reconstruction of additional objects such as tracks and calorimeter clusters that are not associated with the primary event of interest. Additional background effects are also expected due to the constant presence of high-energy neutrons in the ATLAS cavern. Interactions between the neutrons and the detector shielding are a source of electrons and spallation protons that, as charged particles, can be observed in the Muon Spectrometer. This effect is known as the cavern background.

$\sqrt{s} = 10$ TeV, $\mathcal{L}_{int} = 200$ pb^{-1}, $N_{t\bar{t}}$ (expected) = 80320				
m_{H^+} (GeV)	90	110	130	150
Expected upper limit $\mathcal{B}(t \to bH^+)$ (stat. only)	5.8%	3.9%	3.4%	2.3%
Expected upper limit $\mathcal{B}(t \to bH^+)$ (stat + syst)	17.8%	5.5%	4.4%	4.3%

$\sqrt{s} = 7$ TeV, $\mathcal{L}_{int} = 1$ fb^{-1}, $N_{t\bar{t}}$ (expected) = 160800				
m_{H^+} (GeV)	90	110	130	150
Expected upper limit $\mathcal{B}(t \to bH^+)$ (stat. only)	4.0%	2.5%	2.3%	1.5%
Expected upper limit $\mathcal{B}(t \to bH^+)$ (stat + syst)	14.8%	4.7%	3.4%	3.7%

Table 8.4: Expected upper limits on $\mathcal{B}(t \to bH^+)$ at 95% confidence level, for charged Higgs masses of 90 to 150 GeV, assuming 200 pb^{-1} of data at $\sqrt{s} = 10$ TeV, and assuming 1 fb^{-1} of data at $\sqrt{s} = 7$ TeV. Also shown is the total number of $t\bar{t}$ events expected in each data-set.

The limits shown in Figures 8.9 and 8.10 do not take into account the effects of pile-up or cavern backgrounds. Assuming that during early data-taking the LHC reaches luminosities of the order 10^{32} cm^{-2} s^{-1}, however, such effects cannot be assumed to be negligible. Following [68], Monte Carlo events were generated under the following assumptions:

- Luminosity = 10^{32} cm^{-2}s^{-1},
- Bunch spacing = 450 ns,
- Cavern safety factor = 2.

The size of the background due to cavern neutron events is not well known, and the cavern safety factor describes the assumed number of cavern events per bunch crossing [69]. The bunch spacing and luminosity assumptions result in an average of four additional pile-up interactions per event. Due to computing constraints, Monte Carlo events including pile-up and the cavern background were only generated for Standard Model $t\bar{t}$ events, and for the charged Higgs mass points at 90 GeV and 130 GeV. The effect of pile-up on the non-$t\bar{t}$ backgrounds

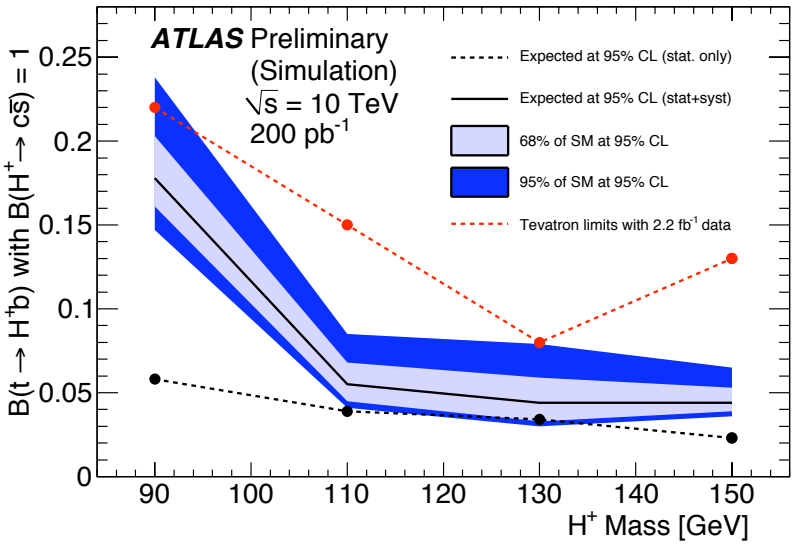

Figure 8.9: The expected upper limit, including systematic uncertainties, on the branching ratio $\mathcal{B}(t \to bH^+)$ as a function of the charged Higgs mass, assuming 200 pb^{-1} data at 10 TeV. The black solid line shows the mean upper limit over all pseudo-experiments, while the 1 σ and 2 σ bands show the region in which 68% and 95% of the pseudo-experiment results fall. For comparison, the black dotted line shows the equivalent limits without systematic uncertainties, while the red dotted line shows the Tevatron results with 2.2 fb^{-1} of data.

is not considered here. In the following, the term 'pile-up' is used to encompass both pile-up and cavern background effects, since only one systematic uncertainty is estimated for the two effects.

Table 8.5 shows the selection efficiencies for a 90 GeV signal sample and for the Standard Model $t\bar{t}$ background when the effect of pile-up is included. As expected, the selection efficiency through the 4 jet cut is increased substantially, since the pile-up interactions give additional energy to each jet. The selection efficiency for the lepton cut is decreased slightly, since the lepton isolation requirement is more difficult to satisfy in the busier pile-up environment. Pile-up effects also shift the di-jet mass distributions to a higher mass since, on average, the jet energies are systematically increased. Figure 8.11 shows a comparison of this distribution

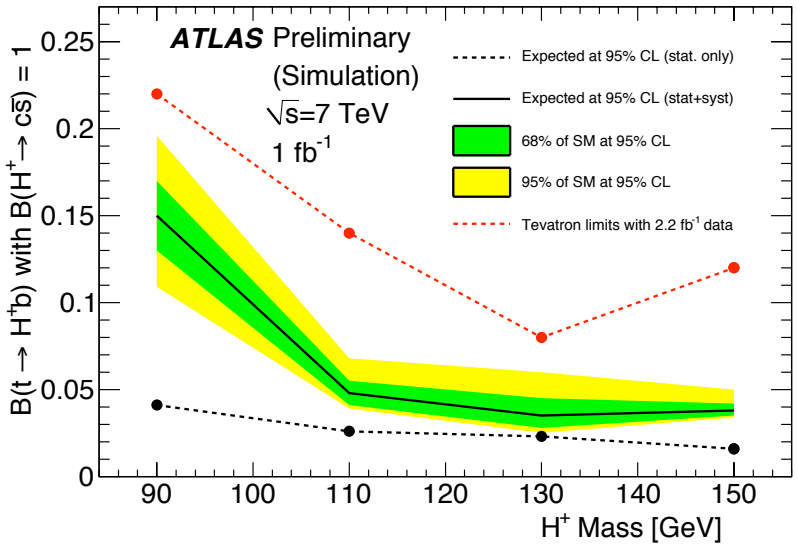

Figure 8.10: The expected upper limit, including systematic uncertainties, on the branching ratio $\mathcal{B}(t \to bH^+)$ as a function of the charged Higgs mass, assuming 1 fb^{-1} data at 7 TeV. The black solid line shows the mean upper limit over all pseudo-experiments, while the 1 σ and 2 σ bands show the region in which 68% and 95% of the pseudo-experiment results fall. For comparison, the black dotted line shows the equivalent limits without systematic uncertainties, while the red dotted line shows the Tevatron results with 2.2 fb^{-1} of data.

with and without the effects of pile-up. Such shifts can have a large effect on the extracted upper limit on $\mathcal{B}(t \to bH^+)$, since the limit setting is based on the comparison of a data distribution with the nominal shape of the di-jet mass distribution.

The number of additional primary vertices reconstructed in an event is a measure of the amount of pile-up present, and can be used to derive a pile-up jet energy recalibration. Figure 8.12 (left) shows the number of additional primary vertices in Standard Model $t\bar{t}$ events which, as expected, peaks at 4. Figure 8.12 (right) shows the average measured di-jet mass, before applying the χ^2 fit described in Section 7.2, as a function of the number of additional vertices for Standard Model $t\bar{t}$ events. As for the Jet Energy Scale recalibration, described

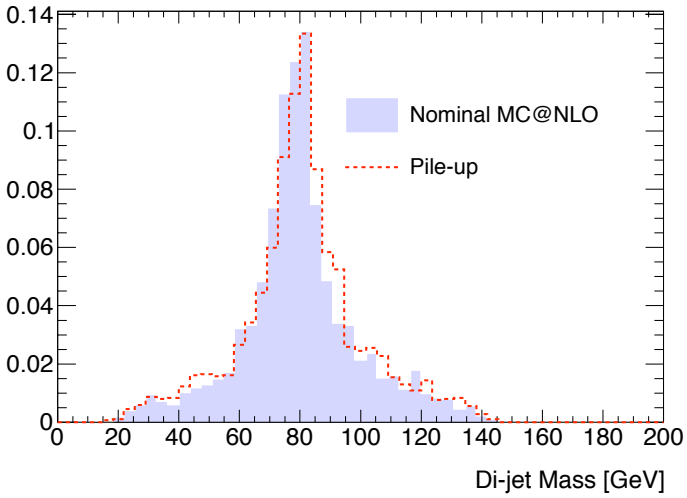

Figure 8.11: The di-jet mass distribution from Standard Model $t\bar{t}$ events with and without the effects of pile-up. The distributions are normalised to unit area.

in Section 8.2, the unfitted di-jet mass distribution was used to derive the pile-up recalibration, as it was found to have a greater sensitivity to pile-up than the equivalent fitted distribution. The rescaling of jet energies in the χ^2 fit can correct, to some extent, for the effect of pile-up. The di-jet mass varies linearly with the number of additional primary vertices, and each additional vertex was found to contribute, on average, 920 MeV to the energy of each jet. This correction was found to be consistent with that derived from the 90 GeV and 130 GeV charged Higgs signal samples. The pile-up correction was applied to all jets before the selection cuts were applied, and the resulting cut flow is shown in Table 8.5 as 'pileup+recal'.

Following the method described in Section 8.4, the size of the systematic uncertainty, ΔB, due to pile-up was estimated, after applying the pile-up correction. This was found to be 0.090 for a 90 GeV charged Higgs and 0.004 for a 130 GeV charged Higgs. These numbers can be compared with those in Table 8.3, and the systematic uncertainty due to pile-up is of the same order as other effects such as

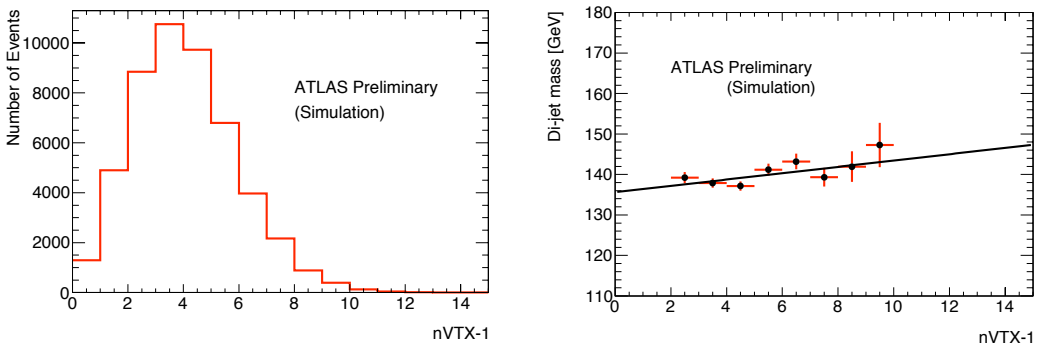

Figure 8.12: (Left) The number of additional primary vertices in Standard Model $t\bar{t}$ events. (Right) The un-fitted di-jet mass as a function of the number of additional vertices in Standard Model $t\bar{t}$ events. A linear parameterisation was used to derive a pile-up recalibration for the jet energies.

initial and final state radiation. The systematic uncertainty due to pile-up is not included in the final quoted limits, since the amount of pile-up present is highly dependent on the beam conditions, and Monte Carlo simulated events were not available for all charged Higgs mass points considered in this analysis. However, for the beam conditions described, the effect of pile-up on the expected upper limits on $\mathcal{B}(t \to bH^+)$ was found to vary between 3% and $\leq 0.3\%$ as the charged Higgs mass increases from 90 GeV to 130 GeV. The expected limits with and without pile-up are shown in Table 8.6 for a 90 GeV and 130 GeV charged Higgs.

Process	cut efficiency (%)							
	1 lepton	E_T^{miss}	4 jets	2 b-tags	trigger	χ^2	M_{top}	total eff
SM $t\bar{t}$, no pileup	0.390	0.906	0.507	0.270	0.883	0.424	0.861	0.0157
SM $t\bar{t}$, pileup	0.385	0.907	0.628	0.256	0.873	0.391	0.810	0.0155
SM $t\bar{t}$, pileup+recal	0.389	0.905	0.540	0.263	0.860	0.388	0.854	0.0142
H^+ 90 GeV, no pileup	0.395	0.897	0.624	0.254	0.882	0.376	0.831	0.0155
H^+ 90 GeV, pileup	0.389	0.898	0.718	0.232	0.860	0.349	0.843	0.0147
H^+ 90 GeV, pileup+recal	0.389	0.898	0.645	0.236	0.863	0.339	0.871	0.0136

Table 8.5: Comparison of selection efficiencies for the Standard Model $t\bar{t}$ and charged Higgs events (for a mass of 90 GeV) in three different pile-up scenarios: no pile-up, with the pile-up parameters described above, and with pile-up and recalibration of the jet energies based on the number of additional vertices in the event. In the case of no pile-up, the numbers reflect the nominal effiencies in Table 6.1 and are shown here for easy comparison. The recalibration is found to improve the shape of the di-jet mass distribution, which is shifted to a higher mass as a result of the pile-up. This correction is also seen to affect the cut efficiencies.

H^+ mass	Expected upper limit $\mathcal{B}(t \to bH^+)$	
	No pile-up	Pile-up
90 GeV	17.8%	20.8%
130 GeV	4.4%	4.5%

Table 8.6: Expected upper limits on $\mathcal{B}(t \to bH^+)$ when the effect of pile-up is included.

Chapter 9

Conclusion

The discovery of a charged Higgs boson would be a direct indication of new physics beyond the Standard Model. The results presented in this thesis show that early ATLAS data can be used to substantially improve upon our understanding of the existence of this particle. The MSSM predicts that light charged Higgs bosons can be produced in the top-quark decay $t \to bH^+$. At the centre of mass energies accessible to the LHC, copious numbers of $t\bar{t}$ pairs will be produced, providing an ideal opportunity to search for charged Higgs bosons in top-quark decays. Theoretical predictions of the branching ratio $\mathcal{B}(t \to bH^+)$, and the subsequent decay modes of the charged Higgs, vary for different MSSM scenarios. This thesis presents the expected upper limits on $\mathcal{B}(t \to bH^+)$, assuming that the charged Higgs decays exclusively to the quark pair $c\bar{s}$. If required, these limits can then be evaluated for specific MSSM scenarios by inserting the relevant prediction of the branching ratio $\mathcal{B}(H^+ \to c\bar{s})$. The observation of a charged Higgs boson in ATLAS data would rule out the minimal Higgs mechanism for particle mass generation, and support the existence of more complex models such as supersymmetry.

The signal channel of interest is a $t\bar{t}$ pair, where one top quark decays as $t \to bH^+$ and the other as $t \to bW^+$. The charged Higgs then decays as $H^+ \to c\bar{s}$ and the W-boson decays to a lepton-neutrino pair. Monte Carlo events were generated for four charged Higgs mass points (90 GeV, 110 GeV, 130 GeV and 150 GeV), for the Standard Model $t\bar{t}$ background and for non-$t\bar{t}$ backgrounds such as $W+$ jets and single top production. Other than the presence of the intermediate charged Higgs, the signal channel is identical to a Standard Model $t\bar{t}$ decay in the semi-leptonic channel and, kinematically, the two are difficult to separate. Event selection cuts on basic quantities such as the p_T, η and the multiplicity of leptons and jets were thus defined with the goal of rejecting the non-$t\bar{t}$ backgrounds, and selecting well-reconstructed $t\bar{t}$ events, rather than separating the signal from the $t\bar{t}$ background.

The analysis is based on the shape of the invariant mass distribution of the di-jet pair from the charged Higgs or W-boson, where the presence of a signal is inferred from a second peak in the W-boson mass distribution. In order to gain a better separation between the mass peaks from the signal and $t\bar{t}$ background events, a χ^2 fitting tool was employed. In the fit, the kinematics of the entire $t\bar{t}$ event were used, along with constraints on the reconstructed top quark and W-boson masses, to improve the measurement of the di-jet mass. The fitting process, together with additional cuts on the output χ^2 and the reconstructed top quark mass on the hadronic side of the $t\bar{t}$ decay, was found to substantially improve the resolution of the mass peaks from both signal and $t\bar{t}$ background events.

Assuming no charged Higgs signal events, the expected di-jet mass distributions from Standard Model $t\bar{t}$ and non-$t\bar{t}$ background events were used to generate pseudo-data distributions. A binned maximum likelihood fit was then used to derive the expected upper limits on $\mathcal{B}(t \to bH^+)$. Since this is a model-independent

search, however, the results are equally applicable to any anomalous charged boson that decays from a top quark, in association with a bottom quark. The maximum likelihood fit was shown to be free from a mass-dependent bias.

The majority of results presented in this thesis correspond to a data-set of 200 pb^{-1}, collected at $\sqrt{s} = 10$ TeV. This is the data-set that was expected to be collected by ATLAS by the end of the 2009-2010 run. In this scenario, the expected limits on $\mathcal{B}(t \to bH^+)$ range between 4.3% and 17.8%, depending on the charged Higgs mass, and show that, in this channel, ATLAS should be able to use early data to improve on the results from the Tevatron experiments. A change of LHC run strategy during 2009 has resulted in an extended period of collisions at $\sqrt{s} = 7$ TeV. To reflect this change, the expected limits were also derived assuming a data-set of 1 fb^{-1}, collected at $\sqrt{s} = 7$ TeV. These limits range between 3.5% and 15% depending on the charged Higgs mass.

At the high instantaneous luminosities accessible by the LHC, pile-up effects are expected to affect this analysis. The expected limits quoted above do not include the effects of pile-up, however, since the size of the systematic uncertainty due to pile-up is strongly related to the beam conditions. Monte Carlo events including the effects of pile-up were generated assuming an instantaneous luminosity of 10^{32} $\text{cm}^{-2}\text{s}^{-1}$ and a bunch spacing of 450 ns, for the Standard Model $t\bar{t}$ background and for charged Higgs masses of 90 and 130 GeV. Under these conditions, pile-up was found to contribute an average of four additional interactions per bunch crossing. A jet energy re-calibration was derived, in order to correct, on average, for the additional energy deposited in each jet due to pile-up interactions. Assuming 200 pb^{-1} of data collected at $\sqrt{s} = 10$ TeV, after jet energy re-calibration pile-up was found to increase the expected upper limit from 17.8% to 20.8% for a 90 GeV charged Higgs, and from 4.4% to 4.5% for a 130 GeV charged Higgs.

Future extensions of this work may improve the analysis in several areas. As the data-set collected by ATLAS increases in size, the statistical uncertainty on the presented limits will be reduced. Due to the large cross-section to produce top-quark pairs at the LHC, the results of this analysis will quickly become dominated by systematic uncertainties. The systematic uncertainties considered in this analysis are conservative estimates, and are based on the expected performance of the ATLAS detector from studies of Monte Carlo simulated events. Studies of real data over the coming months will allow better estimates of systematic effects such as the Jet Energy Scale and Lepton Energy Scale uncertainties and, in time, a more thorough understanding of the detector will allow the size of these systematic uncertainties to be reduced. The di-jet mass fitter has been shown to be a powerful tool in separating charged Higgs signal and $t\bar{t}$ background events with two b-tagged jets. The fitting tool is also designed to take as an input events with either one or zero b-tagged jets, and select the jet-to-parton assignment that is most likely to be correct. This has not yet been fully tested, but the method offers the scope to include a larger number of event types in the analysis. It remains to be seen whether this will be beneficial once systematic uncertainties dominate the results. Finally, at the design luminosity of 10^{34} $\mathrm{cm}^{-2}\mathrm{s}^{-1}$, with an average of 23 proton-proton interactions per bunch crossing, systematic uncertainties due to pile-up effects are expected to be a very real challenge. Further studies may be required in order to find the best technique to minimise the effects of pile-up on this analysis.

Appendix A

Neutrino Solutions

The presence of a neutrino in an event can be inferred from a large E_T^{miss} in the detector. Assuming that the event only contains one neutrino, and that the neutrino mass is negligible, the E_T^{miss} can be interpreted as the neutrino transverse momentum, p_T^ν. To reconstruct a leptonically decaying W boson, as in Section 7.2, the full neutrino momentum is required and, since the centre of mass energy of the colliding parton system is not known, the longitudinal momentum of the neutrino, p_L^ν, is not measured. Assigning all missing E_T to the neutrino, however, it is possible to express p_L^ν in terms of two measurable quantities: p_T^ν and the lepton momentum, p_l. The combination of the lepton and neutrino four-vectors, P_l and P_ν, is constrained to give a mass exactly equal to the W boson mass, $m_W = 80.4$ GeV:

$$m_W^2 = (P_l + P_\nu)^2 \ , \tag{A.1}$$

Assuming the mass shell conditions

$$P_\nu^2 = 0 \ , \ P_l^2 = m_l^2 \ , \tag{A.2}$$

this can be re-written as

$$\Rightarrow E_\nu = \frac{1}{2E_l}(m_W^2 - m_l^2 + 2p_l.p_\nu) \ . \tag{A.3}$$

This is of the form:

$$E_\nu = A + Bp_{\nu z} \ , \tag{A.4}$$

where:

$$A = \frac{1}{E_l}\big(\frac{m_W^2 - m_l^2}{2} + p_{lx}.p_{\nu x} + p_{ly}.p_{\nu y}\big) \ , \tag{A.5}$$

and

$$B = \frac{p_{lz}}{E_l} \ . \tag{A.6}$$

Since the co-ordinate system is defined such that the z axis is in the direction of the beamline we define:

$$p_L = p_z \ , \ p_T = (p_x + p_y)^{\frac{1}{2}}. \tag{A.7}$$

The neutrino energy can be expressed as:

$$E_\nu = (p_{\nu x}^2 + p_{\nu y}^2 + p_{\nu z}^2)^{\frac{1}{2}} \ , \tag{A.8}$$

giving a quadratic equation in p_L^ν

$$(B^2 - 1)(p_L^\nu)^2 + 2ABp_L^\nu + A^2 - (p_T^\nu)^2 = 0 \ . \tag{A.9}$$

This clearly gives two possible solutions for p_L^ν.

Bibliography

[1] W.Cottingham and D.Greenwood, An Introduction to the Standard Model of Particle Physics, Cambridge University Press (1998).

[2] J. Gunion, H. Haber, G. Kane, and S. Dawson, The Higgs Hunters Guide, Addison-Wesley, Reading (1990).

[3] L. Evans and P. Bryant, The LHC Machine, JINST **3** (2008) S08001.

[4] J. Thompson, Introduction to Colliding Beams at Fermilab, FERMILAB-TM-1909, (1994).

[5] S. Martin, A Supersymmetry Primer (1997) [arXiv:hep-ph/9709356v5].

[6] The ALEPH, CDF, D0, DELPHI, L3, OPAL and SLD Collaborations, Precision Electroweak Measurements and Constraints on the Standard Model, CERN-PH-EP/2009-023 (2009).

[7] M. Peskin, Beyond the Standard Model (1997) [arXiv:hep-ph/9705479].

[8] The LEP Collaboration, LEP Design Report, CERN-LEP/84-01 (1984).

[9] ALEPH, DELPHI, L3 and OPAL Collaborations, Search for Charged Higgs Bosons: Preliminary Combined Results Using LEP Data Collected at Energies up to 209 GeV (2001) [arXiv:hep-ex 0107031].

[10] V. M. Abazov *et al.* [D0 Collaboration], The Upgraded D0 Detector, Nucl. Instrum. Meth. A **565** (2006) 463 [arXiv:physics/0507191].

[11] F. Abe *et al.* [CDF Collaboration], The CDF II Detector Technical Design Report, FERMILAB-Pub-96/390-E (1996).

[12] CDF and D0 Collaborations, Combination of CDF and D0 Results on the Mass of the Top Quark Using up to 5.6 fb^{-1} Data, FERMILAB-TM-2466-E (2010) [arXiv:hep-ex/1007.3178v1].

[13] A. Abulencia *et al.* [CDF II Collaboration], A Search for Charged Higgs in Lepton + Jets tt-bar Events Using 2.2 fb^{-1} of CDF Data, Phys. Rev. Lett. **103** (2009) 101803 [arXiv:hep-ph/0907.1269].

[14] S. Abachi *et al.* [D0 Collaboration], A Search for Charged Higgs Bosons in $t\bar{t}$ Events, D0 Note 5715-CONF (2008).

[15] G. Aad *et al.* [ATLAS Collaboration], The ATLAS Experiment at the CERN Large Hadron Collider, Chapter 1, JINST **3** (2008) S08003.

[16] F. Halzen and A. Martin. Quarks and Leptons: An Introductory Course in Modern Particle Physics, Wiley (1984).

[17] P. Higgs, Broken Symmetries and the Masses of Gauge Bosons, Phys. Rev. Lett. **13** (1964) 508.

[18] D0 and CDF Collaborations, Searches for High-Mass Standard Model Higgs Boson at the Tevatron, Proceedings of the Conference on QCD and High Energy Interactions, Moriond, France (2010).

[19] B. C. Allanach *et al.*,The Snowmass Points and Slopes: Benchmarks for SUSY Searches, Eur. Phys. J. C **25** (2002) 113 [arXiv:hep-ph/0202233].

[20] F. Abe *et al.* [CDF Collaboration], Observation of Top Quark Production in $p\overline{p}$ Collisions with the Collider Detector at Fermilab, Phys. Rev. Lett. **74** (1995) 14 [arXiv:hep-ex/9503002].

[21] S. Abachi *et al.* [D0 Collaboration], Search for High Mass Top Quark Production in $p\overline{p}$ Collisions at $\sqrt{s} = 1.8$ TeV, Phys. Rev. Lett. **74** (1995) 13 [arXiv:hep-ex/9411001v1].

[22] J. Pumplin *et al.*, New Generation of Parton Distributions with Uncertainties from Global QCD Analysis, JHEP **7** (2002) 012 [arXiv:hep-ph/0201195].

[23] S. Head, Spin Correlation in the Dileptonic Decay of Top Quark Pairs at ATLAS, PhD Thesis, (2009).

[24] S. Moch and P. Uwer, Heavy-quark Pair Production at two loops in QCD, Nucl. Phys. Proc. Suppl. **183** (2008) 75. [arXiv:hep-ph/0807.2794].

[25] A. Abulencia *et al.* [CDF II Collaboration], Combination of CDF Top Quark Pair Production Cross Section Measurements with up to 4.6 fb^{-1}, CDF note 9913 (2009).

[26] G. B. Yu, Search for Charged Higgs Bosons in Decays of Top Quarks in Proton-Antiproton Collisions at $\sqrt{s} = 1.96$ TeV, PhD Thesis (2009).

[27] S. Dittmaier *et al.*, Charged Higgs Boson Production at the LHC: NLO Supersymmetric QCD Corrections, (2009) [arXiv:hep-ph/0906.2648v1].

[28] R. Eusebi, Search for Charged Higgs in $t\bar{t}$ Decay Products from Proton-Antiproton Collisions at $\sqrt{s} = 1.96$ TeV, FERMILAB-THESIS-2005-33 (2005).

[29] G. Aad *et al.* [ATLAS Collaboration], The ATLAS Experiment at the CERN Large Hadron Collider, Chapter 4, JINST **3** (2008) S08003.

[30] C. Grupen and B. Shwartz, Particle Detectors (Second Edition), Cambridge University Press (2008).

[31] G. Aad *et al.* [ATLAS Collaboration], The ATLAS Experiment at the CERN Large Hadron Collider, Chapter 10, JINST **3** (2008) S08003.

[32] G. Aad *et al.* [ATLAS Collaboration], The ATLAS Experiment at the CERN Large Hadron Collider, Chapter 5, JINST **3** (2008) S08003.

[33] A. Artamonov *et al.*, The ATLAS Forward Calorimeter, JINST **3** (2008) 02010.

[34] G. Aad *et al.* [ATLAS Collaboration], The ATLAS Experiment at the CERN Large Hadron Collider, Chapter 6, JINST **3** (2008) S08003.

[35] G. Aad *et al.* [ATLAS Collaboration], The ATLAS Experiment at the CERN Large Hadron Collider, Chapter 8, JINST **3** (2008) S08003.

[36] G. Aad *et al.* [ATLAS Collaboration], The ATLAS CSC Book, CERN-OPEN-2008-20 (2008).

[37] C. Ohm, T. Pauly, The ATLAS Beam Pickup-based Timing System, Proceedings of the 1st International Conference on Technology and Instrumentation in Particle Physics, Tsukuba, Japan (2009) [arXivhep-ex/:0905.3648v1].

[38] The New ATLAS Track Reconstruction (NewT) J. Phys.: Conf. Ser. **119** (2008) 032014.

[39] A. Salzburger, A Parameterization for Fast Simulation of Muon Tracks in the ATLAS Inner Detector and Muon System, PhD Thesis (2004).

[40] T. Cornelissen *et al.*, The global χ^2 track fitter in ATLAS J. Phys. Conf. Ser. **119** (2008) 032013.

[41] A. Salzburger *et al.*, The ATLAS Track Extrapolation Package, ATL-SOFT-PUB-2007-005 (2007).

[42] G. Piacquadio, Identification of b-Jets and Investigation of the Discovery Potential of a Higgs Boson in the $WH \rightarrow l\nu b\overline{b}$ channel with the ATLAS experiment, PhD thesis, CERN-THESIS-2010-027 (2010).

[43] G. Aad *et al.* [ATLAS Collaboration], The TRT Fast-OR Trigger, ATL-INDET-PUB-2009-002 (2009).

[44] S. Ask, J. Lane and J. Masik, Track Reconstruction in the ATLAS High Level Trigger Using Cosmic Ray Muons, ATL-COM-DAQ-2009-136 (2009).

[45] G. Aad *et al.* [ATLAS Collaboration], Charged-particle Multiplicities in pp Interactions at $\sqrt{s} = 900$ GeV Measured with the ATLAS Detector at the LHC, Phys. Lett. B **688** (2010) 21 [arXiv:hep-ex/1003.3124v1].

[46] G. Aad *et al.* [ATLAS Collaboration], Performance of the ATLAS Inner Detector Trigger Algorithms in p-p Collisions at $\sqrt{s} = 900$ GeV, ATL-COM-CONF-2010-014 (2010).

[47] T. Sjostrand *et al.*, PYTHIA 6.4 physics and manual, JHEP **5** (2006) 026 [arXiv:hep-ph/0603175v2].

[48] S. Jadach *et al.*, TAUOLA - a Library of Monte Carlo Programs to Simulate Decays of Polarised τ Leptons, Comp. Phys. Comm. **64** (1991) 2.

[49] S. Frixone and B. Webber, The MC@NLO 3.3 Event Generator (2006) [arXiv:hep-ph/0612272].

[50] M. Bahr *et al.*, Herwig++ Physics and Manual, Eur. Phys. J. C **58** (2008) 639 [arXiv:hep-ph/0803.0883].

[51] J. M. Butterworth *et al.*, Multiparton Interactions in Photoproduction at HERA, Z. Phys. C **72** (1996) 637 [arXiv:hep-ph/9601371].

[52] M. Mohammadi Najafabadi, Single Top Production at the LHC, (2006) [arXiv:hep-ex/0605034].

[53] B. Kersevan and E. Richter-Was, The Monte Carlo Event Generator AcerMC 2.0 with Interfaces to PYTHIA 6.2 and HERWIG 6.5 (2004) [arXiv:hep-ph/0405247].

[54] M. L. Mangano *et al.*, ALPGEN, a Generator for Hard Multi-parton Processes in Hadronic Collisions, JHEP **7** (2003) [arXiv:hep-ph/0206293].

[55] S. Hoche *et al.*, Matching Parton Showers and Matrix Elements (2006) [arXiv:hep-ph/0602031].

[56] G. Aad *et al.* [ATLAS Collaboration], Understanding Monte Carlo Generators for Top Physics, ATL-COMM-PHYS-334 (2008).

[57] G. Aad *et al.* [ATLAS Collaboration], Expected Sensitivity in Light Charged Higgs Boson Searches for $H^+ \to \tau^+\nu$ and $H^+ \to c\overline{s}$ with Early LHC Data at the ATLAS Experiment, ATL-PHYS-PUB-2010-006 (2010).

[58] G. Aad *et al.* [ATLAS Collaboration], ATLAS Sensitivity Prospects for Light Charged Higgs Bosons in the $H^+ \to c\overline{s}$ and $H^+ \to \tau\nu$ Decay Channels with Simulated LHC Data at 7 TeV, ATL-PHYS-PUB-2010-006 (2010).

[59] G. Aad *et al.* [ATLAS Collaboration], Prospects for the Top Pair Production Cross-section at $\sqrt{s} = 10$ TeV in the single lepton channel in ATLAS, ATL-PHYS-PUB-2009-087 (2009).

[60] G. Aad *et al.* [ATLAS Collaboration], Observation of $W \to l\nu$ Production and Search for $Z \to ll$ in Proton-Proton Collisions at $\sqrt{s} = 7$ TeV with the

ATLAS Detector, Proceedings of Physics at the LHC, Hamburg, Germany (2010).

[61] G. Aad *et al.* [ATLAS Collaboration], Muon Reconstruction and Identification: Studies with Simulated Monte Carlo Samples, ATL-PHYS-PUB-2009-008 (2009).

[62] J. Terron, Jet Algorithms, Zeus Weekly (2002).

[63] L. Vacavant on behalf of the ATLAS Collaboration, b-Tagging Algorithms and Performance in ATLAS, Proceedings of Physics at the LHC, Split, Croatia (2009), ATL-PHYS-PROC-2009-023.

[64] A. Abulencia *et al.* [CDF II Collaboration], Top Quark Mass Measurement Using the Template Method in the Lepton + Jets Channel at CDF II, Phys. Rev. D **73** (2006) 03200 [arXiv:hep-ex/0510048v1].

[65] K. Nakamura *et al*, The Review of Particle Physics, J. Phys. G **37** (2010) 075021.

[66] F. James, Minuit: Function Minimisation and Error Analysis, CERN Program Library Long Writeup D506 (2000).

[67] J. F. Arguin, Measurement of the Top Quark Mass with In Situ Jet Energy Scale Calibration at CDF-II, PhD Thesis (2005).

[68] G. Aad *et al.* [ATLAS Collaboration], Prospects for Measuring Top Pair Production in the Di-lepton Channel with Early ATLAS Data at $\sqrt{s} = 10$ TeV, ATL-PHYS-PUB-2009-086 (2009).

[69] B. Lockman, Pileup and Event Overlay in ATLAS Simulation, Talk given at SLUO/LHC workshop, Stanford, USA (2009).